GaN-Based Micro-LED Visible Light Communication

Line-of-Sight VLC with Active Tracking and None-Line-of-Sight VLC Demonstration

by

Zhijian Lu

A Dissertation Presented in Partial Fulfillment
of the Requirements for the Degree
Doctor of Philosophy

Approved July 2017 by the
Graduate Supervisory Committee:

Yuji Zhao, Chair
Hongbin Yu
Hongjiang Song
Daniel Bliss

ARIZONA STATE UNIVERSITY

August 2017

ABSTRACT

Visible light communication (VLC) keeps the promise of a high data rate wireless network for indoor and outdoor applications. It competes with 5G radio frequency (RF) system as well. Though the breakthrough of Gallium Nitride (GaN) based micro-light-emitting-diodes (micro-LEDs) enhances the -3dB modulation bandwidth dramatically from tens of MHz to hundreds of MHz, the light onto a fast photo receiver drops exponentially, which determines the signal to noise ratio (SNR) of VLC. To fully implement the practical high data-rate VLC link enabled by a GaN-based micro-LED, it needs focusing optics and a tracking system. In this dissertation, we demonstrate an active on-chip tracking system for VLC using a GaN-based micro-LED and None-return-to-zero on-off keying (NRZ-OOK) scheme. Using this novel technique without manual focusing, the field of view (FOV) was enlarged to 120° and data rates up to 600 Mbps at a bit error rate (BER) of 2.1×10^{-4} were achieved. This work demonstrates the establishment of a VLC physical link which shows enhanced communication quality by orders of magnitude, making it optimized for practical communication applications.

This dissertation also gives an experimental demonstration of non-line-of-sight (NLOS) visible light communication (VLC) using a single 80 μm gallium nitride (GaN) based micro-light-emitting diode (micro-LED). IEEE 802.11ac modulation scheme with 80 MHz bandwidth, as an entry level of the fifth generation of Wi-Fi, was employed to use the micro-LED bandwidth efficiently. These practical techniques were successfully utilized to achieve a demonstration of line-of-sight (LOS) VLC at a speed of 433 Mbps and a bit error rate (BER) of 10^{-5} with a free space transmit distance 3.6 m. Besides this, we demonstrated directed NLOS VLC links based on mirror reflections with a data rate of 433 Mbps and a BER of 10^{-4}. For non-directed

NLOS VLC using a print paper as the reflection material, 195 Mbps data rate and a BER of 10^{-5} was achieved.

DEDICATION

To my parents for their love and support

ACKNOWLEDGMENTS

I would love to show my sincere gratitude to my Ph.D. degree advisor, Prof. Yuji Zhao, especially for his continuous guidance and patience during the past three years. It is my great honor to take the opportunity to work for him and officially start my academia life. I am also grateful to Prof. Daniel Bliss, Prof. Hongbin Yu, and Prof. Hongjiang Song for their time and effort in reviewing my dissertation work.

I want to thank my group members Houqiang Fu, Xuanqi Huang, Hong Chen, Josh Montes, Izak Baranowski, and Xiaodong Zhang for all their help. I could not accomplish this dissertation research without their suggestions and assistance. I am also thankful to Prof. Ran Liu and Prof. Pengfei Tian from Fudan University at Shanghai, China. They offered all the high speed testing equipment for my dissertation research work. Their encouragement and enlightenment are also essential in my lab work.

In the end, I would like to thank my friends and my family for their continuous support and all those who have helped me on my way toward this moment. I gratefully acknowledge the funding support from the Science Foundation of Arizona Bisgrove Scholar Faculty Award.

TABLE OF CONTENTS

Page

CHAPTER Page

LIST OF TABLES

LIST OF FIGURES

Figure Page

CHAPTER 1

INTRODCTION

1.1 Overview of VLC

Today's wireless network is in the midst of a transformation driven by the proliferation of data. Explosive growth in data-driven applications is placing unprecedented demands on communication networks. The performance of current Wi-Fi technology, however, is fundamentally limited due to the radio frequency (RF) spectrum crisis and is no longer sufficient to support the future "big data" communication. Most recently, light-emitting diode (LED) Li-Fi visible light communication (VLC) [1-10] has emerged as a promising technology to mitigate the looming RF spectrum crisis as well as support a faster, safer and more reliable wireless network for future communications.

Both Wi-Fi and Li-Fi transmit data over the electromagnetic waves, but their spectrums are different. Li-Fi uses visible light, whereas Wi-Fi utilizes radio waves. Figure 1 shows the schematic of how Li-Fi works: an LED light bulb can be switched on and off (on = 1, off = 0 in digital system) within nanoseconds in order to transmit data. Meanwhile, the LED light bulb can still be working for lighting because it flickers too quickly to be noticed by the human eye. The major advantages for LED Li-Fi are: **(1) Large Capacity**: while Wi-Fi is reaching its full capacity due to the overcrowded RF domain, the visible light spectrum is 10,000 times larger in capacity and very lightly used. **(2) High Speed**: Table I summaries data transfer speed for wired, wireless and Li-Fi VLC technologies. Due to the high modulation speed of LEDs, a much higher data transfer speed (> 10 Gbps) could be potentially achieved using Li-Fi system, while the transfer speed of Wi-Fi is limited on the order of hundreds of Mbps. **(3) No RF interference**: Since the visible light does not interfere with other RF or with the operation of sensitive electronic equipment, it is idea for providing

wireless coverage in areas which are sensitive to electromagnetic radiation including hospitals, airplanes, petrochemical and nuclear power plants, etc. **(4) High Security**: The inability of light to propagate through walls will further eliminate interference between neighboring cells, and offer a more securer network. **(5) Low Cost**: the concept of combining the functions of illumination and communication of LED lighting offers the potential for tremendous cost savings and carbon footprint reductions. The deployment of Li-Fi VLC access points (APs) can reuse the existing lighting infrastructure and reduce the cost. Therefore, Li-Fi is a promising technology to act a key role in the next generation of communication.

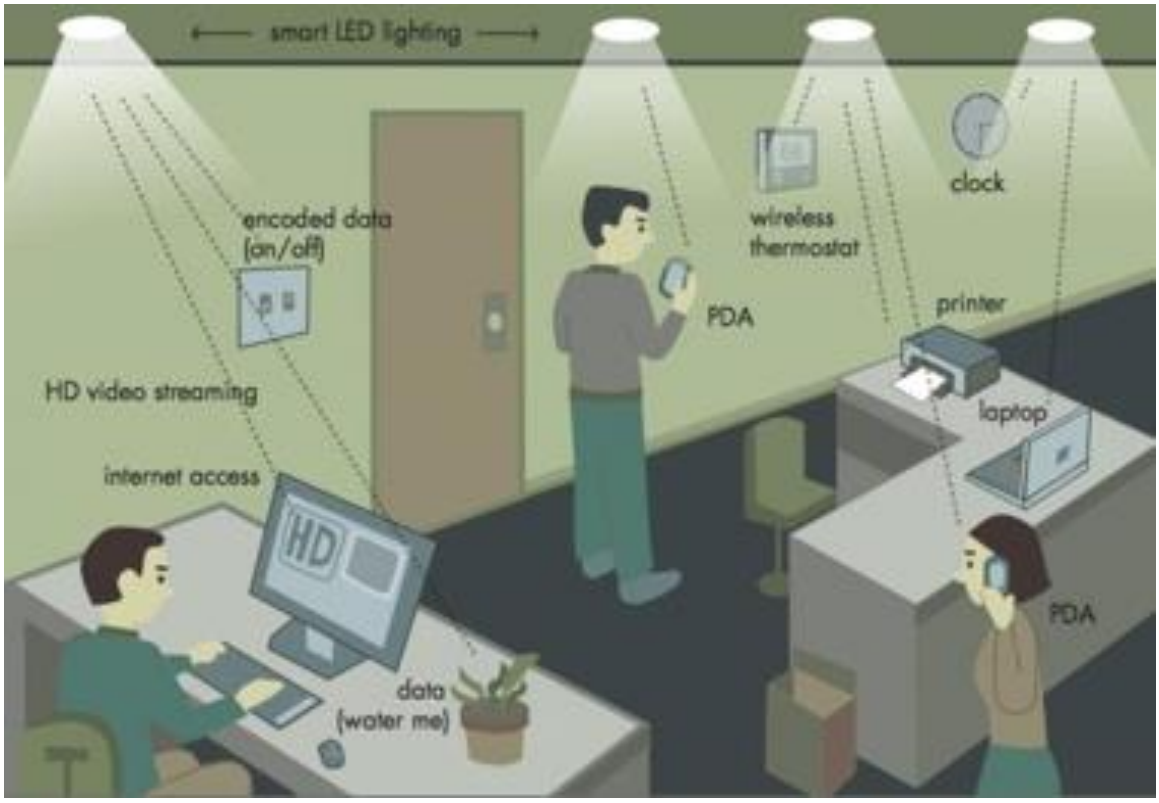

Figure 1. Schematic Picture of How LED Li-Fi Works

	Technology	Speed
Wired	Fire Wire	800 Mbps
	USB 3.0	5 Gbps
	Thunderbolt	10 Gbps
Wireless	Wi-Fi-IEEE (802.11)	150 Mbps
	Bluetooth	3 Mbps
	IrDA	4 Mbps
Future	Visible Light Communication	>10 Gbps

Figure 2. Comparison of Data Transfer Speed for Wired, Wireless, and Li-Fi VLC Technologies

By addressing the key challenges in devices, systems, channels, and integration, the proposed research seeks to significantly advance LED Li-Fi technology. To accomplish the objectives of the proposed research, we plan to pursue the following goals:

- Device: to develop high-speed nonpolar and semipolar LEDs with plasmonic nano-grating structure that can reach a high modulation speed > 2 GHz.
- System: to test and optimize the power consumption of the Li-Fi system for practical applications.

- Channels: to design and test the multiple-input multiple-output (MIMO) channels for both indoor and vehicular communications.
- Integration: to design, fabrication and test the PCB board and IC chip, which is the first of its kind for Li-Fi systems.

We expect these studies to play a key role in accelerate the development of high-speed low-power-consumption LED Li-Fi system as a new wireless communication and network technology. The research and educational activities proposed in this project are expected to have fundamental positive societal and economic impacts.

1.2 Modulation Schemes

One major technical topic for Li-Fi system is the stability and compatibility of the modulation scheme for LED. Due to the incoherent light of LEDs, information can only be encoded in the intensity of the emitted light, while the actual phase and amplitude of the light wave cannot be modulated. This significantly differentiates LED Li-Fi to RF communications. Therefore, the majority of the early work on Li-Fi has been focused on the modulation schemes. In this section, we provide a brief review on existing modulation schemes as well as some related works. We also show our preliminary results obtained on our basic LED Li-Fi setup.

1.2.1. OOK Modulation Scheme

On-off keying (OOK) modulation [11] is the simplest modulation scheme for VLC, where the LEDs are turned on or off dependent on the data bits being 1 or 0. While the modulation is logically OOK, OOK "off" does not necessarily mean the light is completely turned off; rather, the intensity of the light may simply be reduced as long as one can distinguish clearly between the "on" and "off" levels. The schematic

of OOK modulation scheme is as shown in Figure 3. The OOK mode transmitter includes the forward error correction (FEC) and Manchester run length limited (RLL) coding. The Manchester encoding embeds the clock into the data by representing a logic zero as an OOK symbol "01" and a logic one as an OOK symbol "10," providing a DC balanced code.

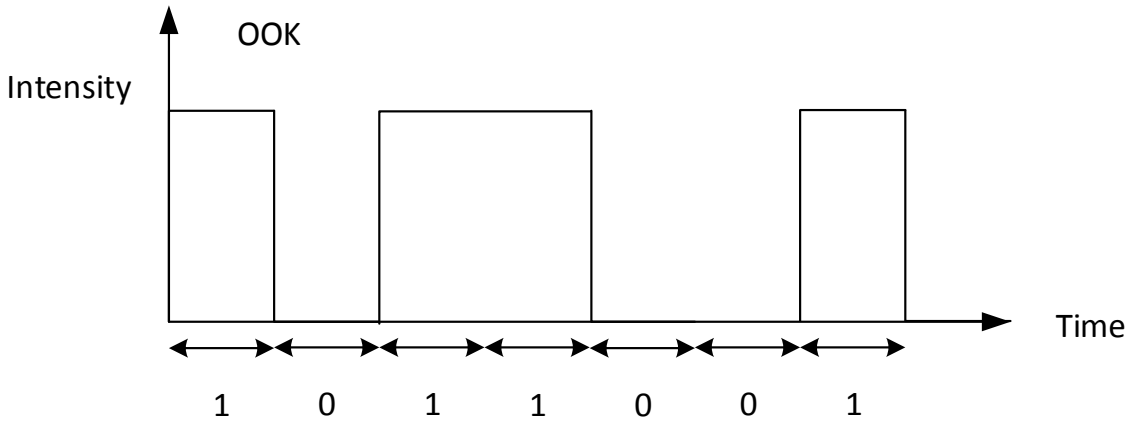

Figure 3. Schematic of OOK Modulation Scheme

1.2.2 OFDM Modulation Scheme

Orthogonal Frequency Division Multiplexing (OFDM) [12-14] is a parallel data transmission scheme in which high data rates can be achieved by transmitting orthogonal subcarriers. OFDM systems do not require complex channel equalizers, the time varying channel can easily be estimated using frequency-domain channel estimation, and adaptive modulation can be applied based on the uplink/downlink requested data rates and quality of service. Also, the possibility to combine OFDM with any multiple access scheme makes it an excellent preference for visible light communication application.

In general, the output of the OFDM modulator is complex. In intensity modulation optical systems, quadrature modulation is not possible (i.e., phase information detection is not possible for intensity modulation with direct detection systems). Therefore, the OFDM commonly used in RF communications must be modified. Both systems are very similar to RF systems designed for wired or wireless communications, but they have their own requirements and methods. A real OFDM signal can be generated by constraining the input to the inverse fast Fourier transform (IFFT) operation to have Hermitian symmetry.

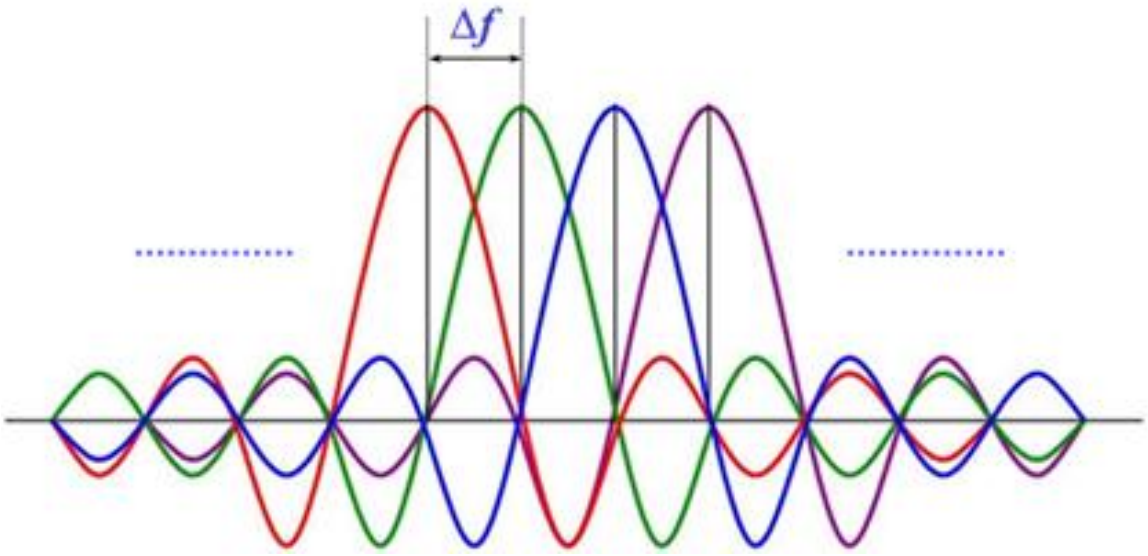

Figure 4. Schematic of OFDM Modulation Scheme

1.2.3 VPPM Modulation Scheme

The use of modulation techniques such as pulse position modulation (PPM) for dimming support has been proposed for VLC. Variable pulse position modulation (VPPM) [15, 16] changes the duty cycle of each optical symbol to encode bits. The variable term in VPPM represents the change in the duty cycle (pulse width) in

response to the requested dimming level. VPPM optical symbols are distinguished by the pulse position. VPPM is similar to 2-PPM when the duty cycle is 50 percent. The logic 0 and logic 1 symbols are pulse width modulated depending on the dimming duty cycle requirement. The pulse width ratio (b/a) of PPM can be adjusted to produce the required duty cycle for supporting dimming by pulse width modulation (PWM). Figure 5 shows an example waveform of how VPPM can attain a 50 percent dimming duty cycle requirement, where both logic 0 and logic 1 have a 50 percent pulse width.

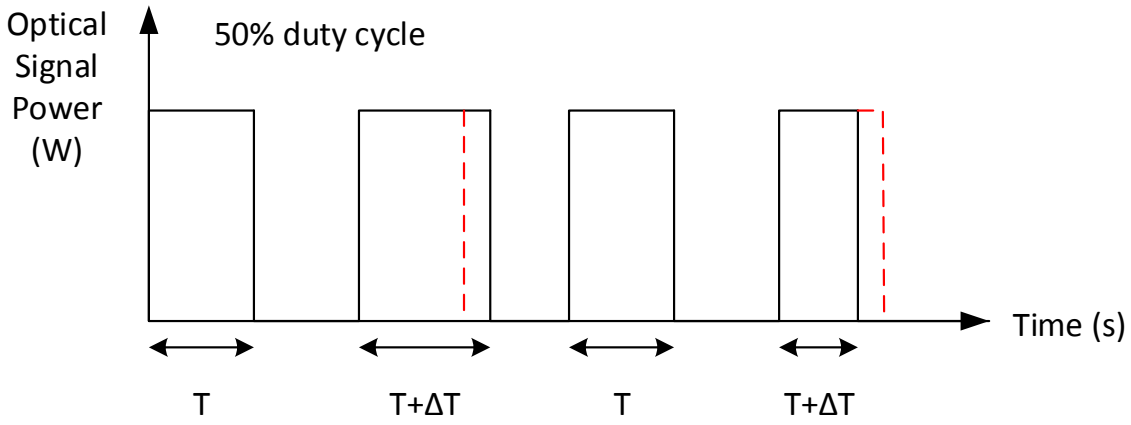

Figure 5. Schematic of VPPM Modulation Scheme

1.3 Channel: MIMO Channel Study

1.3.1 Introduction

Proper design of wireless systems (e.g. signal set selection, or receiver equalization) starts with an understanding of the channel at hand. In wireless systems, the channel phenomena of interest include delay spread, Doppler spread, and MIMO channel characteristics. In this aspect of work, we propose using the following MIMO system to study the channel:

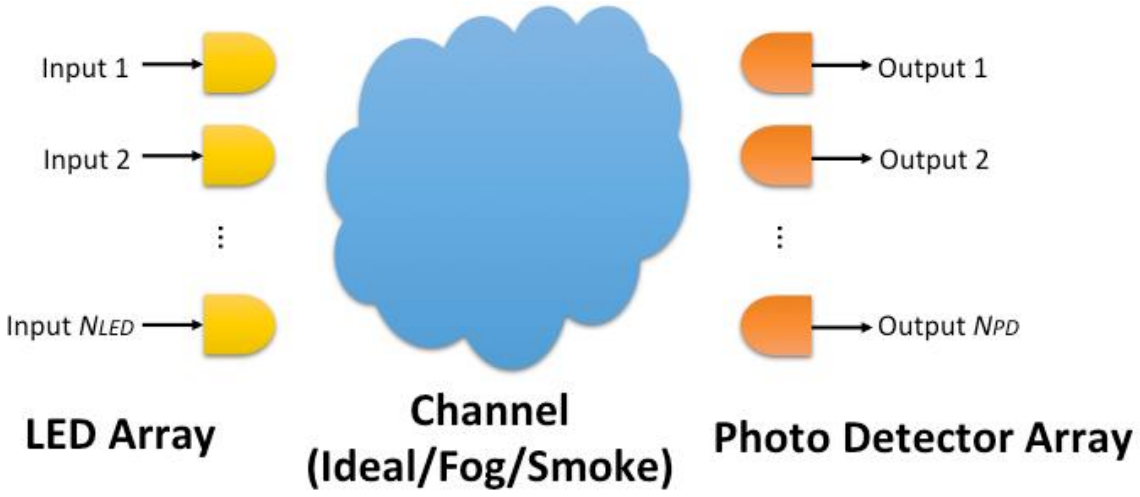

Figure 6. NLED x NPD System: Input Processing Circuitry and Output Processing Circuitry Omitted for Simplicity.

Referring to the above NLED to NPD system, we shall perform channel estimation over a variety of physical arrangements between the LEDs and the PDs, recording the channel estimation data for later analysis. As the channel varies greatly depending on the physical arrangement of the LEDs, the PDs, and other objects such as ceilings, walls, and so forth, we shall endeavor to reproduce arrangements representative of potential applications of Li-Fi. For example, since Li-Fi has potential applications in office areas, in congregation areas such as coffee shops, and in vehicular communications, we shall endeavor to replicate relevant aspects of those scenarios. The fog/smoke scenarios are of interest to vehicular communications, as automobiles often operate in fog, rain, and snow.

1.3.2 Indoor Channel Measurements

We shall perform channel measurements, for each of an office scenario, a coffee shop/eatery scenario, and an auditorium scenario. These scenarios correspond

to small/medium/large indoor areas. Emphasis shall be placed on the coffee shop/eatery and auditorium scenarios, as Li-Fi has particular value here, given the inconvenience of a wire-line network connection. In each scenario, the LED array shall be located consistent with indoor lighting locations, and the PD array shall be located consistent with user terminal locations. Channel data shall be measured and recorded, along with approximate room measurements and LED and PD locations. Images (pictures) of the scenario shall also be recorded.

1.3.3 Vehicular Communications Channel Measurements

We shall perform channel measurements for each of a vehicle-to-vehicle scenario, and a vehicle-to-traffic-light (i.e. vehicle-to-infrastructure) scenario. For the vehicle-to-vehicle scenario, the LED array shall be mounted on one vehicle, consistent with vehicle lighting locations. The PD array shall be mounted on a second vehicle consistent with vehicle lighting locations. Channel measurements shall be performed over a variety of vehicle velocities. For the vehicle-to-traffic-light scenario, the LED or PD array shall be mounted on the vehicle, consistent with vehicle lighting locations. The PD or LED array shall be mounted on the traffic light consistent with lighting locations on that fixture. If obtaining use of a traffic light location is too inconvenient, we may use a substitute, such as a light pole, to mimic the traffic light location as well as is practical. Channel measurements shall be performed over a variety of vehicle velocities.

As vehicles must operate in rain, snow, fog, and other scenarios with channel impediments, we additionally want to characterize the channel in these scenarios. However, we do not sufficiently control the weather to generate these channels as needed. Therefore, we shall give reasonable effort to measure the channel in these scenarios, or mimic and measure such scenarios as is practical in the laboratory

environment. Emphasis shall be given to repeatability; i.e. as fog or rain can vary greatly, we shall endeavor to record the degree of impediment such that it can be objectively known.

CHAPTER 2

LINE-OF-SIGHT VISIBLE LIGHT COMMUNICATION ACTIVE TRACKING

2.1 Introduction

The demand for high data rate wireless communication has increased over the past decade for the applications such as Internet of things (IoT), big data, augmented reality (AR), virtual reality (VR), and vehicle-to-vehicle (V2V) communication. Though the 5G radio frequency (RF) communication network takes use of millimeter wave carrier frequencies to 60 GHz, the limited frequency spectrum crisis restricts the development of wireless communication. In order to meet this challenge, visible light communication (VLC) has been brought as a promising method for wireless communication [17]. The utilization of optical carrier frequencies allows for a much wider available spectrum, a high degree of spatial multiplexing, and the possibility to communicate at a higher speed [18].

Light emitting diodes (LEDs) are utilized as the optical source in VLC. Because the system bandwidth is mainly limited by the electrical to optical bandwidth of an LED, Gallium Nitride (GaN) based micro-LEDs become the hot choice for the VLC optical source. Scaled with their size, GaN based micro-LEDs' smaller carrier lifetime and lower junction capacitance lead to a bandwidth on the order of 100 MHz [19]. On-off keying (OOK), pulse-amplitude modulation (PAM) and orthogonal frequency division multiplexing (OFDM) have been taken into use to achieve high-speed communication up to 11.95 Gbps for a single micro-LED [20], demonstrating the significant advantages of micro-LEDs in the application of VLC.

Due to the smaller size of a GaN-based micro-LED, the order of optical power drops from 100 mW to 1 mW dramatically. Although this can be compensated for with focusing optics, the drawback is a reduced field of view (FOV) because of the conservation of etendue in geometrical optics. The loss of FOV related to the

constant increased active aperture is often made up for by active tracking systems in optical communications [21–23]. We demonstrate a method to enhance the active area and FOV, widely used to concentrate light in solar panel. A novel light tracking sensor and the custom circuit were integrated in a chip by a standard 0.18 μm CMOS process. The results showed the system has nice sensitivity to the incident angle and achieve the tracking accuracy of 1.9° over a range of 120° [24, 25].

In this dissertation, we present an active tracking system consisting of a motor and a CMOS chip with a light sensor and the signal processing circuits [26]. The majority of the circuits were integrated on the same chip to process the sensing signal and control the motor. This is available for high speed visible light communication using a GaN-based LED and NRZ-OOK, insensitive to the spatial mode of the incident light obtaining 600 Mbps at a bit error rate (BER) of 2.1×10^{-4} below the limit of forward error correction (FEC). For the indoor use, 3D high-definition (HD) video streaming to VR helmet requires high throughout wireless channels without harmful radiation that would not exert a health threat. Being a green communication link, the VLC system is applied to track the VR helmet movement and offer large HD video data. For the outdoor application, Facebook Company conducts a breakthrough project called 'Connecting the World'. As shown in Figure 7, two auto pilot flights are in the sky 20 Km far away and connected by point-to-point VLC link using laser diodes (LDs). This brings in a new set of challenges; the tracking system should be precise enough to hit a dime-sized object 20 Km away. Air flow between the flights interferes with the point-to-point VLC link and needs the active tracking.

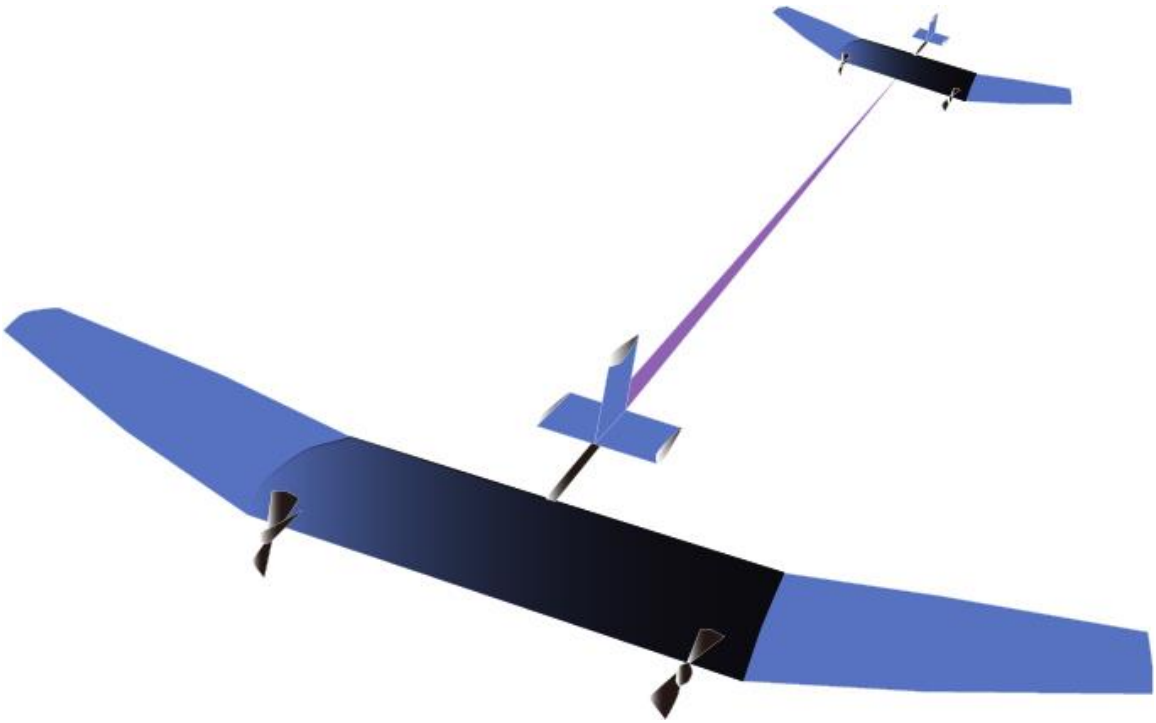

Figure 7. For Outdoor Use, 20 Km Long Range Point-to-point VLC Link Using an LD Is Needed in the Latest Project Named 'Connecting the World' Conducted by Facebook

2.2 GaN-based Micro-LED Design and Fabrication

We applied a GaN-based micro-LED with a pixel size of 80μm × 80μm. It is fabricated from a commercially available LED wafer grown on a c-plane sapphire substrate. The LED had a traditional p-i-n structure with an n-GaN layer, InGaN/GaN multiple quantum wells (MQWs), an AlGaN electron blocking layer and a p-GaN layer. Ni/Au (10nm/25nm) layers were deposited on top of the p-GaN. Afterwards, dry etching was used to etch the Ni/Au layer and the GaN layers to build the mesas. P-contacts were built by thermal annealing in purified air at 500 °C. Then, SiO_2 was deposited by plasma-enhanced chemical vapor deposition (CVD) as the passivation layer, and apertures on the mesas were further formed by HF-based wet etching. In the end, Ti/Au (50nm/200nm) deposited as the p-pad and n-pad to address each

pixel separately. The micro-LEDs were bonded on a custom-designed PCB and only the light emission from the sapphire side was employed for VLC. The peak wavelength of the micro-LED is around 440 nm at a driving current 40 mA [19]. To measure the -3dB modulation bandwidth of the packaged micro-LED, a small signal modulated output from an Agilent N5225 network analyzer was added with direct current from a Yokogawa GS610 source to power the micro-LED. The light emission was detected by a 1.4 GHz photo sensor. Then, the frequency response was measured from the network analyzer.

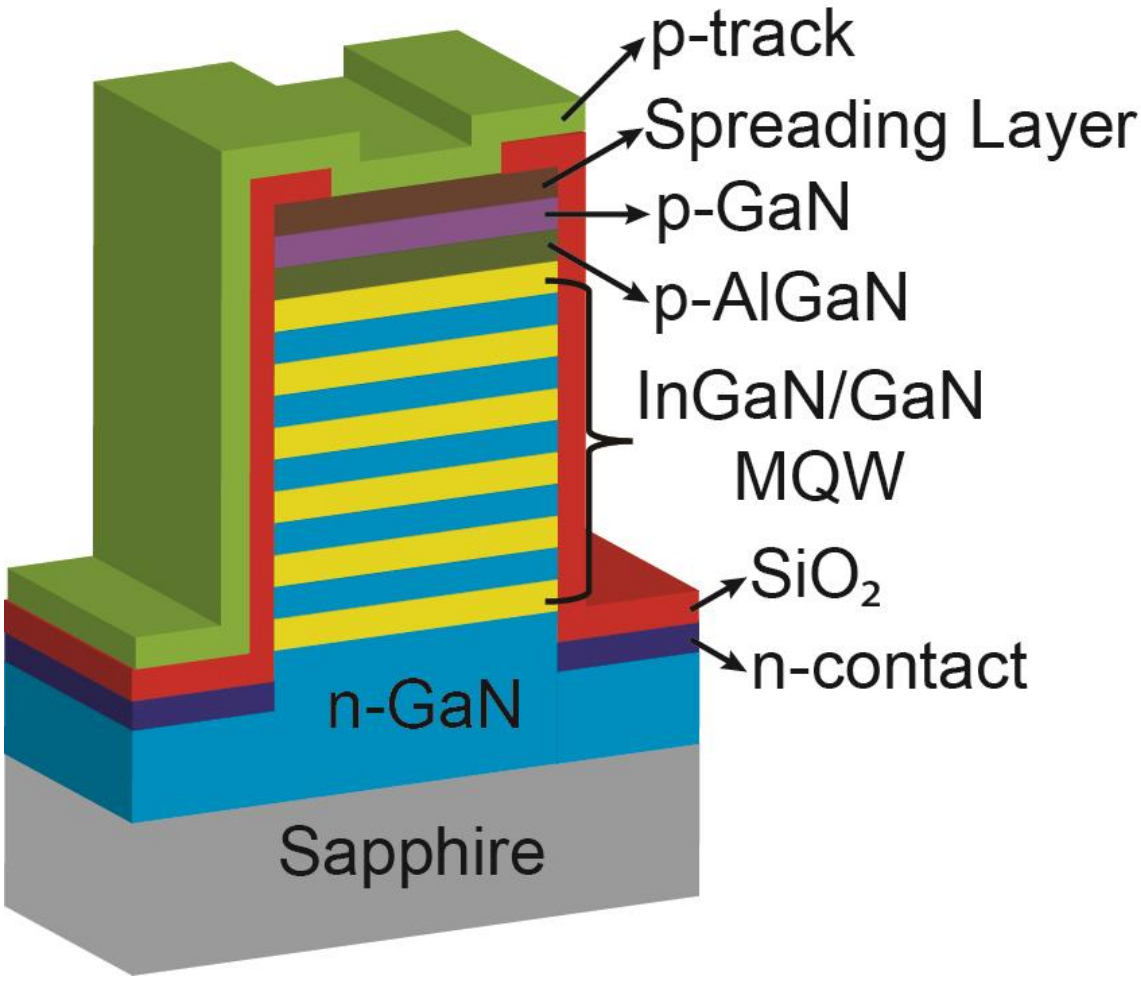

Figure 8. 3-D Schematic Structure of the Fabricated Micro-LEDs

2.3 The Setup of VLC Link

Figure 9 shows the proposed VLC link using a single GaN-based micro-LED and NRZ-OOK modulation scheme, accompanied with an active tracking system. An Anritsu Signal Quality Analyzer MP1800A (Pulse Pattern Generator) generated high quality, low intrinsic jitter PN15 outputs. The peak-to-peak voltage is 2.0 V. A DC bias, GS610, was combined to the AC input signal by a Bias-T, Mini-Circuits ZFBT-6GW, which drives the blue GaN-based micro-LED. The light beam was focused at both transceiver and receiver within a 1 m transmit distance and captured by a 1.4 GHz bandwidth photodetector, HAS-X-S-1G4-SI-FS. The electrical output signal of the detector was measured by an Anritsu Signal Quality Analyzer MP1800A Error Detector and Wide-Bandwidth Oscilloscope 86100A to acquire BER and eye diagrams, separately. In BER measurement of NRZ-OOK, the delay model in MP1800A brings in a delay of N samples to the input signal, PN15 data pattern, to generate the reference. With the bit streams synchronization, the reference (REF) and test (TEST) inputs are calculated for BER measurement.

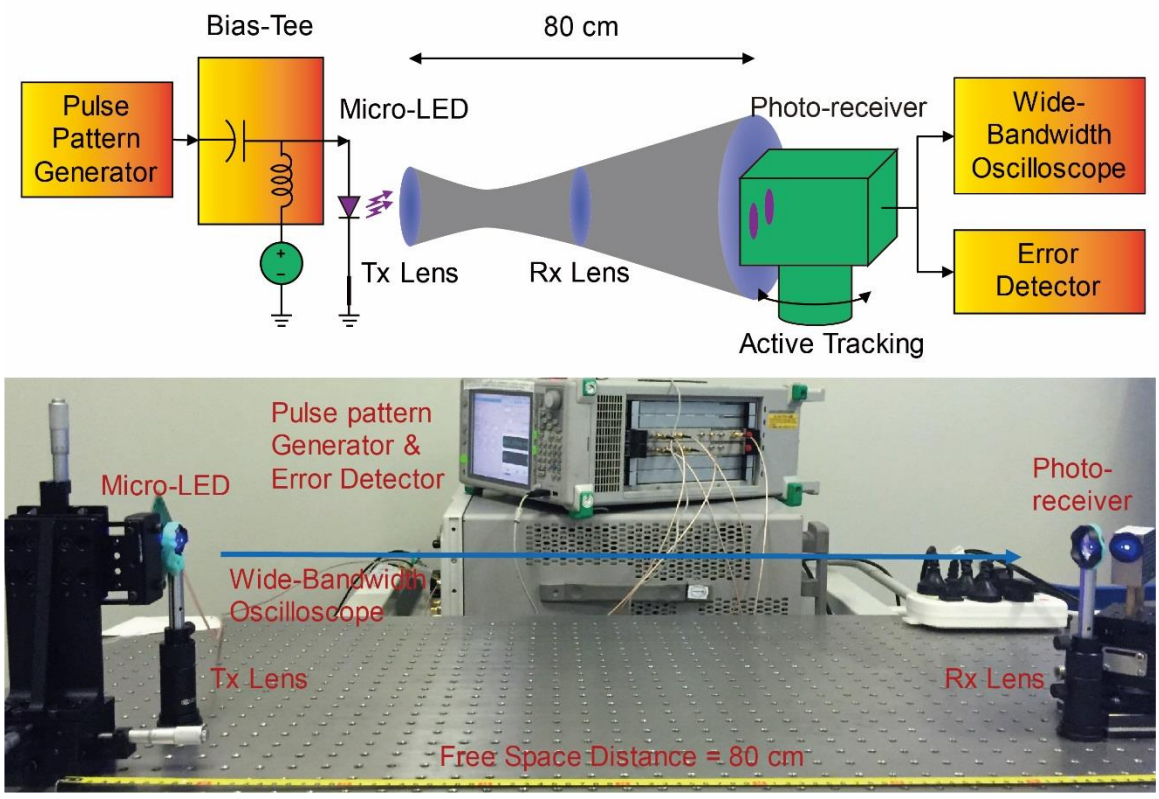

Figure 9. Experimental Setup Including a VLC Link Using a GaN-based Micro-LED and NRZ-OOK, an Active Tracking System Using an On-chip Photo Sensor

2.4 Characteristics of GaN-based Micro-LED

To measure the electrical to optical performance of the single 80 μm × 80μm GaN-based micro-LED, we firstly packaged the die of micro-LED to printed circuit board (PCB) as demonstrated in Figure 10. It is made up of a GaN-based micro-LED array, a high-speed PCB board, and a soldered SMA connector. The power-current (P-I) and voltage-current (V-I) response shown in Figure 11 illustrate that the sheet resistance Rseries = dV/dI at bias currents from 30 mA to 102.7 mA kept steady around 19.1 Ω. When we exerted a small modulated signal to the current, it would lead the variation of the optical power. Because of the linearity of the P-I response, the GaN-based micro-LED modulation performance is fit to VLC. The characteristics

of extracted -3dB modulation bandwidth with bias currents are described in published paper [29]. When bias current goes up from 1 mA to 61 mA, the bandwidth shifts up dramatically. When the bias current is higher than 61 mA, the bandwidth stays at 160 MHz. Higher current leads to more self-heating to the micro-LED, thus higher junction temperature makes the micro-LED's lifetime and reliability worse [30]. So we chose 40.8 mA bias current and 4.6 V bias voltage for the operation point of VLC system, at which the -3dB bandwidth of the micro-LED is 140 MHz. The electroluminescence spectrum measurement shows that the GaN-based micro-LED emits mostly 440 nm wavelength blue light at the bias current of 40.8 mA [32-35].

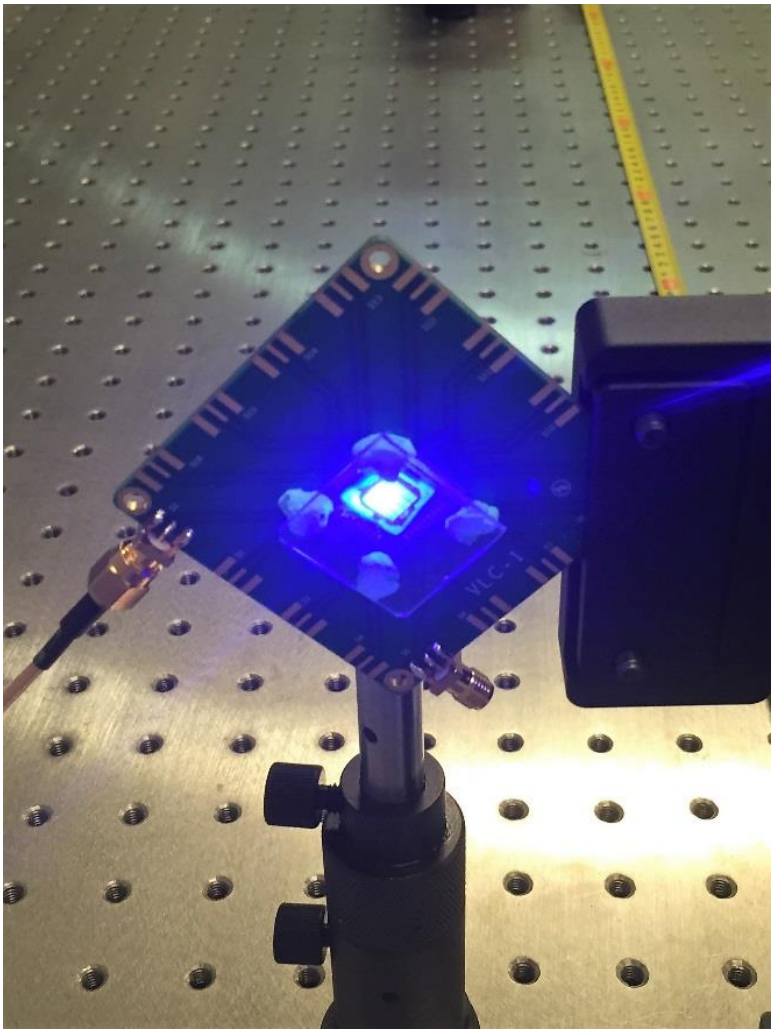

Figure 10. Image of the Packaged 440-nm Blue GaN-based Micro-LED

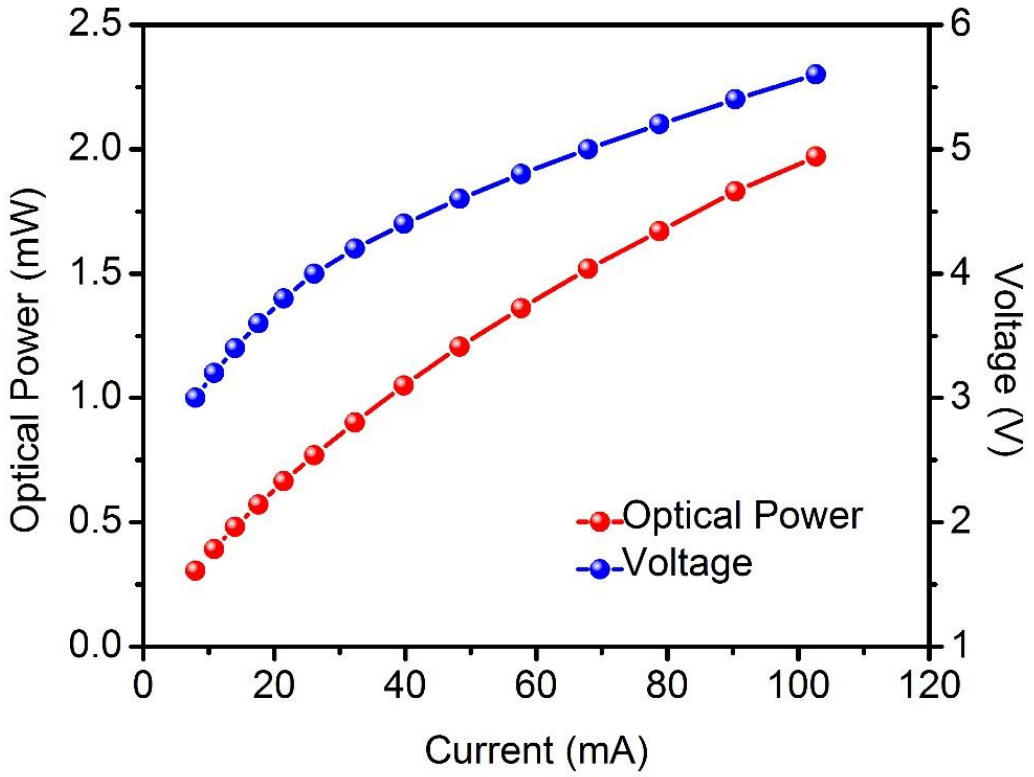

Figure 11. P-I Curve and V-I Curve of the GaN-based Micro-LED

2.5 440-nm Blue Micro-LED Based VLC System over an 80-cm Free Space Distance

Appling an active tracking system with an on-chip photo sensor, a VLC link using a GaN-based micro-LED and NRZ-OOK scheme is experimentally built as demonstrated in Figure 12. Due to the blue GaN-based micro-LED is applied as both a data transmitter and a lighting source in the VLC system, most of the optical emission is distributed within a large angle of around 120° [31]. Because of its smaller optical power compared to commercial LEDs and Laser diodes, the optical emission is collected by the focusing lens to make sure that the PIN receiver can acquire the most optical power. As a trade-off, its low divergence angle limits the

allowable lighting range after collimation. So the focusing lens placed next to GaN-based micro-LED would correspond to the communication quality. It also affects its divergence angle as well. The transmission performance of VLC link depends on the direction of the measurement setup placed with respect to the GaN-based micro-LED. In this dissertation, the active tracking system adhered to the photo detector locates in front of the micro-LED with a free-space distance of 80 cm to investigate its maximal allowable VLC capacity.

For VLC link using GaN-based micro-LED and NRZ-OOK, manual focus provides the high-quality and high-speed wireless communication demonstration within 80-cm free-space transmit distance. NRZ-OOK is used. Eye diagrams are shown in Figure 12. Error free eye diagrams at 200 Mbps, 300 Mbps, 400 Mbps, and 500 Mbps can be achieved at 40.8 mA DC bias. In Figure 13, the BER at different driving currents was measured from 13 mA to 102 mA. A higher throughout communication link can be achieved at a higher driving current, because of the increase of modulation bandwidth and optical output power. From 70 mA to 102 mA, a slightly higher speed than 600 Mb/s was obtained because the bandwidth already saturated at 70 mA. At 78 mA, a data rate of 600 Mb/s was obtained with a BER 3.4×10^{-7} (below FEC 3.8×10^{-3}). Even though manual focus brings good performance in VLC, at 40.8 mA within 80-cm free-space transmit distance, the received power is 1.15 mW. At data rates of 200 Mbps, 300 Mbps, and 400 Mbps, BERs are below than 1×10^{-13}. So the NRZ-OOK VLC link is error free. At data rates of 500 Mbps and 600 Mbps, BERs are 1×10^{-10} and 2.1×10^{-4} as shown in Figure 14. We also apply neutral density filters to decrease the received power to its one-fourth for VLC BER measurement. Figure 14 demonstrates that BER drops dramatically to 2.8×10^{-3} at 500 Mbps when the received power decreases to its one-fourth. Since the received

optical power decreases, then the received effective signal intensity becomes less. Thus, the signal to noise ratio (SNR) and BER become worse.

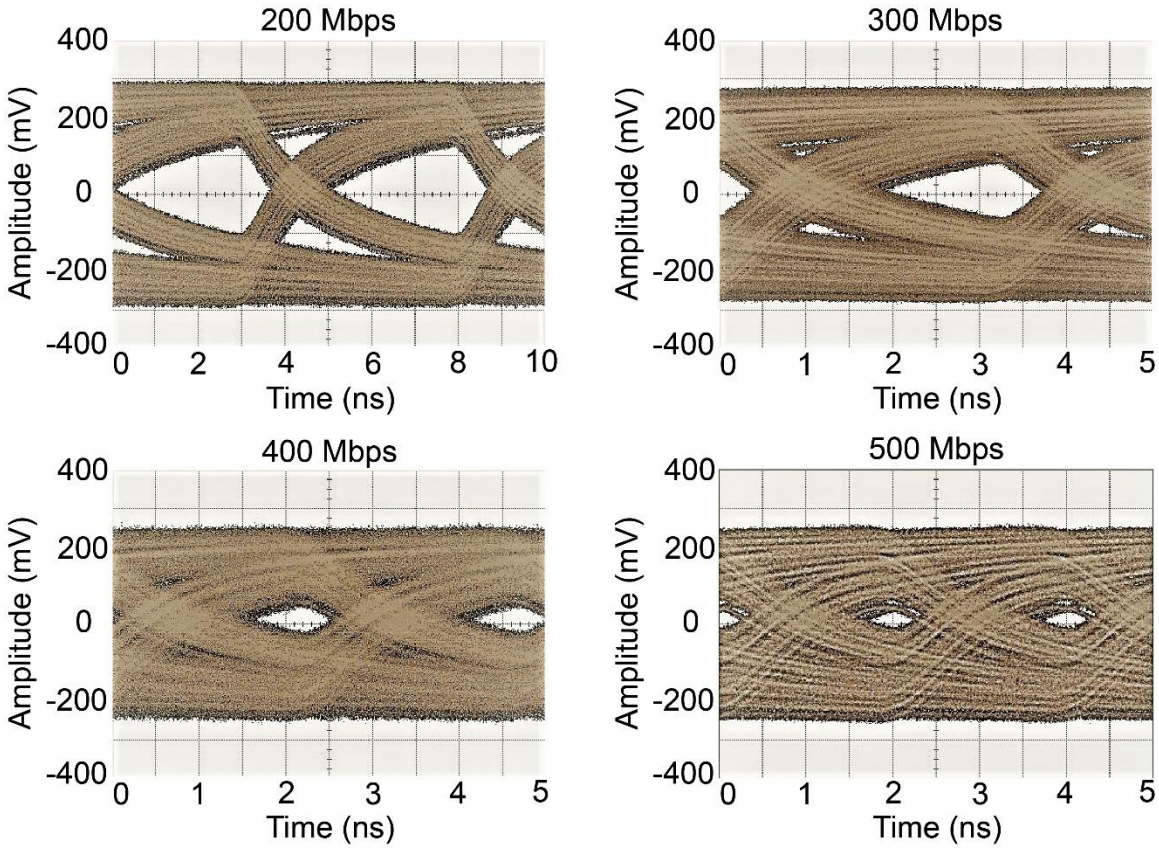

Figure 12. Open Eye Diagrams with 200 Mbps, 300 Mbps, 400 Mbps, and 500 Mbps Acquired at 40.8 mA DC Bias

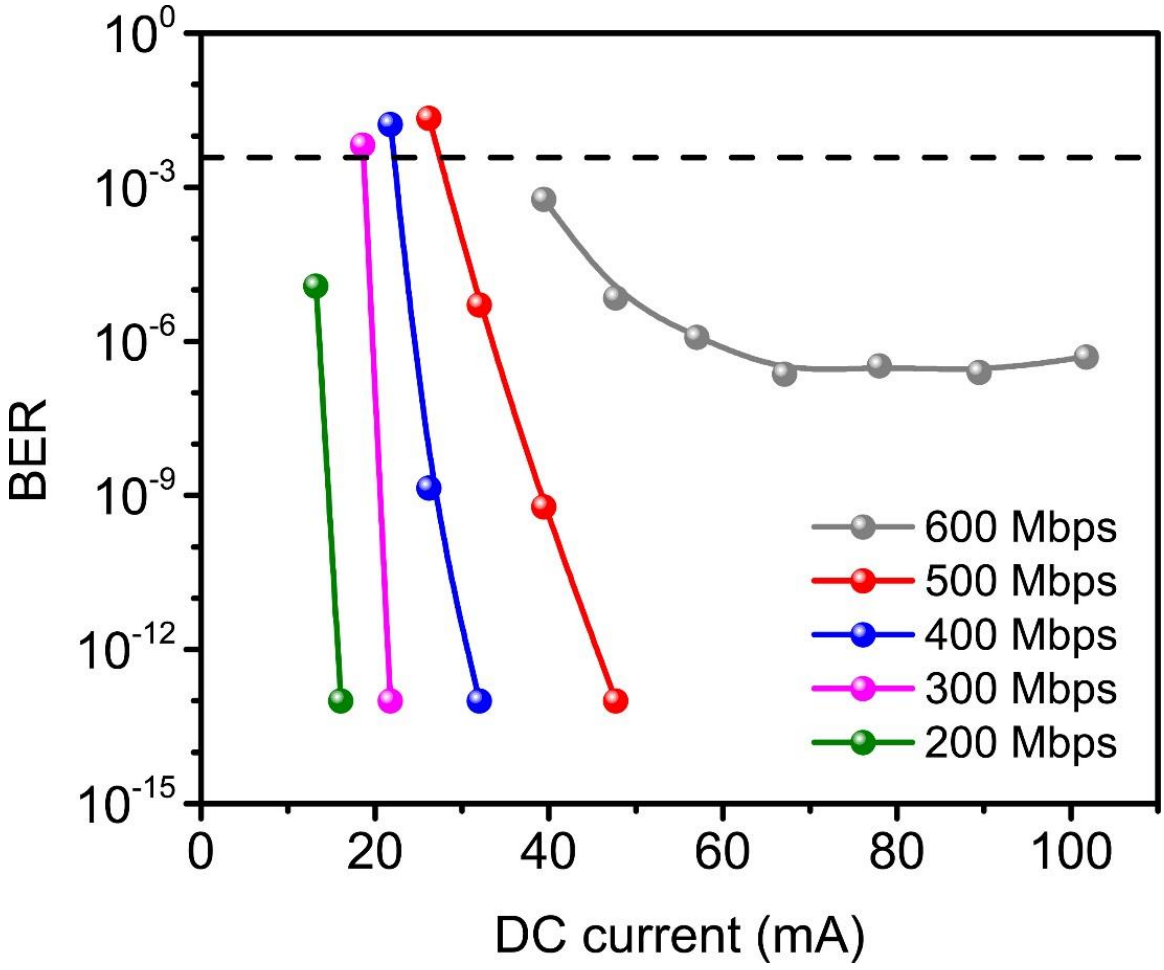

Figure 13. The BER at Different Bias Current

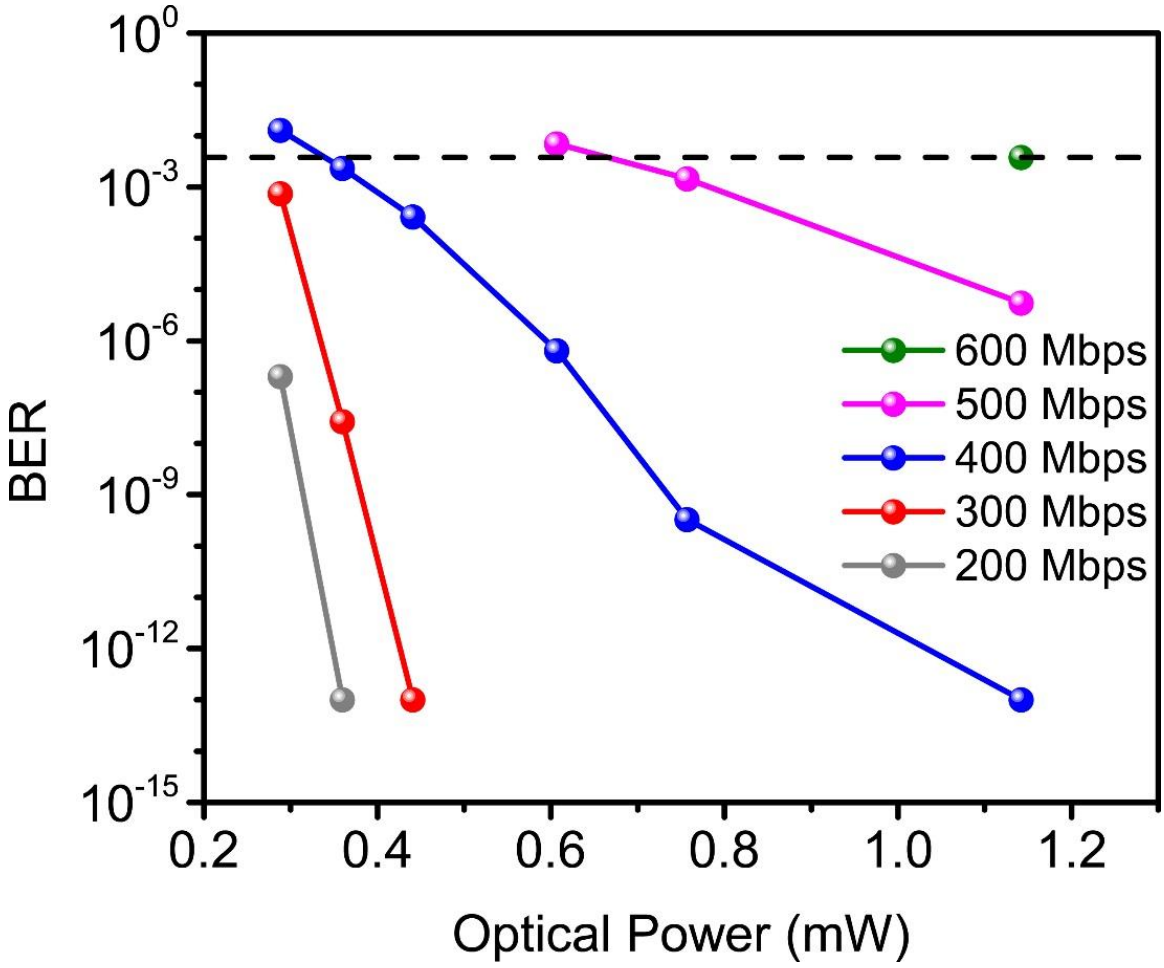

Figure 14. The BER at Different Received Optical Power

2.6 Active Tracking System

A CMOS sensor is to sense the incident light and point in the direction of the light. Figure 15 shows a basic cell of the sensor. The whole sensor consists of a set of the basic cells. A metal wall built by stacking all metal layers, contacts, and vias available in the process is applied to generate the on-chip micro-scale shadow. The height of the metal wall denotes to h. We choose the dimensions of the metal wall for the sensor's performance. In this work, we use 12 μm as the height of the metal wall. Diffraction has been also taken into account. The bandgap voltage of silicon is

1.12 V. So the sensor can absorb the light wavelength to 1.1 μm covering 440 nm blue light generated by GaN-based micro-LED. But the distance between two adjacent metal walls is 30 μm, and the height of the metal wall is 12 μm. The physical dimensions are larger than the wavelength of the absorbed light, therefore, the diffraction exerts little impact on the sensor's performance.

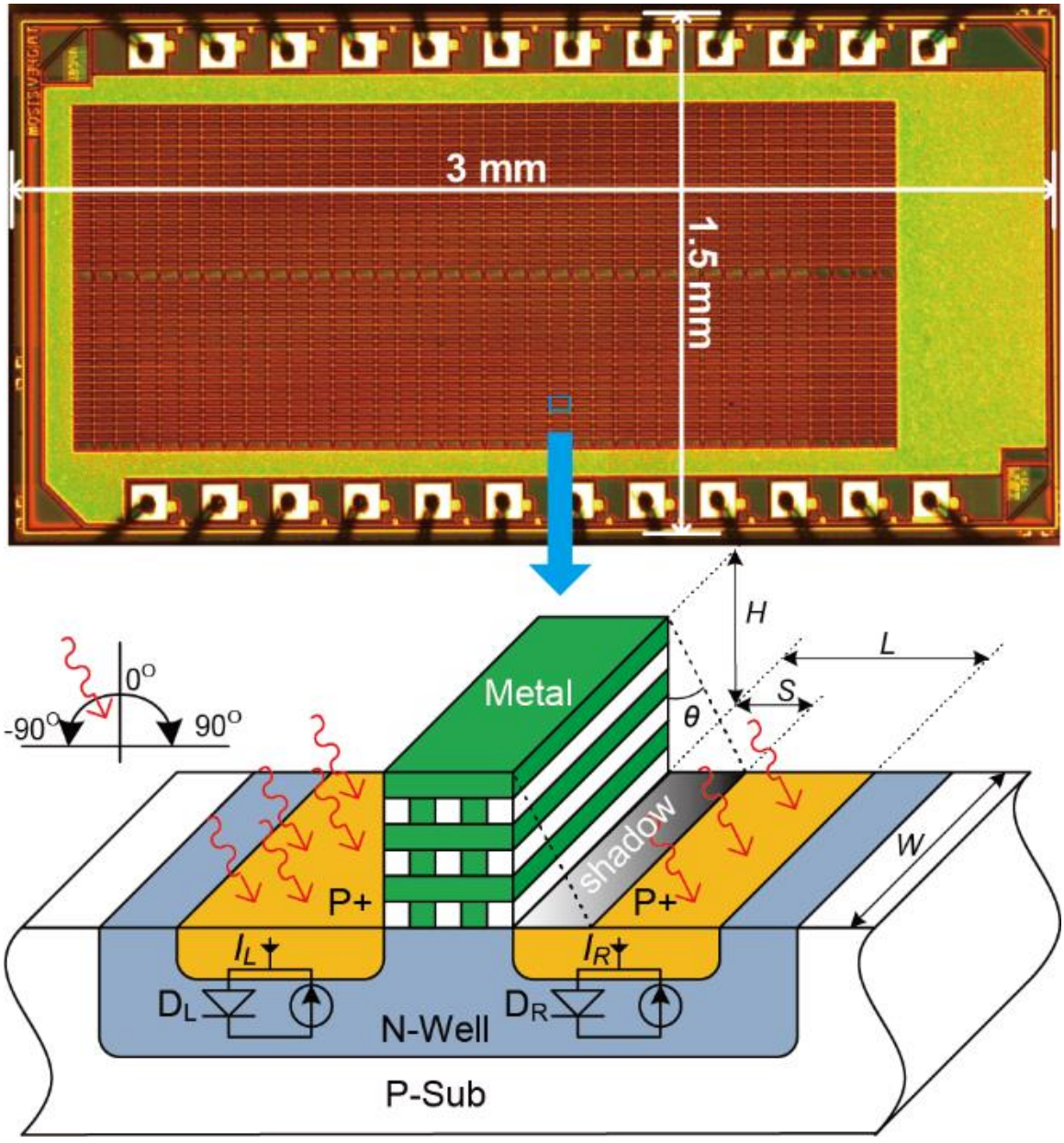

Figure 15. On-chip Light Tracking Sensor Structure and Micrograph

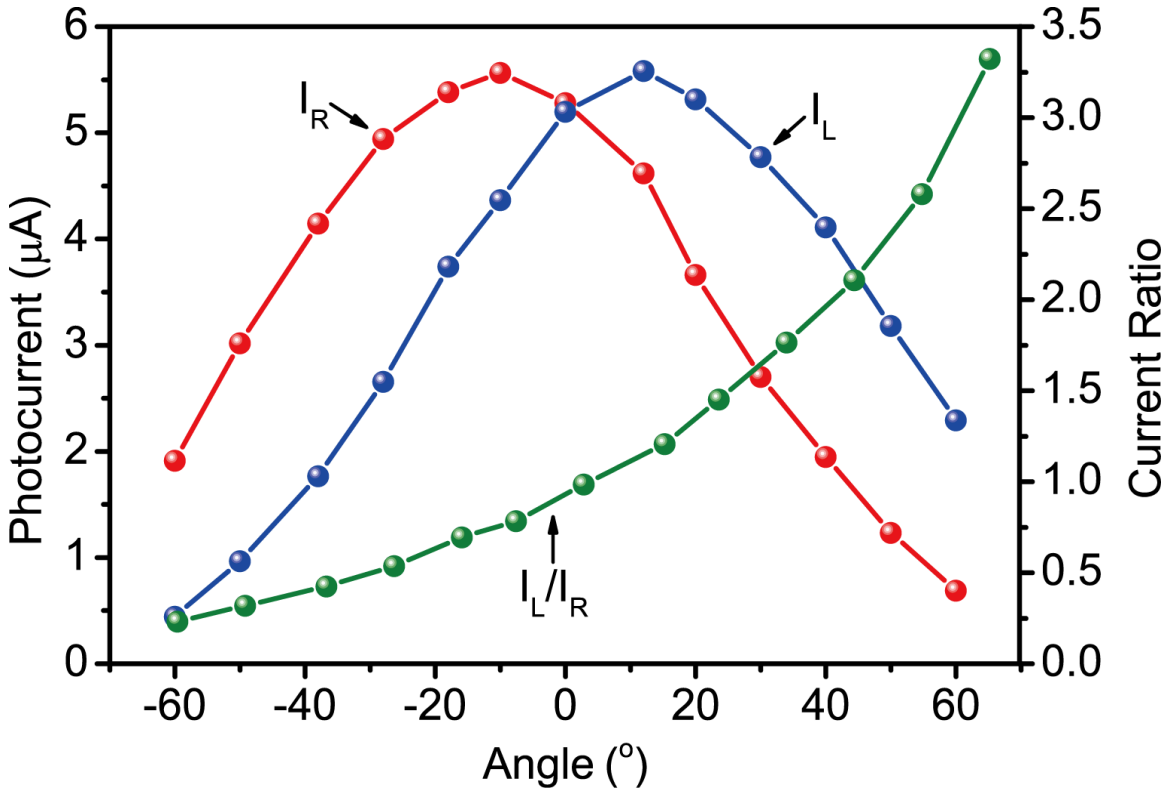

Figure 16. Photocurrents and Current Ratio versus Incident Light Angles under the Power Density of 80 mW/cm^2

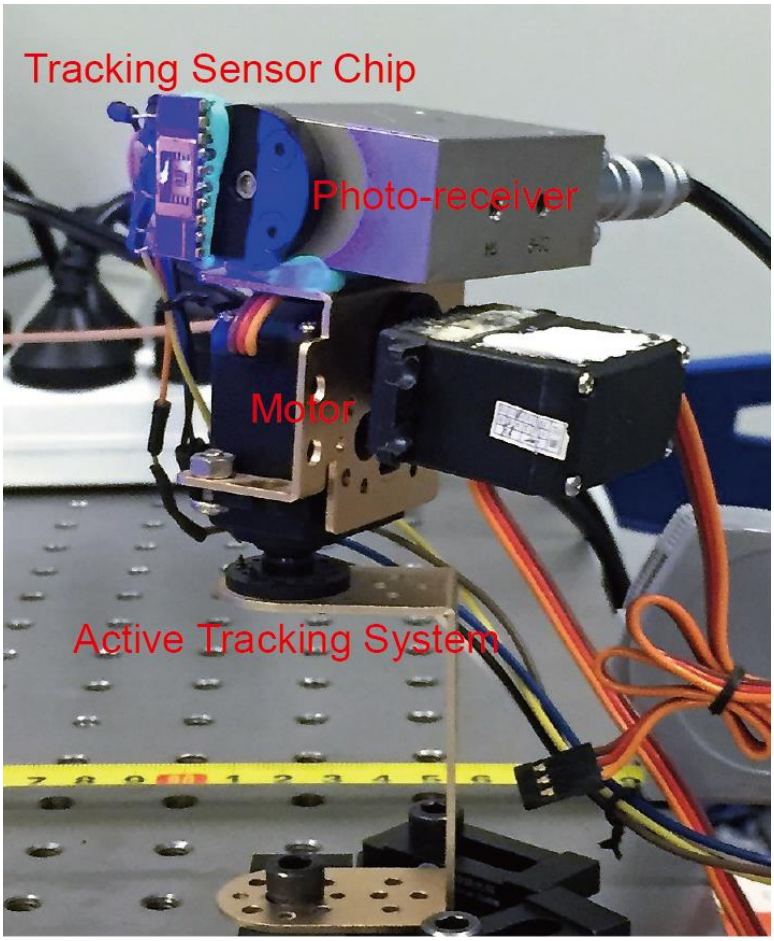

Figure 17. Photograph of the Active Tracking System

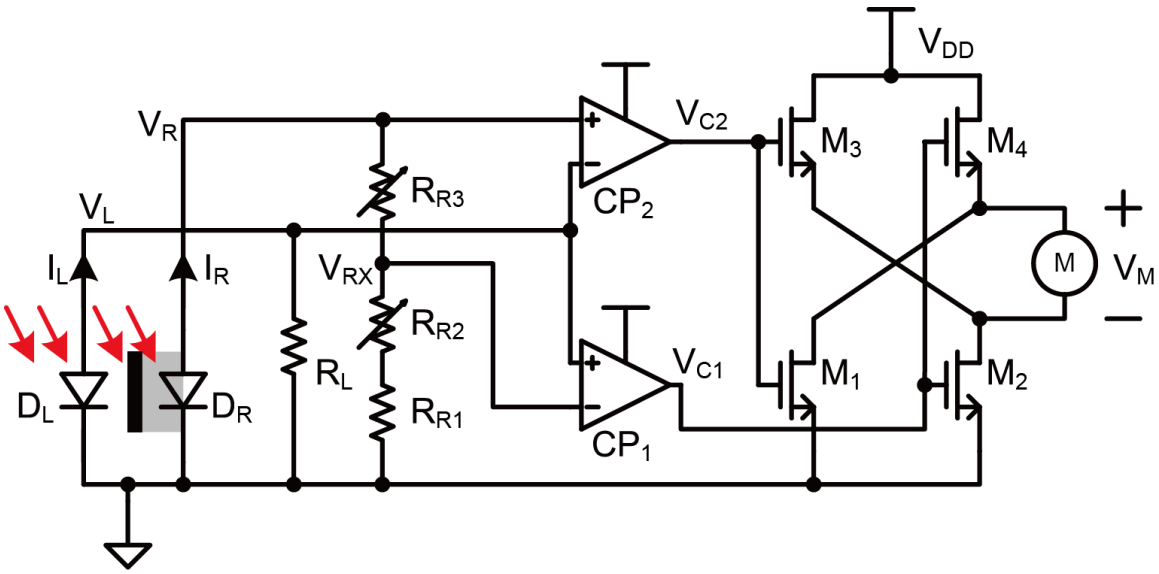

Figure 18. Block Diagram of the Proposed Tracking Circuit

Two same photodiodes locate on both sides of the metal wall. D_L is the left side diode while D_R is the right side diode. They have the identical width W and the same length L. The schematic current sources beside each diode show the photocurrents are produced by the related photodiodes. The angle between the metal wall and the light direction is θ. When the light comes from directly above of the wall, namely θ = 0, the two photodiodes are even and generate the identical current values. When the light comes from one side above the wall, namely θ > 0 or θ < 0, the wall blocks some of the light to the other photodiode will offer less current. So the relationship between of I_L and I_R is related to the incident light angle θ given by [28]

$$\frac{I_L}{I_R} = \begin{cases} \dfrac{(1+\beta)L \cdot \cos\theta + \alpha H \cdot \sin\theta}{(1+\beta)L \cdot \cos\theta - H \cdot \sin\theta}, & \theta \geq 0 \\ \dfrac{(1+\beta)L \cdot \cos\theta + H \cdot \sin\theta}{(1+\beta)L \cdot \cos\theta - \alpha H \cdot \sin\theta}, & \theta < 0 \end{cases} \quad [1]$$

in which α corresponds to the ratio of the reflected light to the total light reaching the left side of the metal wall, β corresponds to the ratio of the reflected light to the total light reaching the right side of the metal wall. α and β depend on the package, process, and layout. Both values are assumed to remain constant in a known design. So, from Eq. 1, the current ratio of IL/IR is independent of the light intensity and only dominant by the incident light angle θ. Figure 16 shows the photocurrents IL, IR and its current ratio versus the angle of the incident light when the constant light intensity is 80 mW/cm^2. It was measured with KEITHLEY 2636A Source Meter. Both photocurrents vary with the light angle. When the angle is 0, IL

and ID are almost the same. When the light comes from left side $\theta < 0$, IL is larger than IR. When the light comes from right side $\theta > 0$, IL is larger than IR.

The active tracking system for VLC consists of an on-chip light tracking sensor, the integrated circuits, a motor, and the mechanical transmission as shown in Figure 17. Figure 18 demonstrates the circuit schematic of the tracking system. Photodiodes DL and DR, photocurrents IL and IR are identical as shown in Figure 16. It shows that when $\theta < \theta 1$, the motor is driven by $VM > 0$, thus the angle will increase to the balance. When $\theta > \theta 2$, the motor is driven by $VM < 0$ and the angle will decrease to the balance. When $\theta 1 < \theta < \theta 2$ and $VM = 0$, the motor will be steady and there will be little power consumption by the motor driver. It is the steady region. For a fixed-location solar-cell sun tracking application, the needed rotating speed is very slow, so most of the time this system stays in a very low power state, in which the motor driver does not consume power, and only the comparators continuously work. In this design, the consumed current is only 88 μA for the low power applications. The results showed that the system has good sensitivity to the incident angle and achieve a tracking accuracy of 1.9° over a range of 120°.

2.7 An Active Tracking System for 440-nm Blue Micro-LED Based VLC System over an 80-cm Free Space Distance

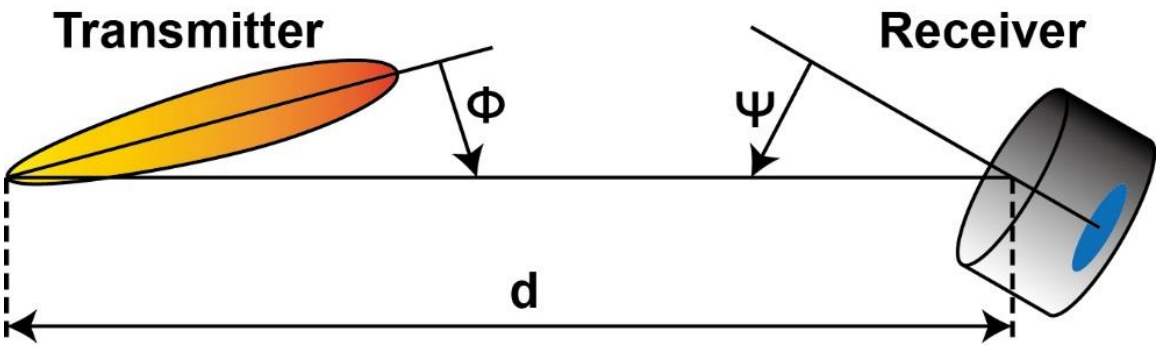

Figure 19. LOS Geometry Used in Channel Gain Calculations

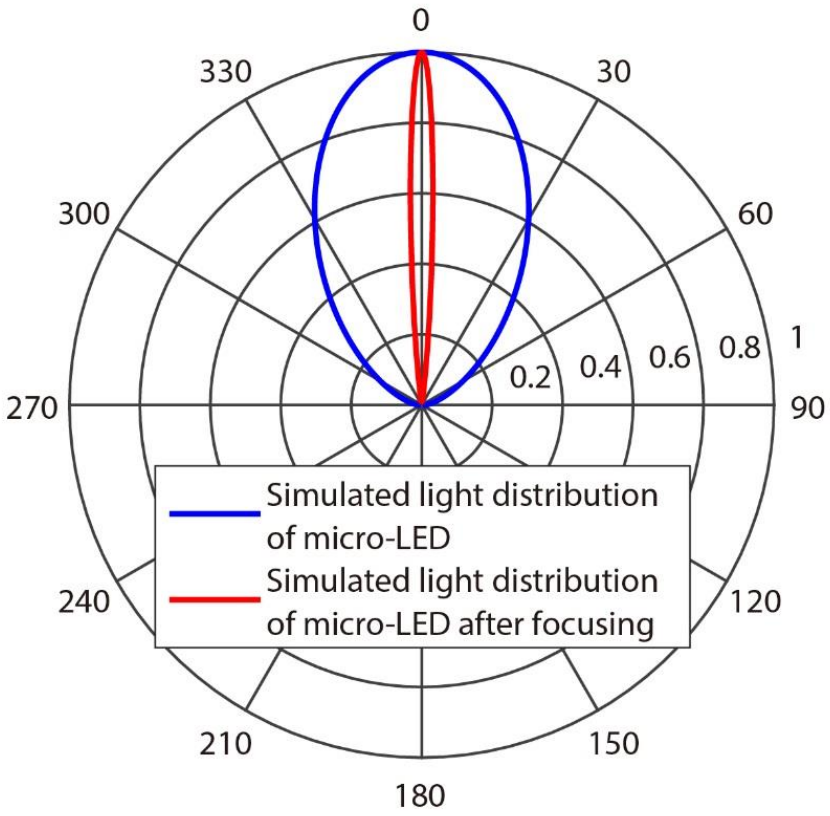

Figure 20. Simulated Light Distribution of Micro-LED and Its Distribution after Focusing versus the Angle of Irradiance

LOS geometry applied in micro-LED light distribution simulation and LOS channel gain simulation is shown in Figure 19. d is the free space distance from the GaN based micro-LED to the PIN receiver; φ is the angle of irradiance; ψ is the angle of incidence. To evaluate the farfield of a micro-LED manipulated by the focusing lens, a simple optics approximation is employed [36]. It is obvious that this approximation is only accurate when $\tan\phi \approx \phi$, which is clearly not always the case in our work. However, because the most of optical power is concentrated at small φ region, this approximation still provides useful information for this research. To estimate the farfield from a single micro-LED, a Gaussian-type distribution is utilized in Equation below, where R is the radiance; φ is the angle of irradiance; and φ0 is the fitting parameter assumed as 30° in this work. The farfield pattern is shown in Figure 20 (blue curve).

$$R(\phi) = exp(-\frac{\phi^2}{2\phi_0^2}) \quad [2]$$

By applying an ABCD matrix method in ray optics shown in Eq. 3, the farfield and energy distribution can be solved, where y0 and φ0 denote the initial position and the initial angle. In this simulation, y0 is 0 and φ0 is calculated by Eq. 2. The M matrix is determined by Eq. 4, whose value for each component can be found in Table 1. B1 is the distance between the micro-LED and the focus lens; C2 is the lens strength; and B3 is the distance between the micro-LED and the PIN receiver. The calculated farfield and power distribution is illustrated in Figure 20 (red curve).

$$\begin{bmatrix} y_1 \\ \phi_1 \end{bmatrix} = M_1 M_2 M_3 \begin{bmatrix} y_0 \\ \phi_0 \end{bmatrix} \quad [3]$$

$$M_i = \begin{bmatrix} A_i & B_i \\ C_i & D_i \end{bmatrix} \quad [4]$$

LOS channel gain is given by Eq. 5. [37–40]

$$H(0)_{LOS} = \begin{cases} \frac{(m+1)A}{2\pi d^2} cos^m(\phi) T_s(\psi) g(\psi) cos(\psi), & 0 \le \psi \le \Psi_c \\ 0, & \theta > \Psi_c \end{cases} \quad [5]$$

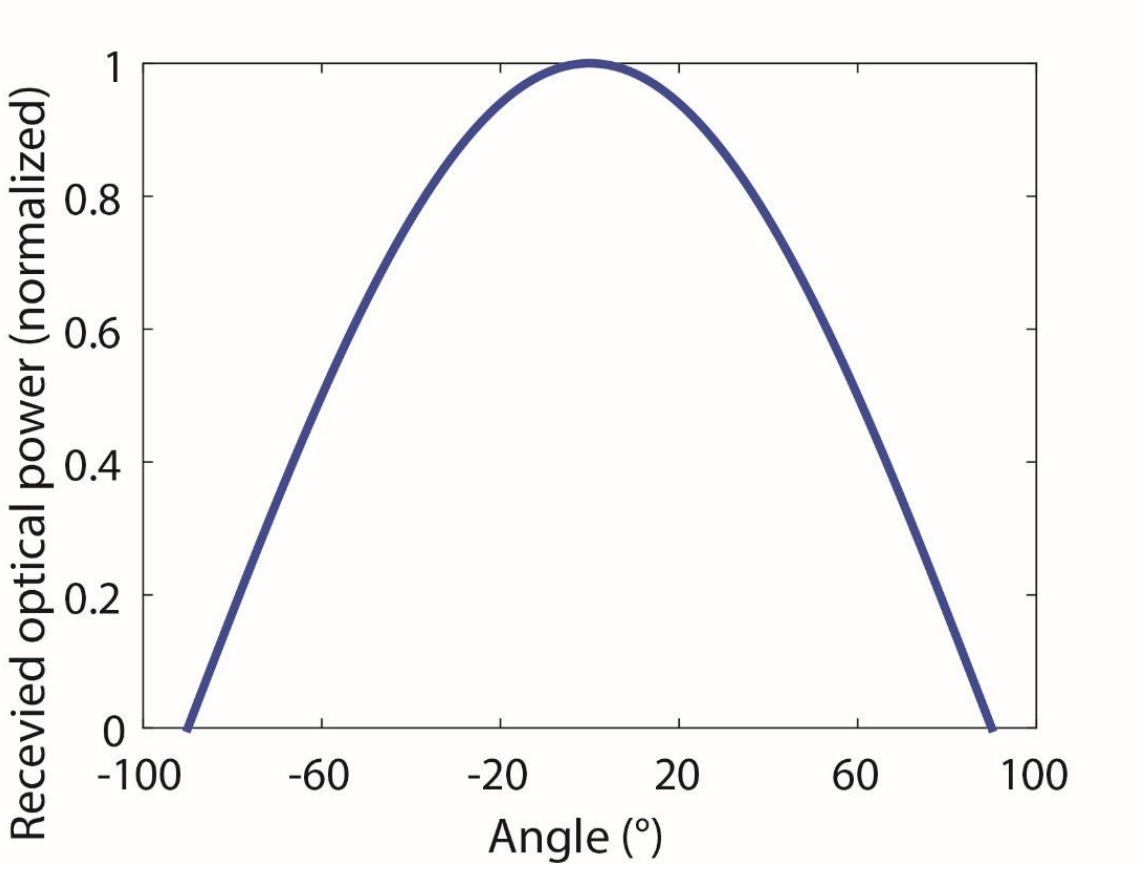

Figure 21. Simulated Normalized LOS Channel Gain versus the Angle of Incidence When the Angle of Irradiance Is Fixed

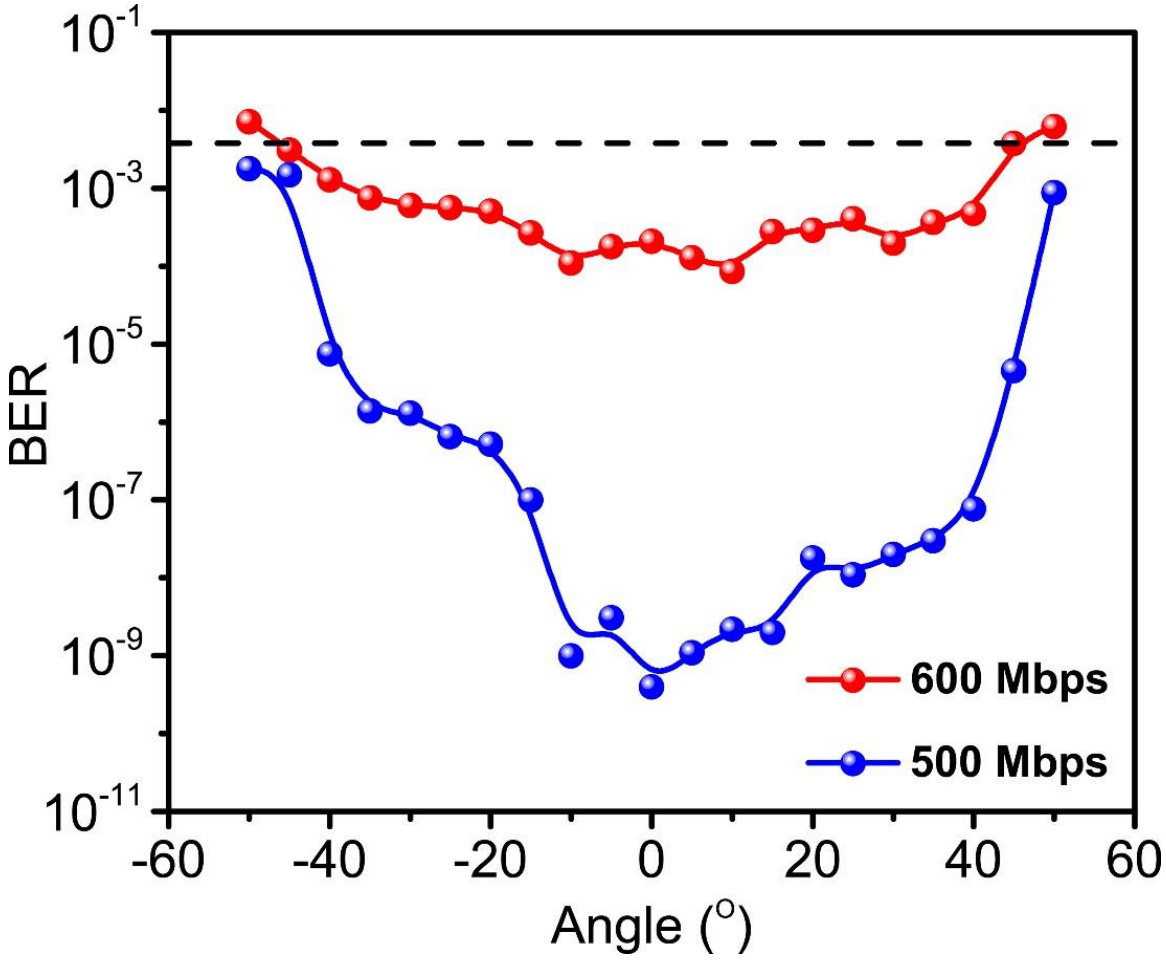

Figure 22. The BER for Different Angle of Incidence at Data Rates of 500 Mbps and 600 Mbps

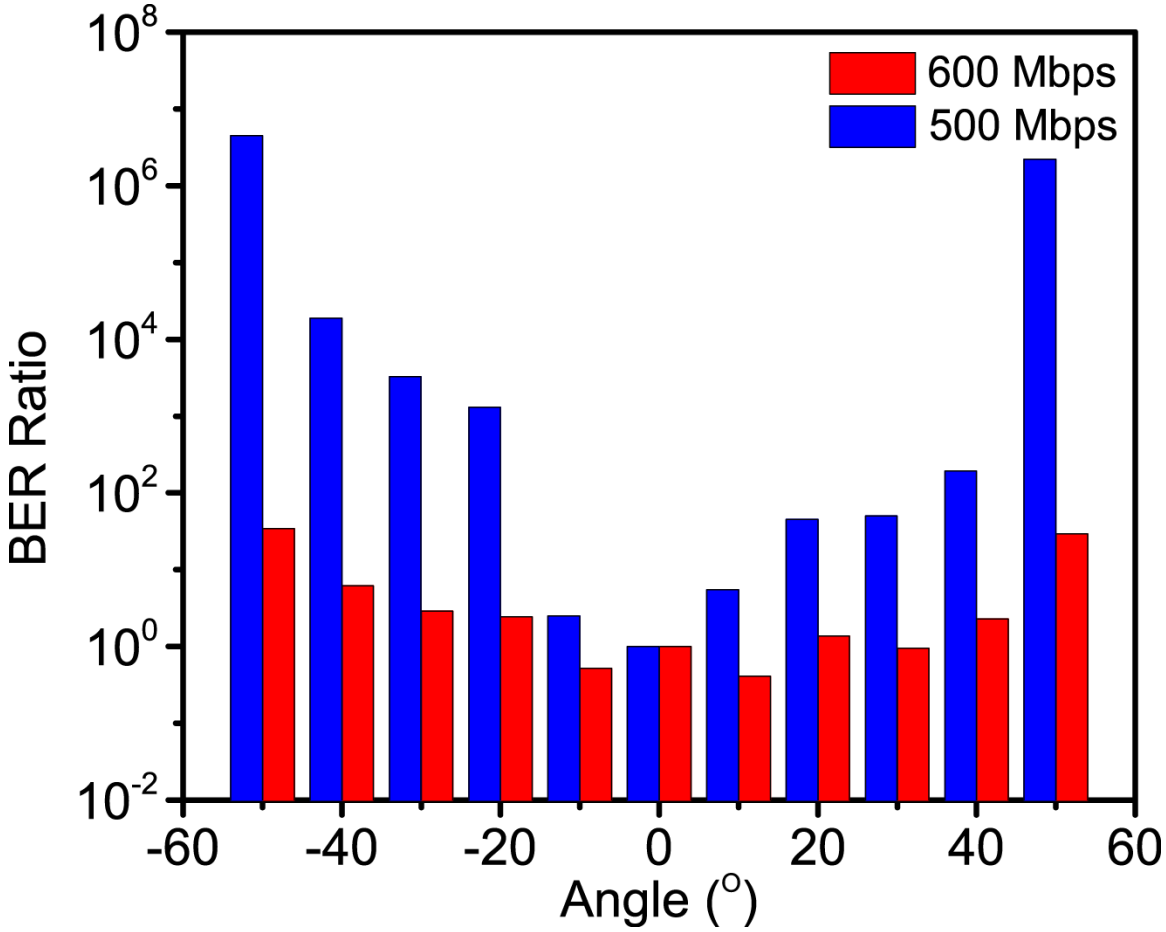

Figure 23. Active Tracking System Improved VLC Performance at Data Rates of 500 Mbps and 600 Mbps

Table 1. ABCD Matrix Value

i	Ai	Bi	Ci	Di
1	1	0.55 cm	0	1
2	1	0	-2 cm^{-1}	1
3	1	80 cm	0	1

Where m = − ln2/ln(cos(Φ1/2)) is the Lambertian order of the optical source relative to $\Phi_{1/2}$, the transmitter semi-angle (at half power). Original directed

transmitter $\Phi_{1/2}$ = 15° corresponds to m = 20. *A* denotes the detection area of the PIN receiver. We assume the receiver is pointed straight upward, and utilizes a concentrator of field of view (FOV) $\Phi_{1/2} = 15°$. It achieves omnidirectional gain $g(\psi) \approx g \approx n^2$ and an omnidirectional filter with $T_s(\psi) \approx T_s$. We did simulation based on those equations and got results of normalized LOS channel gain versus the angle of incidence ψ when the angle of irradiance φ is small as shown in Figure 21. If φ is very small, we can increase H(0) by narrowing the angle ψ. It enhances the SNR or BER of this VLC system.

Figure 22 demonstrates that the BER becomes worse when the incident light leaves from the point-to-point link. It shows that the angle of incidence changes the concentration of the received power, similar to the mechanism using neutral density filter as shown in Figure 20. Therefore, the active tracking system is necessary in VLC, especially for practical indoor or outdoor uses. The histogram as shown in Figure 23 reveals that the active tracking system enhances VLC performance if it is out of focus or far away from the point-to-point transmission. BER ratio represents the ratio of the BER after active tracking to the BER originally. When the angle is 0°, BER ratio is 1 for active tracking system does not function to change the pointing of the PIN receiver. Within a 10° range, BER does not enhance dramatically even if the active tracking system works because the ball lens of the PIN receiver can concentrate the received optical power. In the range between 10° and 50°, BER improves a lot by automatically narrowing the angle of incidence. When the angle of incidence is between 50° and 60° out of FOV, active tracking system can still sense the incident light and narrow the angle of incidence to provide a valid VLC link.

CHAPTER 3

NONE-LINE-OF-SIGHT VLC DEMONSTRATION

3.1 Introduction

Today's wireless network is in the midst of a transformation driven by the proliferation of data. Explosive growth in data-driven applications is placing unprecedented demands on communication systems. The performance of current Wi-Fi technology, however, is fundamentally limited due to the radio frequency (RF) spectrum crisis and is no longer sufficient to support future big data communication. Most recently, visible light communication (VLC) has emerged as a promising technology to mitigate the looming RF spectrum crisis as well as support a faster and safer wireless network for future communications. Thus, the essential techniques, including the fabrication of fast LEDs and optimization of the modulation scheme, have been widely investigated.

However, the limited bandwidth is the key factor of an LED-based optical source in VLC. Commercial LEDs based on blue LEDs and yellow phosphor usually have a modulation bandwidth of several MHz. Using a blue filter can increase the bandwidth to 20 MHz [41]. In comparison, micro-LEDs based on gallium nitride (GaN) offer much smaller carrier lifetimes and lower capacitance, which increases the bandwidth from several MHz [41] to hundreds of MHz [42]. On-off keying (OOK), pulse-amplitude modulation (PAM) and orthogonal frequency division multiplexing (OFDM) have been used to achieve high-speed data communication up to 5 Gbps for one micro-LED [42], demonstrating the significant advantages of micro-LEDs in the application of VLC.

Regarding the VLC standard, the IEEE 802.15.7 VLC task group has completed a PHY and MAC standard for VLC as of December 2011 with maximum data communication rate of 96 Mbps [43]. It fails to consider the latest technological

developments in the field of optical wireless communications, specifically with the wider bandwidth of GaN-based micro-LEDs and the introduction of optical orthogonal frequency-division multiplexing (O-OFDM) modulation methods which have been optimized for high data rates, multiple-access and energy efficiency. IEEE 802.11ac, widely used in 5G Wi-Fi communication, is a wireless networking standard based on OFDM modulation methods in the 802.11 families providing wider bandwidth (up to 80 MHz), high-density modulation (up to 256-QAM), and a single link high-throughput of up to 433 Mbps [44, 45]. Its 80 MHz channel bandwidth and 400 ns guard interval provides a data rate of 433 Mbps with a 256 QAM modulation scheme. Being able to use an IEEE 802.11ac-based communication system [46] provides a pathway towards merging Wi-Fi and VLC links, which can accelerate the practical application of VLC.

Line-of-sight (LOS) VLC using a GaN micro-LED achieves speeds on the order of Gbps in previous research [47, 48], but its indoor communication scenario is not realistic. Non-line-of-sight (NLOS) VLC is more realistic, but there is no experimental demonstration, especially for micro-LEDs, due to its small emission area and low optical output power. In this research, a packaged GaN-based micro-LED with a pixel size of 80μm × 80μm was employed with a frequency response up to 92.7 MHz. We improved optics at both transceiver and receiver and enlarged the free space transmit range to 3.6 m for LOS VLC. We analyzed NLOS of the proposed VLC system using a micro-LED based on four kinds of reflection material such as mirror, ceramic, print paper, and photo paper. It demonstrated a high-speed VLC link for multi-path free space transmission according to the modified IEEE 802.11ac standard achieving a data rate of up to 433 Mbps.

3.2 Experimental Setup

IEEE 802.11ac has been used in RF band for high-throughput Wi-Fi. Here, we introduced IEEE 802.11ac wireless networking standard to VLC and modified its carrier frequency to approximately 50 MHz, which fit the electrical-to-optical modulation bandwidth of the micro-LED as discussed above. Figure 24 demonstrates the proposed LOS VLC link using a single GaN micro-LED and practical IEEE 802.11ac wireless communication standard. We reproduced the IEEE 802.11ac-based VLC link by SystemVue, which includes an IEEE 802.11ac source, IEEE 802.11ac vector signal analysis (VSA) and bit error rate (BER) measurement. The IEEE 802.11ac data source generated a PN15 data pattern. The IEEE 802.11ac source module generated IEEE 802.11ac-coded baseband signal with modulation coding scheme up to 256 QAM and a supported bandwidth of 80 MHz. The Complex to Real and Imaginary Converter model converted complex input values to real and imaginary output values. The oscillator generated an RF (complex envelope) tone. Then M-ary quadrature amplitude modulation (M-QAM) baseband signal was modulated with the carrier frequency implemented by the modulator model, which was then downloaded to an ESG vector signal generator, Agilent E4438C. A DC bias, GS610, was added to the AC input signal by a Bias-T, Mini-Circuits ZFBT-6GW, driving the single GaN-based micro-LED. The light beam was concentrated by both transceiver and receiver optics in the 65 cm transmit distance and then captured by a high-sensitivity avalanche photodiode (APD), Hamamatsu C12702. The electrical output signal of the APD was detected by a PXA signal analyzer, Agilent N9030A. This IEEE 802.11ac receiver model was used to detect, demodulate and decode the baseband signal. In the IEEE 802.11ac VSA, it was captured by a Keysight 89600 vector signal analyzer. The Spectrum Analyzer model was used to measure the spectrum of a real baseband. A coherent demodulator can be used to perform amplitude, phase, frequency, or I/Q demodulation. The Real and Imaginary to Complex Converter

model converts real and imaginary input values to complex output values. After equalization, the output signal is ready for constellation of each spatial stream. In an IEEE 802.11ac BER, the Delay model introduces a delay of N samples to the input signal, in this case a PN15 data pattern, to generate the reference. After the bit streams synchronization, the reference (REF) and test (TEST) inputs are compared for BER measurement.

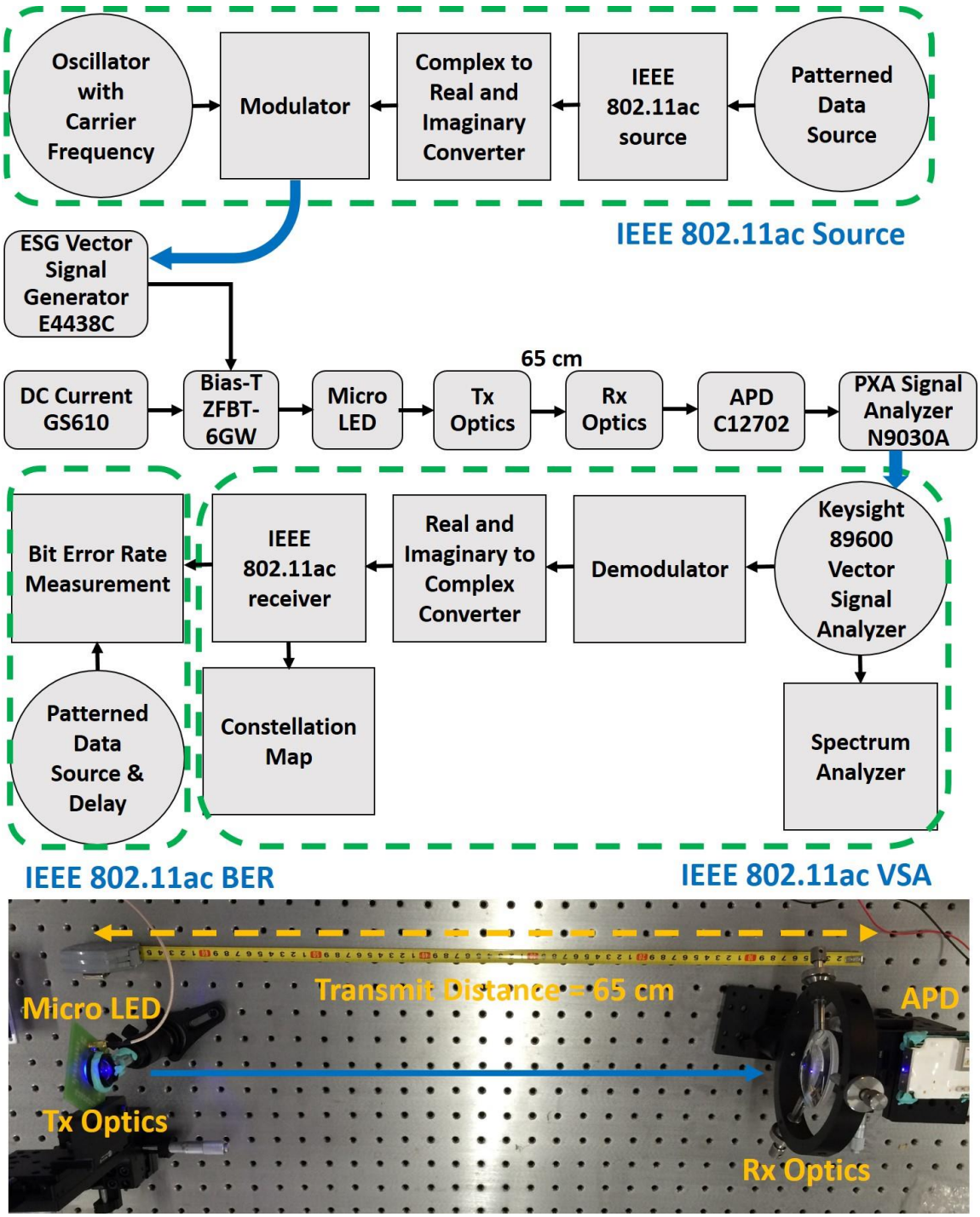

Figure 24. LOS VLC Using a GaN-based Micro-LED and Modified IEEE 802.11ac Standard Implementation by SystemVue Including IEEE 802.11ac Source, IEEE 802.11ac VSA, and IEEE 802.11ac BER

In practical applications, the NLOS VLC link relies on the reflected light from the walls. For this scenario, we studied two commercially available reflection materials for directed NLOS: mirror and ceramic. As a reference, a mirror-based NLOS VLC setup with several reflections was established as shown in Figure 25. The blue light is emitted from a GaN-based micro-LED and concentrated by a focus lens. Both the incident angle and reflected angle are 45° due to directed reflection. After a few reflections, the directed NLOS optical power is concentrated by the focus lens and captured by an APD. The system performance is evaluated by the overall distance, the received power, the transmitted data rate with modulation mode, and BER.

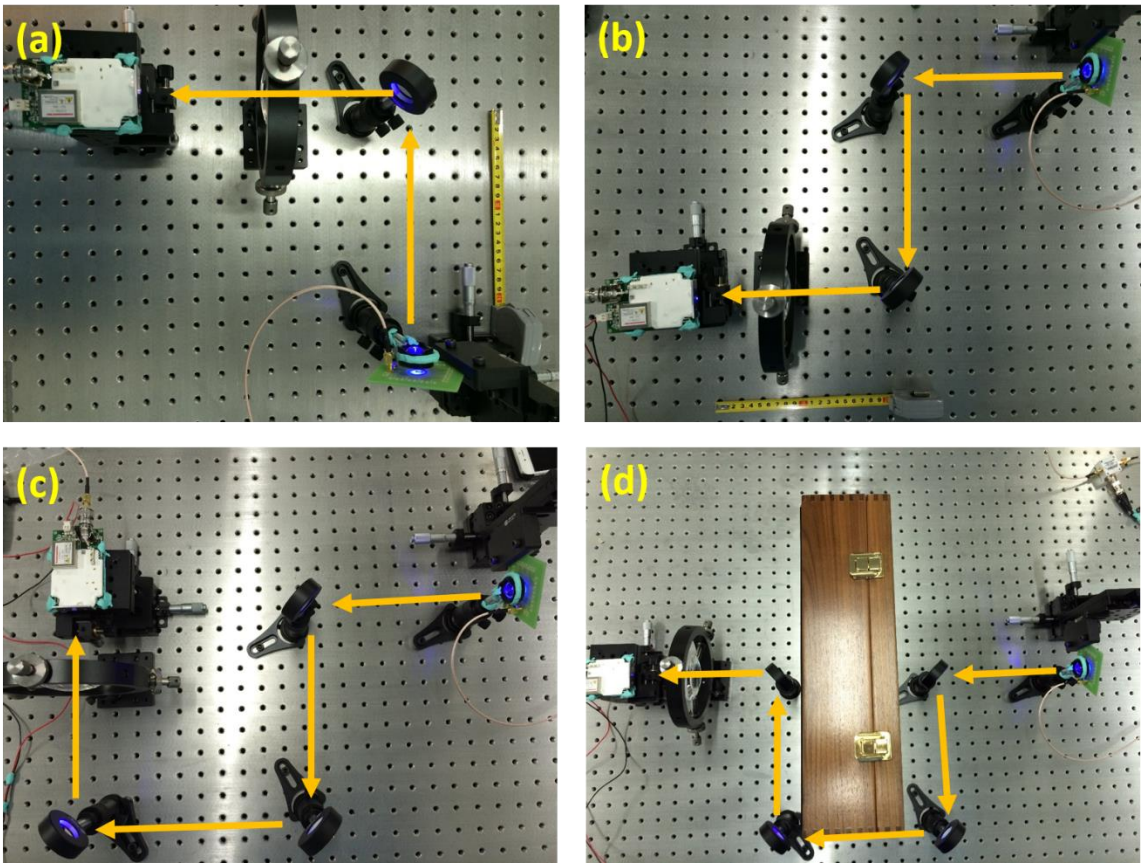

Figure 25. Mirror-based Directed NLOS VLC Setup with One Reflection; (b) Mirror-based Directed NLOS VLC Setup with Two Reflections; (c) Mirror-based Directed NLOS VLC Setup with Three Reflections; (d) Mirror-based Directed NLOS VLC Setup with Four Reflections

With a non-directed NLOS link, the divergent beam of the communications between a transceiver and a large field-of-view (FOV) of the receiver depend on light reflections on the wall surfaces in the room. Two commercially available materials were used: print paper and photo paper. In comparison to the directed NLOS VLC setup, we added two optical lenses at the receiver in the non-directed NLOS VLC system as shown in Figure 26 (a) with careful alignment in order to focus the transmission beam and narrow receiver FOV, which can support a feasible VLC link. In Figure 26 (b), (c), and (d), we fixed the 45° incident angle, the 40 cm free-space transmit distance, and changed the reflected angle to 10°, 45°, and 70°. The overall performance is measured by the reflected angle, the received power, the transmitted data rate with modulation mode, and BER.

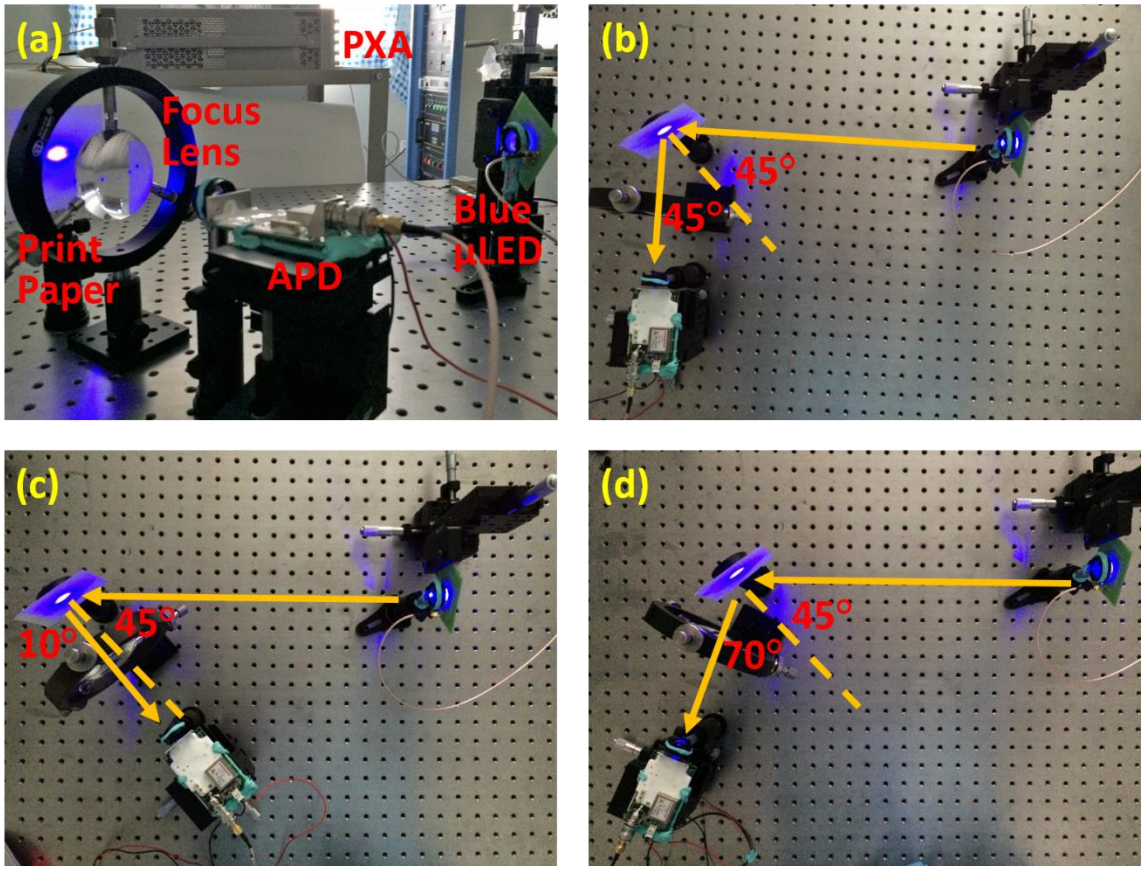

Figure 26. (a) Print Paper Based Non-directed NLOS VLC System; (b) Print Paper Diffuse Reflection for 45° Incident Angle and 45° Reflected Angle; (c) Print Paper Diffuse Reflection for 45° Incident Angle and 10° Reflected Angle; (d) Print Paper Diffuse Reflection for 45° Incident Angle and 70° Reflected Angle

3.3 GaN-based Micro-LED Bandwidth

Figure 27 shows that the electrical-to-optical modulation bandwidth of the micro-LED is 92.7 MHz at the 40 mA DC bias. Note that the micro-LED has a much higher bandwidth than 92.7MHz, but packaging the micro-LEDs on a PCB limited the achieved bandwidth. However, the 92.7 MHz bandwidth is large enough for the 80 MHz IEEE 802.11ac standard. Improved packaging techniques, such as impedance matching, will be done in our future work. Figure 28 shows the -3dB electrical-to-

optical modulation bandwidth of the GaN-based micro-LED with DC bias from 10 mA to 100 mA. In this range, higher currents lead to the bandwidth increasing from 57.8 MHz to 107.6 MHz. Then the tendency keeps steady for the bandwidth saturation.

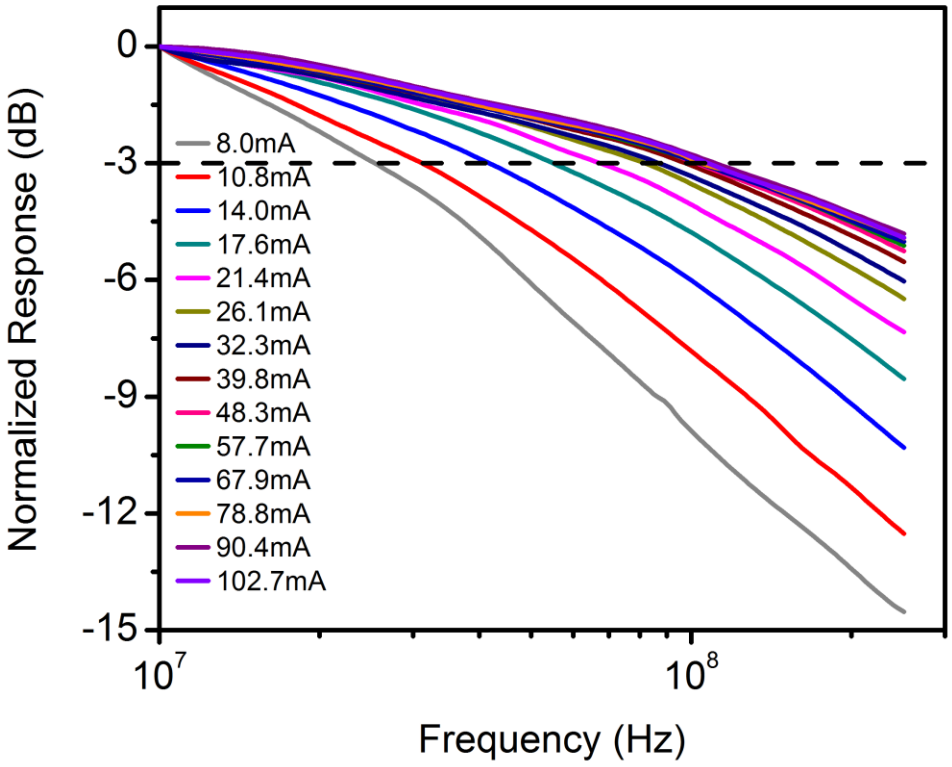

Figure 27. The Frequency Response of the Packaged Micro-LED under 40 mA DC Bias. The Extracted Modulation Bandwidth Is 92.7 MHz

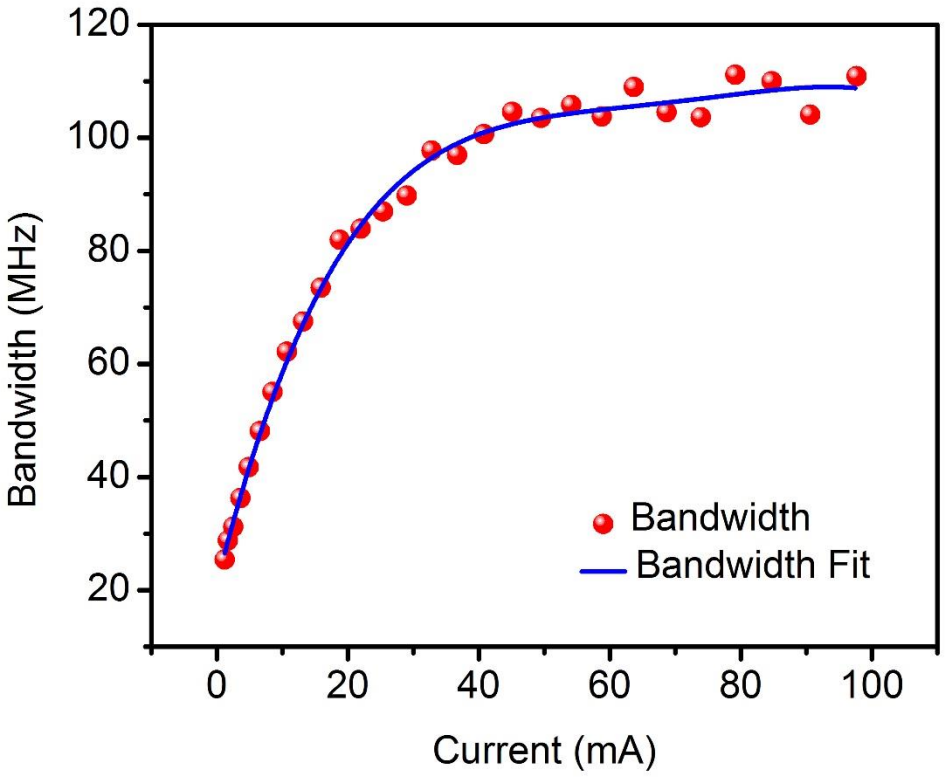

Figure 28. The -3dB Electrical-to-optical Modulation Bandwidth versus DC Bias

3.4 Optimal Operating Point

The VLC link has been built by a single GaN-based micro-LED and modified IEEE 802.11ac standard, in which DC bias dominates the bandwidth of the micro-LED and the AC carrier frequency determines the band used in the modified IEEE 802.11ac standard. In the micro-LED bandwidth experiment, it shows that the bandwidth increases dramatically when DC bias goes up to 40 mA. If DC bias continually increases, the bandwidth will increase slightly because it is saturated by both PCB impedance matching and the micro-LED itself. Considering the reliability of the micro-LED, we chose 40 mA for the optimal operating conditions because larger DC biases might reduce the lifetime of the micro-LED. Also, AC carrier frequency is

the key factor to the VLC link band when using a modified IEEE 802.11ac standard. As 80 MHz channels were employed in VLC, a low AC carrier frequency moved the used band close to DC. Therefore, the quality of VLC became worse, because DC noise was brought into VLC. On the contrary, when a high AC carrier frequency was used, the band moved beyond the -3dB bandwidth (92.7 MHz) of the packaged micro-LED when the DC bias was at 40 mA. Figure 29 demonstrates the relationship between DC bias and BER of the VLC link. Figure 30 demonstrates the relationship between AC carrier frequency and BER of the VLC link using a practical IEEE 802.11ac with 256 QAM modulation scheme. The VLC link with 50 MHz carrier frequency and 40 mA DC bias offers a BER of 6.2×10^{-5}. These characteristics proved that the optimal operating current is 40 mA and AC carrier frequency is 50 MHz.

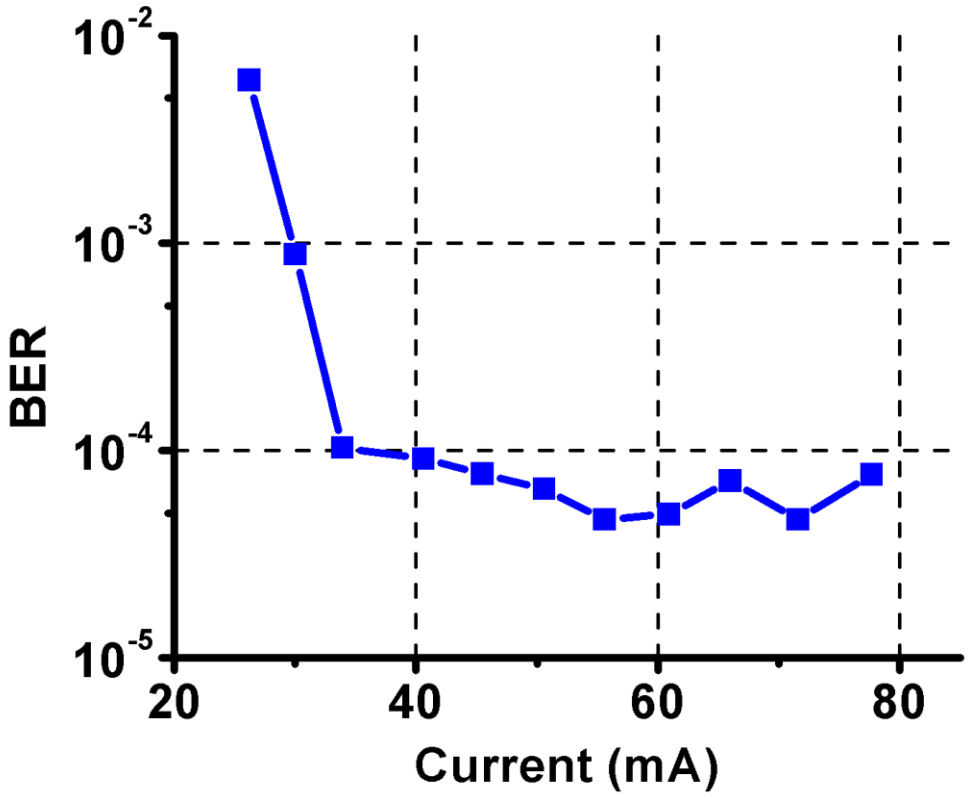

Figure 29. BER versus DC Bias in VLC for 50 MHz AC Carrier Frequency and 256 QAM Scheme

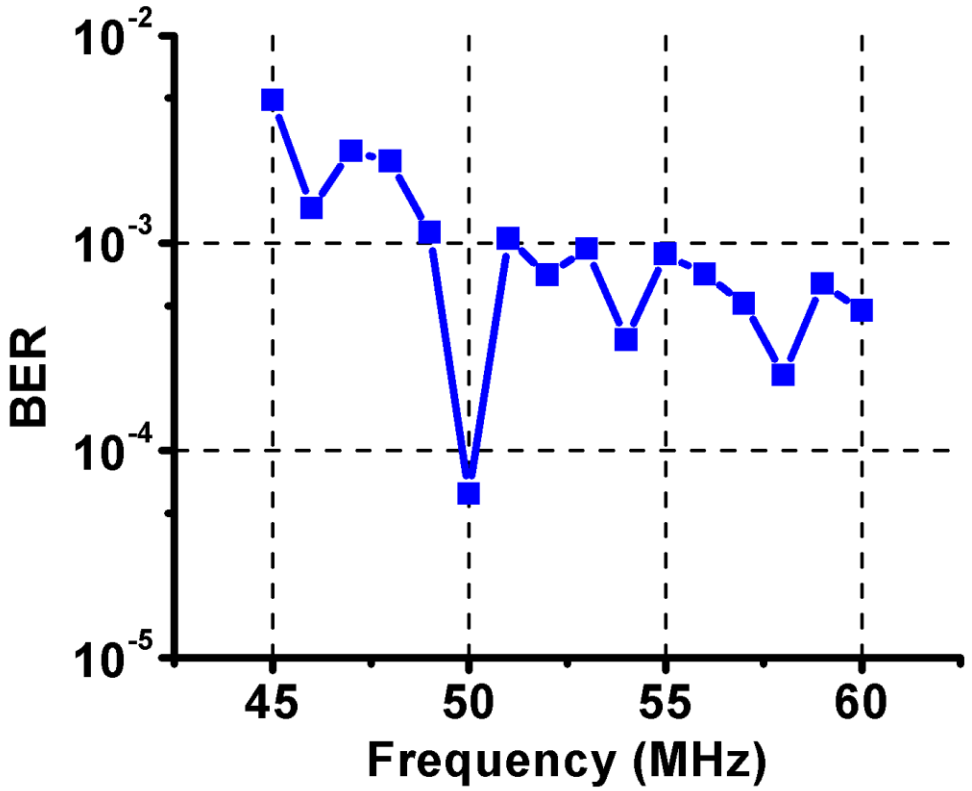

Figure 30. BER versus AC Carrier Frequency in VLC at 40 mA DC Bias with 256 QAM Scheme

3.5 LOS VLC

The LOS VLC using a GaN-based micro-LED and modified IEEE 802.11ac standard was established as shown in Figure 24. According to this modified standard, the LOS VLC link at optimal operating condition using 80 MHz channels and 400 ns guard interval achieves a data rate of 433.3 Mbps and a BER of 4.6×10^{-5} with a 256 QAM modulation scheme. Figure 31 shows received power spectrum over a frequency range from 10 MHz to 90 MHz. The received power spectrum decreased by

6 dB approximately due to the -3dB bandwidth of the packaged micro-LED. Figure 32 illustrates the received constellation maps for four modulation schemes including QPSK, 16 QAM, 64 QAM, and 256 QAM.

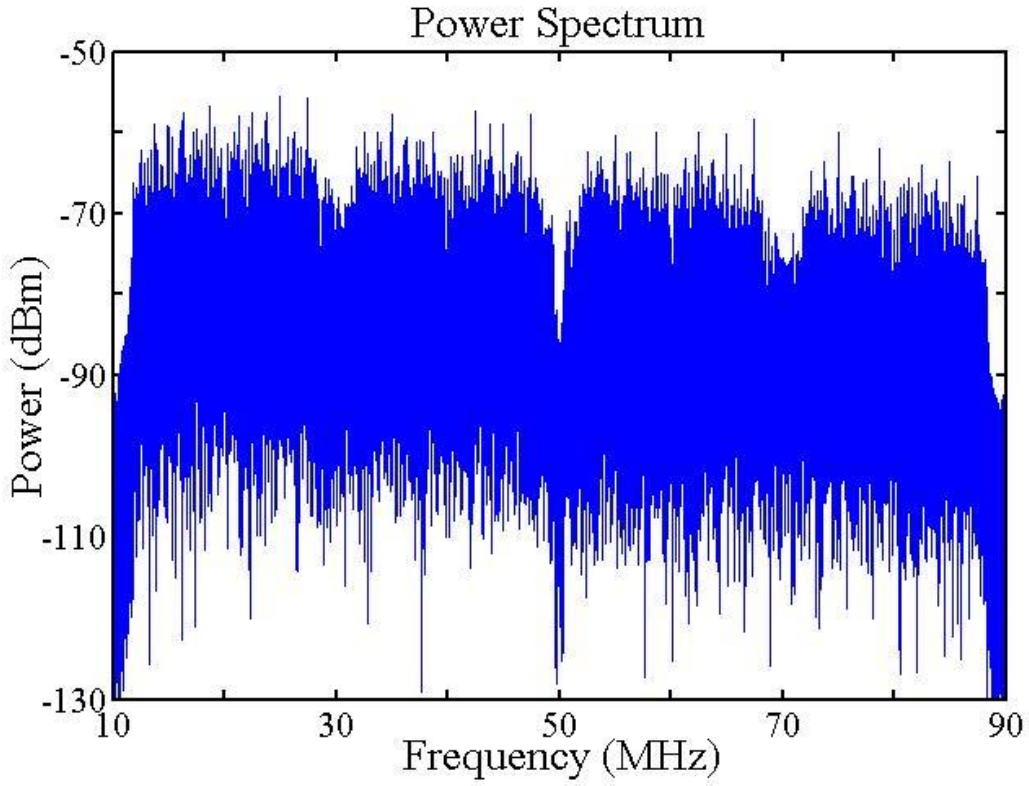

Figure 31. BER versus AC Carrier Frequency in VLC at 40 mA DC Bias with 256 QAM Scheme

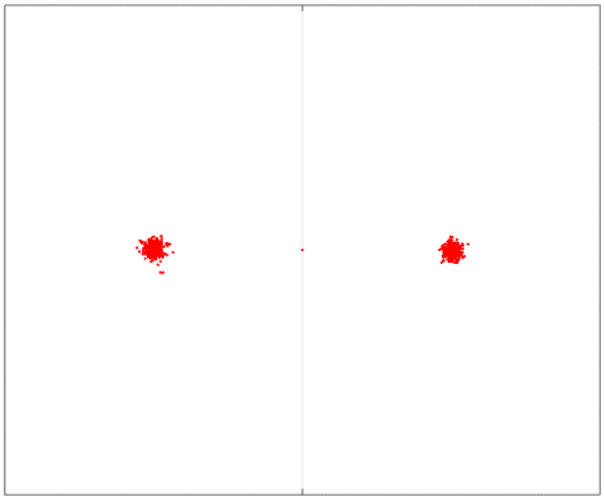

(a) BPSK ½ Coding Rate

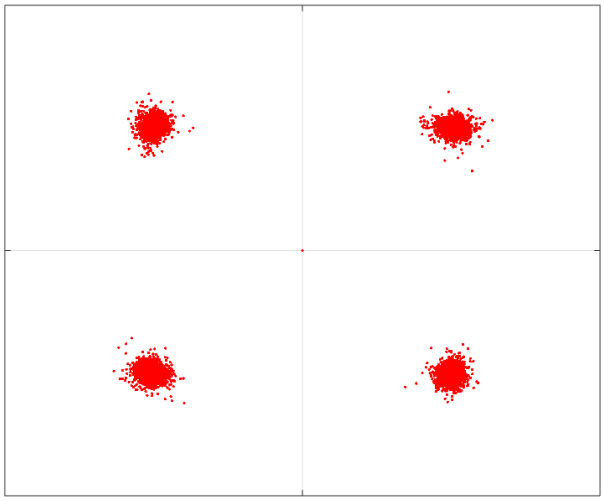

(b) QPSK ½ Coding Rate

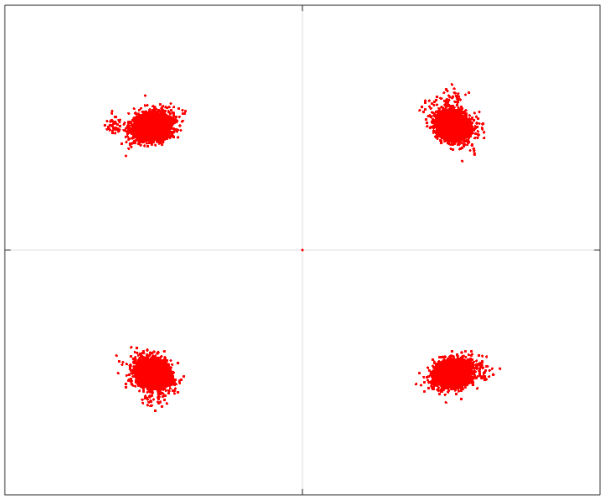

(c) QPSK ¾ Coding Rate

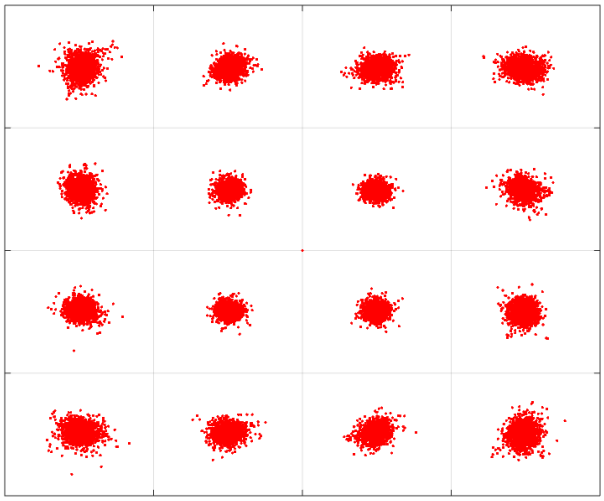

(d) 16 QAM ½ Coding Rate

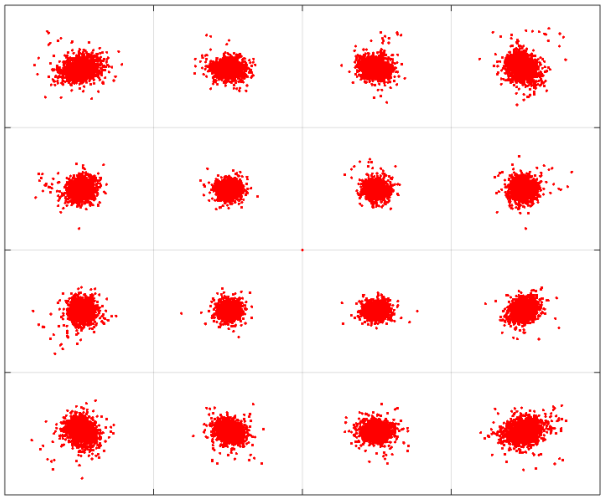

(e) 16 QAM ¾ Coding Rate

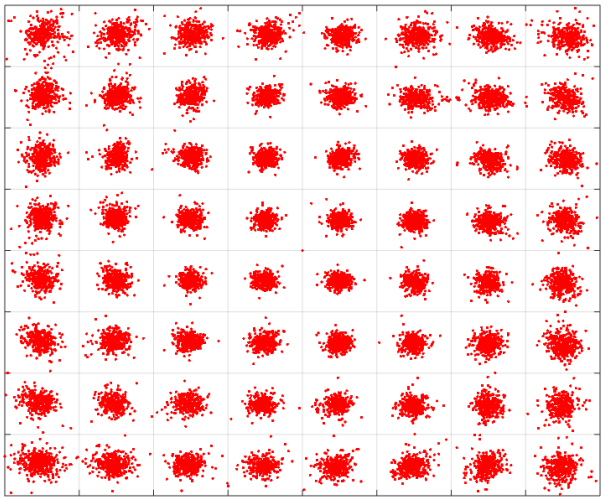

(f) 64 QAM 2/3 Coding Rate

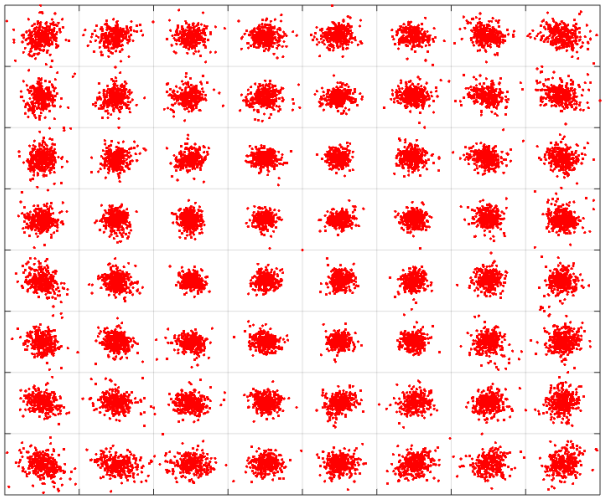

(g) 64 QAM ¾ Coding Rate

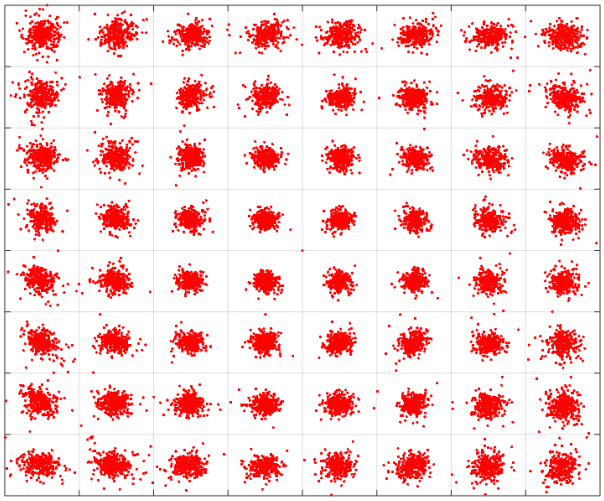

(h) 64 QAM 5/6 Coding Rate

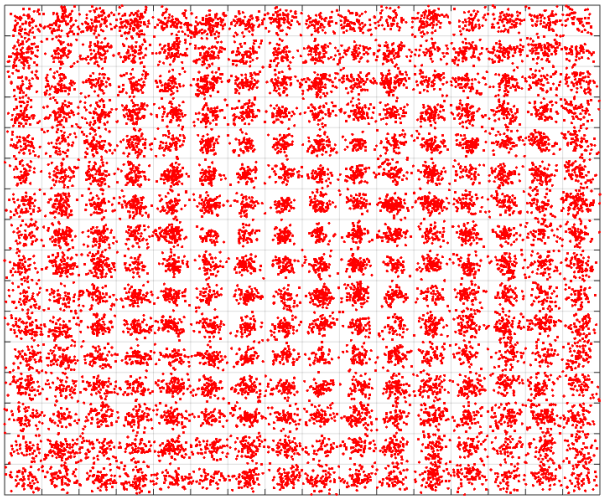

(i) 256 QAM ¾ Coding Rate

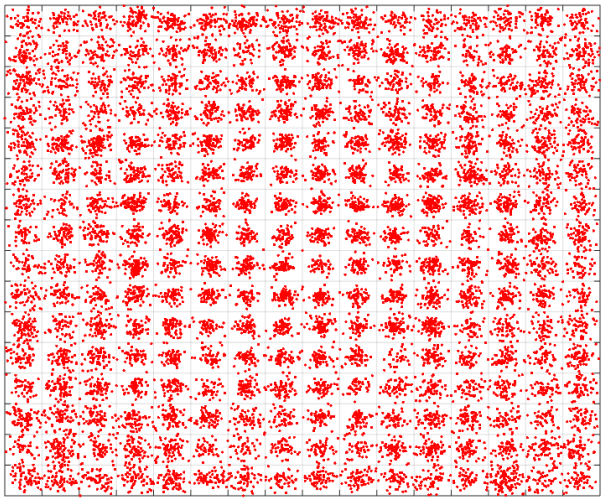

(j) 256 QAM 5/6 Coding Rate

Figure 32. Received Constellation Maps of QPSK, 16 QAM, 64 QAM, and 256 QAM

We also investigated the distance loss of LOS VLC within different distances over a range from 0.2 m to 3.6 m by measuring the received power and BER as shown in Figure 33. The 3.6 m distance was limited by the size of our lab, and longer distance communication will be done in the future. It shows that received power decreased from 1.22 mW to 0.91 mW and thus BER kept a stable value of approximately 5×10^{-5} when the transmit distance increased. The distance loss largely depended on the proposed optics at both the transmitter and the receiver.

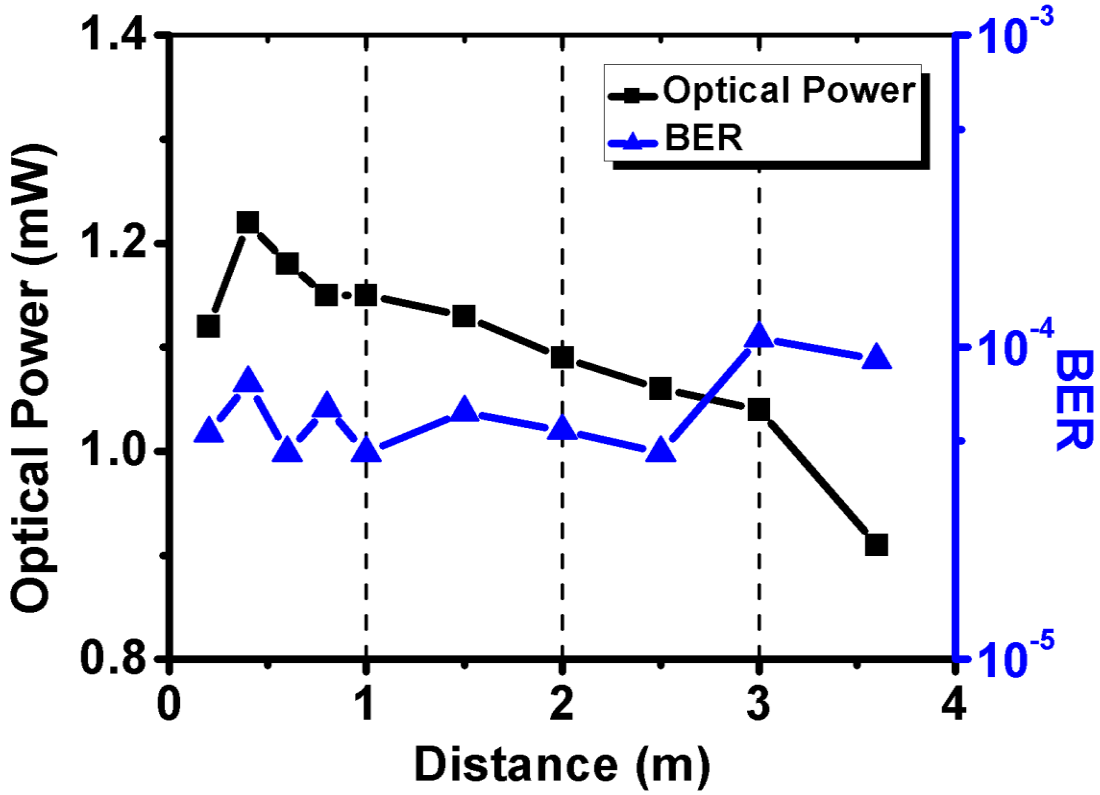

Figure 33. Optical Power and BER versus Distance in LOS VLC Using Modified IEEE 802.11ac at 40 mA DC Bias with 50 MHz AC Carrier Frequency

3.6 Directed NLOS VLC

Previous studies on VLC only assumed LOS between the transmitter and the receiver [47, 48]. Thus the transmission loss of indoor VLC is mainly related to the transmit distance, which determines the received optical power by LOS. In practice, the LOS light is usually blocked by obstacles between the transmitter and the receiver. Therefore, NLOS VLC link based on reflections can be utilized to keep communication functional [52, 53]. There are two kinds of transmission loss in NLOS VLC link: distance loss and reflection loss. The distance loss of LOS VLC link has already been discussed above. The mirror-based reflectivity is 0.91 while the ceramic-based reflectivity is 0.07 according to the incident optical power and reflected optical power. These results illustrate that the reflection loss is the principal loss in NLOS VLC.

Table 2 shows the system performance of directed NLOS VLC measured by the overall distance, the received power, transmitted data rate with modulation mode, and BER. The mirror-based NLOS VLC can still offer an effective high-speed communication link at a data rate of 433.3 Mbps and a BER of 10^{-5}. Ceramic, as the traditional wall material, was also employed in directed NLOS VLC. The result in Table 1 illustrates that after two ceramic-based directed reflections, the received optical power decreased dramatically to -22.22 dBm when background noise exerted a large impact to SNR. Even if the SNR of the ceramic-based NLOS VLC cannot support the high-speed link with 256 QAM, the practical IEEE 802.11ac standard with QPSK modulation scheme can be applied to this link at a data rate of 97.5 Mbps and a BER of 9.3×10^{-5}. We can also conclude from this that the proposed VLC link is suitable for visible light communication with very weak light due to the combination of the high-sensitivity APD, noise resistive modulation scheme, large bandwidth of micro-LED, and proposed optics.

Table 2. Directed NLOS VLC Using Practical IEEE 802.11ac for 40 mA DC Bias and 50 MHz AC Carrier Frequency

Direct Reflection Type	Overall Distance (cm)	Received Power (dBm)	Applied Modulation Mode	Data Rate (Mbps)	BER
mirror reflection once	40	-0.27	256 QAM	433.3	1.27×10^{-4}
mirror reflection twice	60	-0.71	256 QAM	433.3	6.54×10^{-5}
mirror reflection three times	80	-3.47	256 QAM	433.3	5.54×10^{-5}
mirror reflection four times	100	-5.69	256 QAM	433.3	2.01×10^{-4}
ceramic reflection once	40	-12.22	64 QAM	325	5.15×10^{-5}
ceramic reflection twice	60	-22.22	QPSK	97.5	9.32×10^{-5}

3.7 Non-directed NLOS VLC

Besides directed NLOS VLC, non-directed NLOS VLC was firstly demonstrated experimentally in our work and may require higher transmission power. In the modeling literature [54, 55], it has been found that the intensity via diffuse paths is much weaker than that via LOS paths. The power via an LOS path is about ten times higher than that via the first reflective path. In the non-directed NLOS VLC experiment in our work, the intensity via an LOS path is 37.3 times greater than that

via the first print paper reflective path and 32 times higher than that via the first photo paper reflective path.

Table 3 shows the overall performance of non-directed NLOS VLC evaluated by the reflected angle, received power, transmitted data rate with modulation mode, and BER. Diffuse reflection of non-directed NLOS VLC was uniformly distributed in different reflection angles when using print paper. With a 45° incident angle light, non-directed NLOS VLC can provide an effective communication link at a data rate of 195 Mbps and a BER of 6.36×10^{-5} at different reflection angles. On the other hand, the photo paper-based demonstration shows a non-uniform distribution in diffuse reflection. With a 45° incident angle light, it can provide communication links with different modulation modes at different reflected angles. The photo paper shows the performance of both directed reflection and diffuse reflection due to its surface roughness between the mirror and the print paper. When the reflected angle is 45°, using mirror-based reflection, it is possible to achieve 325 Mbps with 64 QAM modulation and a BER of 5.15×10^{-5}. When the angle is changed to 75°, the same BER can be achieved at a lower speed of 195 Mbps. However, when the reflected angle changes to 15°, keeping the 325 Mbps speed makes the quality of non-directed NLOS VLC decrease to a BER of 2.79×10^{-3}.

In solar blind ultraviolet NLOS communication [51, 56-59], bit rates of 2.4 kbps in 11 m or 200 bps in 100 m have been achieved by utilizing an LED array of 40 mW with a wavelength 274 nm as the light source. Compared with previous work, NLOS VLC shows its advantages including large-scale communication capacity, illumination spectrum, and 5G Wi-Fi standard compatibility for indoor communication.

Table 3. Non-directed NLOS VLC Using Practical IEEE 802.11 ac for 40 mA DC Bias and 50 MHz AC Carrier Frequency (Reflection Materials Are Print Paper and Photo Paper)

Diffuse Reflection Type	**Incident Angle (degree)**	**Reflected Angle (degree)**	**Applied Modulation Mode**	**Data Rate (Mbps)**	**BER**
print paper reflection	45	10	16 QAM	195	6.36×10^{-5}
print paper reflection	45	45	16 QAM	195	6.36×10^{-5}
print paper reflection	45	70	16 QAM	195	6.54×10^{-5}
photo paper reflection	45	15	64 QAM	325	2.79×10^{-3}
photo paper reflection	45	45	64 QAM	325	5.15×10^{-5}
photo paper reflection	45	75	16 QAM	195	6.36×10^{-5}

CHAPTER 4

WI-FI OVER VLC TECHNOLOGY

4.1 Introduction

The RF based wireless communication has been developed to the fifth generation, which meets the unprecedented communication demands and brings more benefits to human life nowadays. The Cisco white paper on visual networking index shows that the global mobile traffic data has reached 7 Exabytes per month in 2016, and is expected to be 49 Exabytes per month in 2021 [60]. However, the current RF technology is fundamentally limited to radio spectrum. As an emerging wireless technology, VLC utilizes the unregulated and wider optical spectrum. Thus, it becomes one of the alternative wireless technologies to RF communication. Furthermore, VLC can be integrated to the conventional illumination, which evolves each of light bulb to a high speed hotpot. Modern VLC system using GaN based micro-LED and orthogonal frequency division multiplexing (OFDM) has achieved high-throughput communication up to 11.95 Gbps for one micro-LED, which shows the significant advantages of micro-LEDs in the application of VLC. Because micro-LEDs have smaller carrier lifetime and lower junction capacitance. It elevates the electrical to optical modulation bandwidth from dozens of MHz to hundreds of MHz.

In regards to radio-over-fiber (RoF), it allows the delivering of radio services through distributed antenna systems built on top of fiber network infrastructures [61-64]. Similar to RoF, Wi-Fi over VLC system is another wireless technology, which allows the latest Wi-Fi standard services through VLC systems. Therefore, Wi-Fi services by VLC systems can easily deliver in extreme environments, especially in hospitals where electro-magnetic impact is regarded as an interference to high sensitive medical care facilities. In this paper, we investigate the coexistence of Wi-Fi and VLC systems, and demonstrate a VLC link using GaN based micro-LED and IEEE

802.11ac Wi-Fi service. Data transmission over VLC system can achieve a data rate of 433 Mbps and a bit error rate (BER) of 10^{-5} in 256 QAM modulation without pre-equalization. Error vector magnitude (EVM) and Eb/N0 are also provided to evaluate the communication performance in terms of signal quality.

4.2 Wi-Fi over VLC System Performance

According to this modified standard, the LOS VLC link at optimal operating condition using 80 MHz channels and 400 ns guard interval achieves a data rate of 433.3 Mbps and a BER of 4.6×10^{-5} with a 256 QAM modulation scheme. Fig. 9 shows received power spectrum over a frequency range from 10 MHz to 90 MHz. The received power spectrum decreased by 6 dB approximately due to the -3dB bandwidth of the packaged micro-LED.

IEEE 802.11ac not only supports the modulation modes used up to now (BPSK, QPSK, 16QAM and 64QAM) but also 256QAM. The wireless device determines, on the basis of the measured signal quality, which modulation mode is used. If the signal quality improves or degrades during a connection, the system will select a higher-order or lower-order modulation. To allow 256QAM transmission at a 5/6 code rate, IEEE permits an error vector magnitude (EVM) of at most -32 dB (2.5 %). For 64QAM, up to -27 dB (4.4 %) is tolerated. Fig. 10 illustrates the received constellation maps for four modulation schemes including BPSK, QPSK, 16 QAM, 64 QAM, and 256 QAM. The EVM for all of the modulations are lower than -27 dB. According IEEE 802.11ac standards, all the modulations except 256 QAM meet the EVM requirements below -27 dB. The results show that the Wi-Fi over VLC system can easily achieve 64 QAM modulation of IEEE 802.11 ac without equalization.

Table 4. IEEE 802.11ac EVM and BER Test Table

No.	Modulation	Rate (Mbps)	BER	EVM(dB)	EVM limit
9	256 QAM 5/6	433.3	6.77E-05	-27.196	-32
8	256 QAM 3/4	390	4.90E-05	-26.737	-30
7	64 QAM 5/6	325	5.15E-05	-27.094	-27
6	64 QAM 3/4	292.5	5.38E-05	-25.94	-25
5	64 QAM 2/3	260	5.63E-05	-26.095	-22
4	16 QAM 3/4	195	6.36E-05	-26.094	-19
3	16 QAM 1/2	130	7.82E-05	-26.235	-16
2	QPSK 3/4	97.5	9.32E-05	-25.937	-13
1	QPSK 1/2	65	1.22E-04	-25.923	-10
0	BPSK 1/2	32.5	2.14E-04	-26.589	-5

To evaluate the performance of the WiFi-over-VLC system for a real scenario, we measured the quality of the received signal in terms of error vector magnitude (EVM) at different levels of luminance, varying the VLC distance Tx-Rx from 0.8 to 3.6 m (illuminance ranging between 1300 uW and 117 uW). We illustrate the performance of the hybrid system in Fig. 2a. Here we report the constellation diagrams of the received signals at distances of 0.8 and at 3.6 m. Clearly, at longer distance (lower luminance) we observed a deterioration of signal quality. In Figure 34, we summaries the system performance in terms of EVM values for configurations against illumination. The data were measured from the VSA by moving the VLC RX away from the TX with distance. We see from the reported EVM values that the

performance was degraded at 117 uW (3.6 m distance); at any distance, we typically measured a slightly better EVM value (around 1.5 dB difference). This is ascribed to the fact that in the downlink case, the signal obtained by the receiver, although having an excellent EVM, had a limited electrical power: after the down conversion and the amplification, it experienced a significant SNR reduction, thus resulting in a sub-optimal LED driving signal. To separate the impairments in the VLC and in the RoF channels, we also report the performance trend obtained by transmitting the same signal only over the VLC part of the link. However, in all cases and at all luminance levels, the EVM value was always much lower than -27 dB, which is the limit given in the IEEE 802.11ac standard for the 325 Mbit/s transmission. In particular, we observed a working system at a luminance value even lower than 15 uW (i.e. at 3 m distance), which is a common distance from the ceiling in indoor communications.

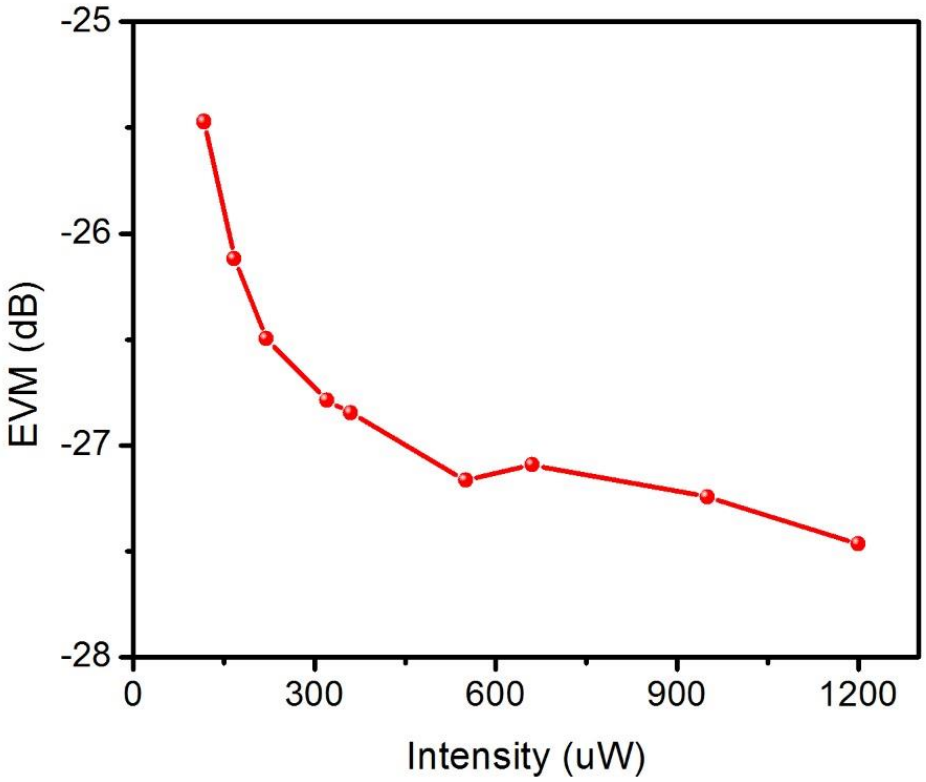

Figure 34. Wi-Fi over VLC System with Distance

4.3. Wi-Fi over VLC Link with Post Equalization

The system magnitude and phase response are shown in Figure 35 and Figure 36. As post equalization, Finite Impulse Response (FIR) Filter is used in Wi-Fi over VLC link to enhance the communication performance. The custom design FIR response is shown in Figure 37 in order to cancel the magnitude decline and phase shift. The number of taps in FIR is 112.

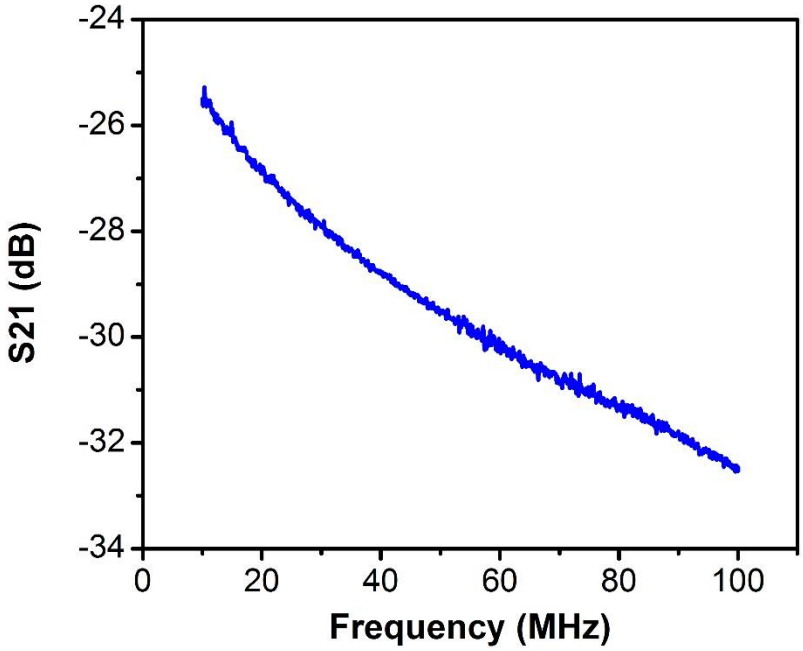

Figure 35. System Magnitude

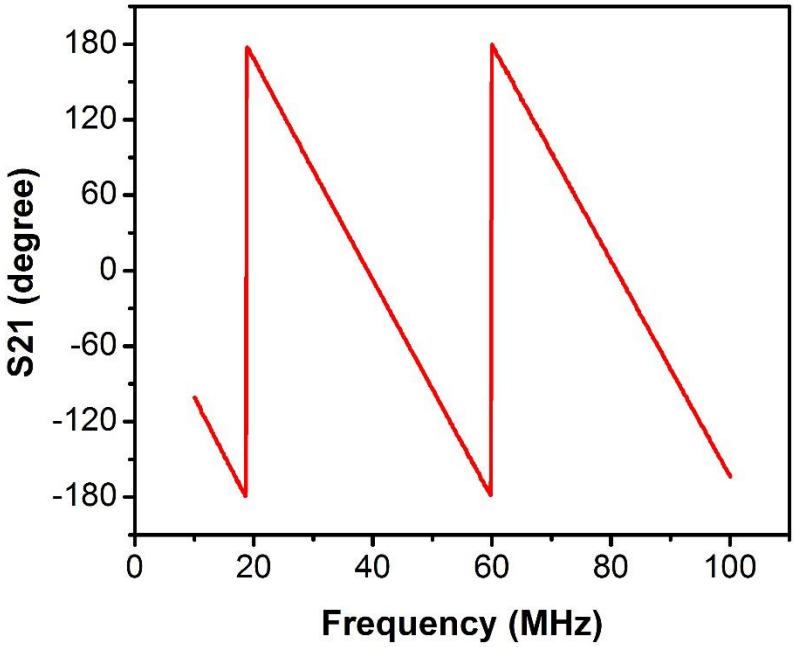

Figure 36. System Phase

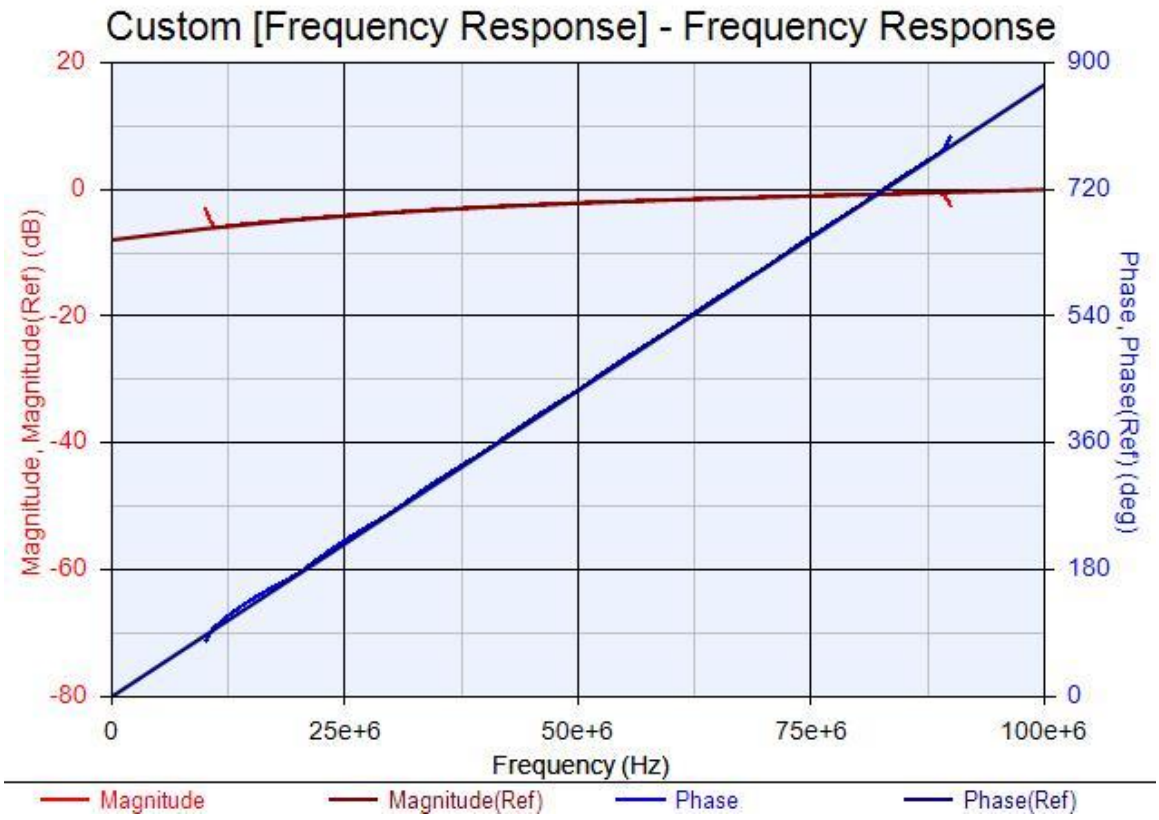

Figure 37. Finite Impulse Response Filter

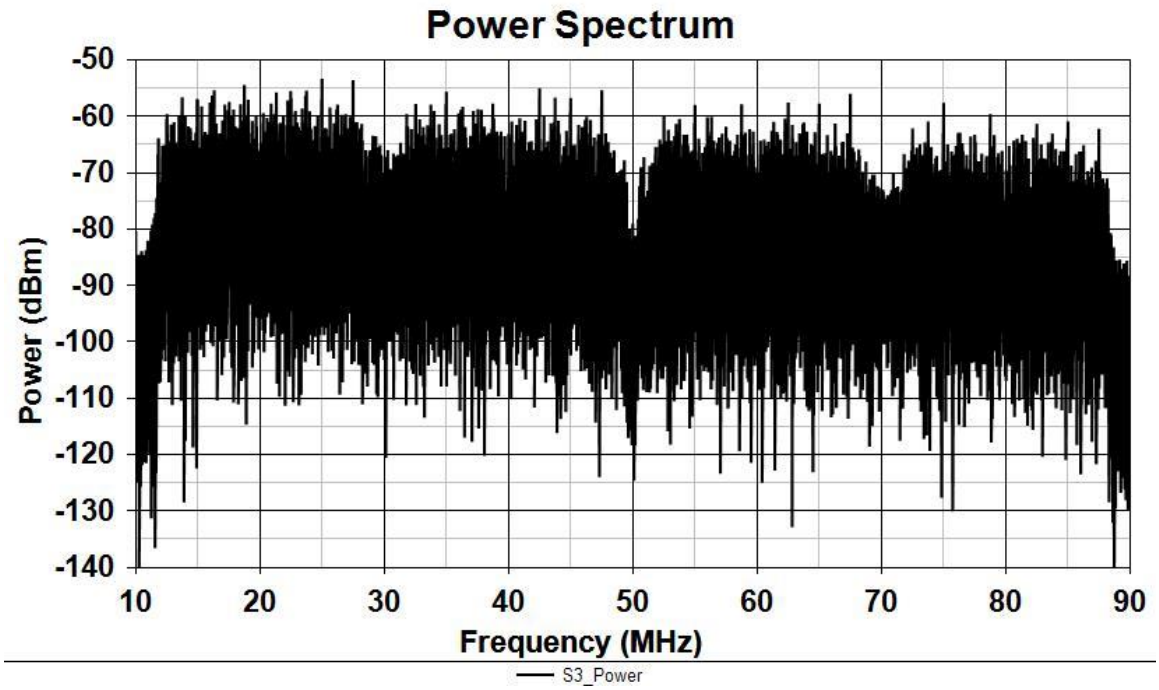

Figure 38. Power Spectrum without Post Equalization

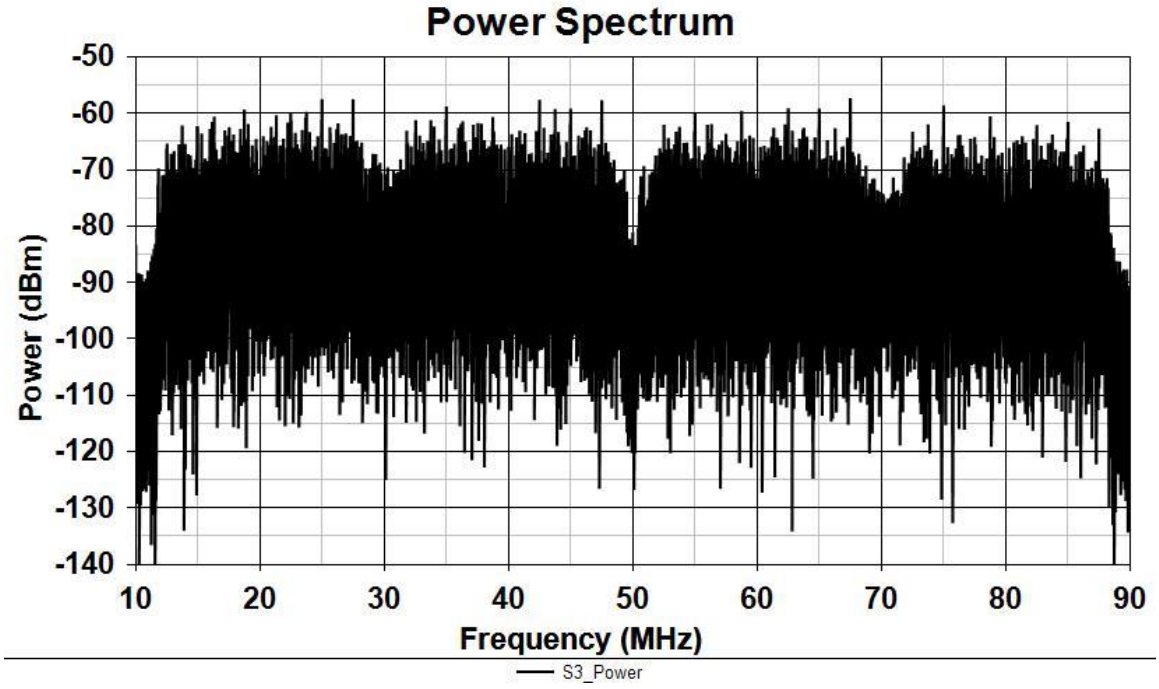

Figure 39. Power Spectrum with Post Equalization

Figure 38 shows the power spectrum without post equalization. Figure 39 demonstrates the power spectrum with post equalization. With post equalization, the droop becomes improved. Therefore, EVM becomes better. EVM of 256 QAM 5/6 coding rate decreases from -27.196 dB to 27.429 dB. But BER stays meanwhile.

If the additive white noise is the only source of noise in IEEE AWGN BER analysis, the Wi-Fi over VLC link can be simulated as shown in Figure 41. Table 5 illustrates the results Eb/N0 versus BER in IEEE 802.11ac AWGN BER Analysis. When the energy per bit to noise power spectral density ratio is 9, BER is close to our experimental results.

Table 5. Eb/N0 versus BER in IEEE 802.11ac AWGN BER Analysis

Eb/N0	BER
7	0.029
8	6.57E-04
9	5.76E-05
10	3.42E-06

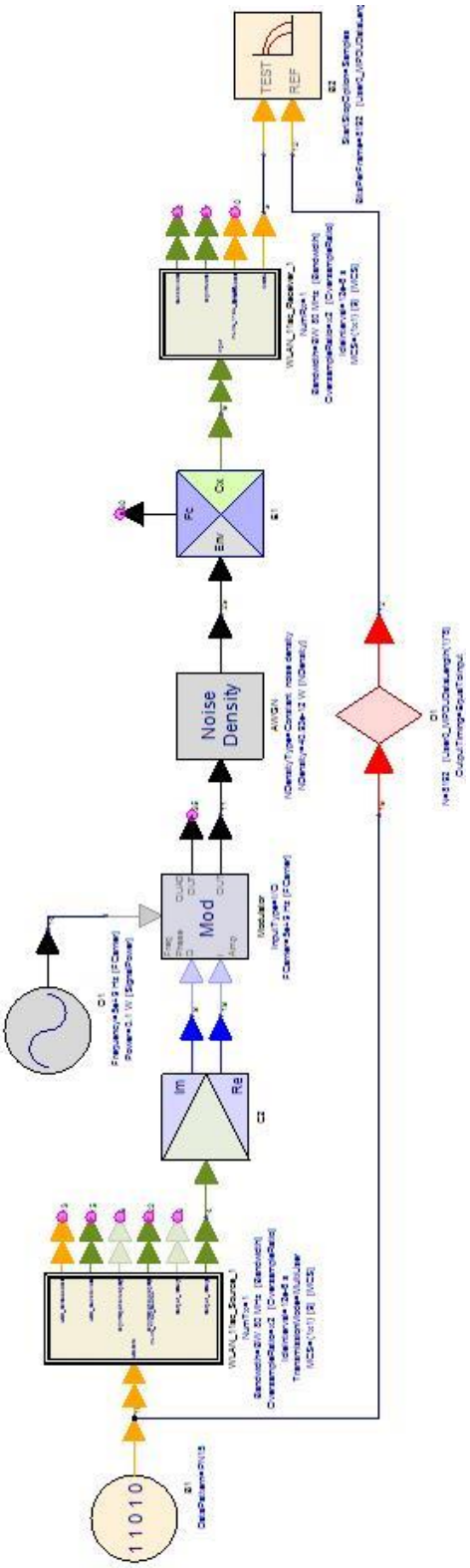

Figure 40. IEEE 802.11ac AWGN BER Analysis

CHAPTER 5

SELF-POWERED CHIP FOR VLC

5.1 Introduction

Attitude sensors are widely used in the aircraft's orientation which usually depends on some reference vectors. According to the reference vectors they use, attitude sensors are classified into different categories including gyrocompasses, magnetometers, star tracking sensors, and sun tracking sensors. Sun tracking sensors are characterized among the attitude sensors due to their simple structures, low power consumption and low cost in the aircraft applications. In recent years, nanosatellites have rapidly developed in military and commercial field because of nanosatellites' low power consumption, low weight and low cost. A nanosatellite usually has a weight less than 10 kg. So it is significant for the sun tracking sensors which are a necessary part of nanosatellites to minimize. Many kinds of sun sensors have been utilized into space applications including positioning solar panels, orienting solar thermal collectors, and the spacecraft attitude determination [65]. However, most solutions need some special process, such as MEMS, or other off-chip devices which is a trade-off of the weight and size of sensor [66-68]. In this case, it is better to have an on-chip light direction sensor for this system. Many techniques have been developed to detect light direction, such as the shading device method [69], the tilted surface method [70], and the collimator tube method [71]. However, this conventional techniques have some disadvantages on accuracy, size and integration [72]. Both small form factor and low power consumption is required by many aircraft applications. Since we can use the light detected to provide needed energy, energy harvesting is an attractive approach which absorbs ambient energy to support the system. A self-powered on-chip sensor is a smart choice to meet these requirements. Some complete solutions have been presented, but these solutions

just offer an analog output which cannot directly provide control signals to the system [73] e.g., controlling attitude of solar panel or aircraft. Apart from aircraft utilization, the light direction detection sensor chip we designed can also be transplanted into some internet of things such as smart medical, smart vehicles and smart home. This paper demonstrates a self-powered solution with an on-chip light direction sensor and real-time adaptive tracking ADC to detect the direction of the incident light. In our approach, the integrated real-time adaptive tracking ADC can generate a digitized output that can directly control the system. Built in photodiodes are utilized to harvest energy so no external power supply is needed when the chip works. On-chip photo sensor offers the light direction with an accuracy of 1.8 degree over a 120 degree range. In addition, the digitized output has an accuracy of approximate 7 ENOB.

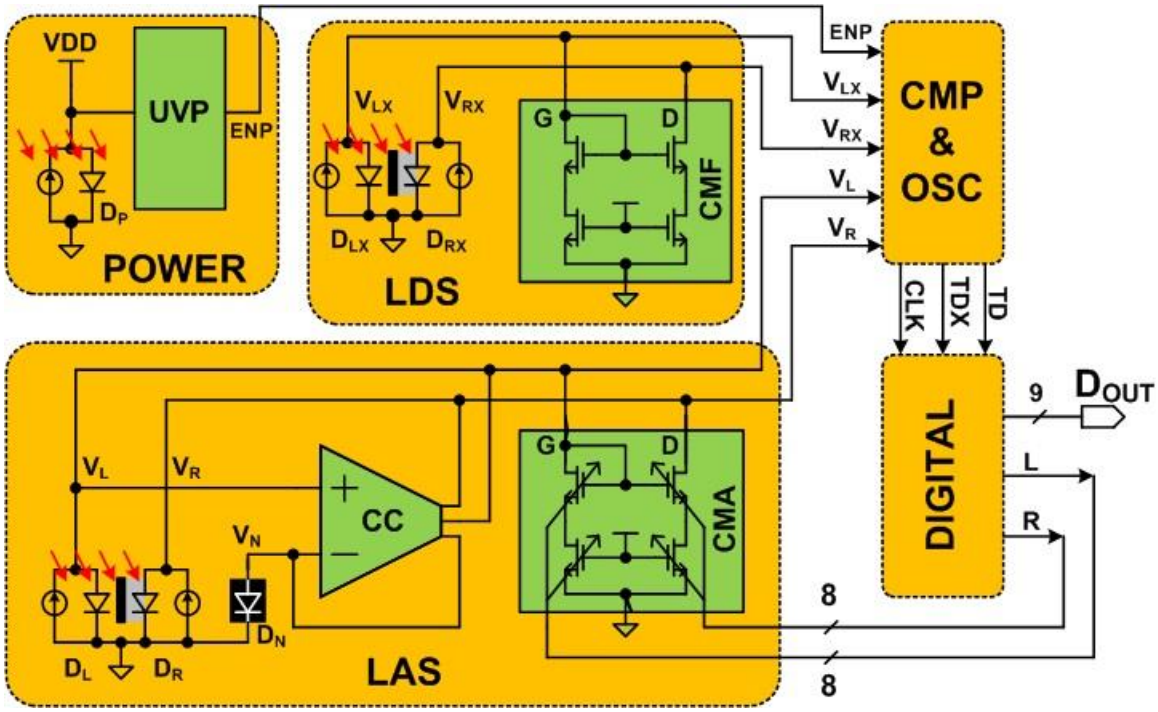

Figure 41. The Block Diagram of the Self-powered Light Direction Chip

5.2 Top-level Design

The complete block diagram of the self-powered sensor chip we presented in this work is shown in Figure 41 including five blocks: POWER, LDS, LAS, OSC & CMP and DIGITAL. In POWER block, the photodiode DP harvests energy for the other blocks. The current sources beside diodes indicate the photocurrents generated by corresponding photodiodes. Under Voltage Protection (UVP) is an adaptive supply voltage monitoring circuit. When VDD is lower than the threshold of transistor which changes due to process deviation, the circuit provides an EPN signal to switch the chip into sleep mode in which oscillator stops but the digitized output is stored to decrease the power consumption. LAS is a Light Angle Sensor with the Adjustable Current Mirror (ACM) which is regulated by the further digitized signals and LDS is a Light Direction Sensor with the Fixed Current Mirror (FCM). Two identical photodiodes are located on opposite sides of the micro-scale metal wall as it is revealed in both LAS and LDS. The four identical photodiodes DL, DLX, DR, and DRX generate four different photocurrents with diverse incident light. Current mirror ACM and FCM convert the four photocurrents into four voltage signals VL, VLX, VR and VRX. These signals come into OSC & CMP block to generate direction and angle signals TDX and TD. Besides that, the OSC & CMP block also generates clock signal CLK. Depending on these signals, DIGITAL block produces two 8 bits digitized signals to adjust the ratio of the current mirror ACM and a 9 bits digitized signal for incident light information. In order to improve the measurement precision, a Current Compensation (CC) circuit is designed in LAS. These blocks will be described in detail in the latter parts of this paper. Section 3 describes the photo sensor and the circuit implement of proposed approach. Section 4 gives the measure results and discussion. Finally, conclusions are presented in Section 5.

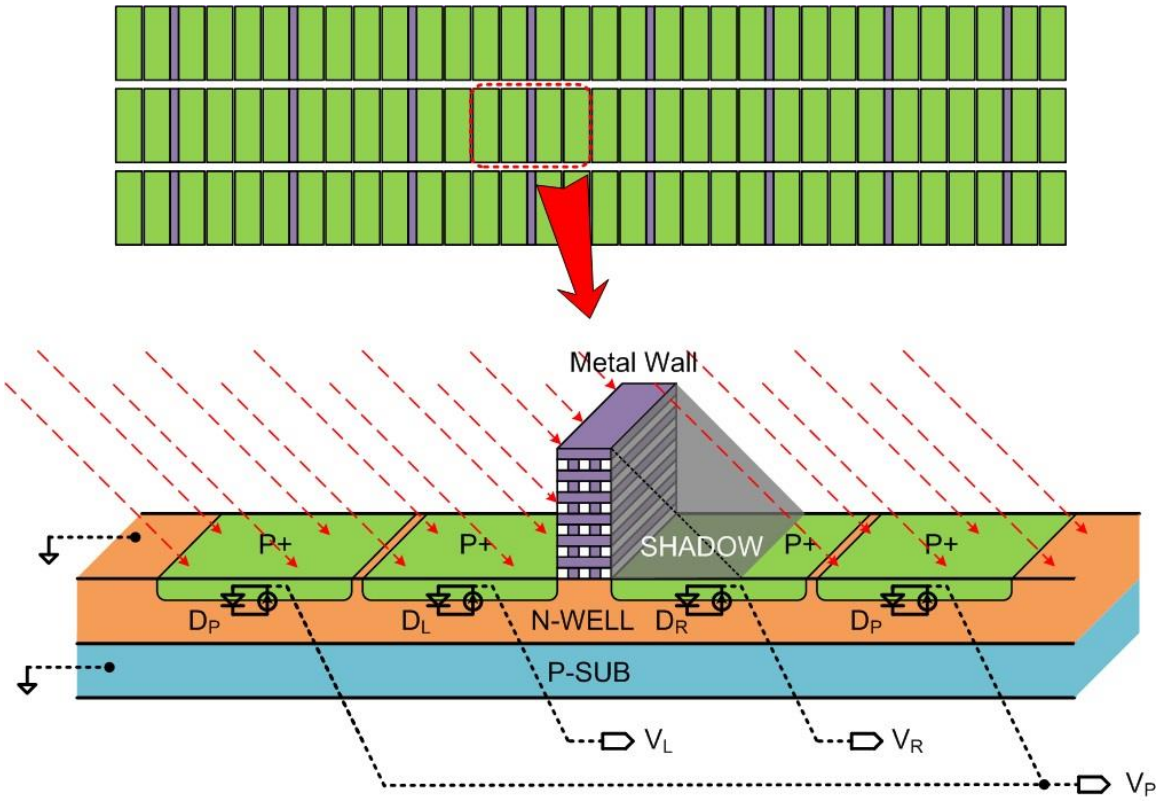

Figure 42. Structure of the Presented On-chip Sensor

5.3 Circuit Implementation

5.3.1 Photo Sensor

Figure 42 shows the structure of the on-chip light direction sensor, the diodes pairs DL, DLX, DR, and DRX have the same structure. The basic sensor cell of the on-chip light direction sensor lies at the bottom of Figure 42. Many primary cells compose the on-chip sensor as shown at the top. As an innovative detection method, the sensor we presented consists of 154 individual sensor basic cells for a total area of approximately 1.25 mm^2 fabricated in a standard 0.18 μm CMOS process.

Each cell has a metal wall created by stacking all metal layers, contacts, and vias available in the process to generate on-chip micro-scale shadow. The height of the metal wall is h, and the width of identical photodiodes on both sides of the wall is w. We should optimize the dimensions of the metal wall for the sensors good performance. In this design, diffraction has also been considered. As we all know, the bandgap voltage of silicon is about 1.12 V. So the longest wavelength of the absorbed light is about 1.1 μm. The absorption peak is around 0.7 μm. In this design, height is designed as 12 μm and width is designed ad 15 μm. The physical dimensions are much larger than the wavelength of the absorbed light. So the diffraction has little influence on the sensors performance. The basic cell of the photodiode is built by P+ resistance in N-well. The contact of the N-well and the connection metals form a wall which is used to block the light pass through the middle position of the two photodiodes. When the light comes from not just the middle top, the two photodiodes will receive different luminous flux, hence the two photodiodes generate different amount of currents. As it is shown in Figure 42, light comes from right to left and this means the right photodiode is fully illuminated and the left one is partly shadowed by the metal wall. In this case, the total photocurrent generated by the right diode DR can be divided into three parts. The first part of the current is the current generated by the light which directly illuminates the diode. The second part is the current generated by the reflected light from the metal wall. And the rest of the current is generated by the residual light reflected many times by the back metal base, the metal layers, and the interfaces of different materials. For the left photodiode DL, the total current consists of only the first and the third part. While the currents generated by right one DR have three parts.

The photodiode model shown in Figure 42 is composed of a current source and a diode. DR and DL which locate on both of the metal baffle are utilized to detect

light. Two energy harvesting photodiodes DP placed separately on both sides of the sensor cell are used to provide power for the whole chip. The photocurrent ratio of the smaller one to the larger one in DR and DL is almost linearly dependent on the angle of the incident light. A function of the ratio of current and the incident light angle has been described above. According to the function, we can get the incident light angle messages with an accuracy of 1.8 degrees over a 120 degree range.

5.3.2 Forward Current Compensation Circuit

The current ratio of the two photodiodes DL and DR shown in Figure 43 has an approximate linear relationship with the angle of the incident light. As described above, we use a basic model for the photodiodes composed of a diode and a current source, the forward currents IDL and IDR decrease the accuracy of the ratio between two photocurrents. So we present a compensation circuit (CC) as shown in Figure 43 to compensate the forward current. In this circuit, we design a special diode DN which is the same kind of DL and DR but is completely shielded by metal layers, thus there is no photocurrent in DN. The size ratio of DN, DL, DR is 1: n: n. In order to match the current, PMOS currents has the same ratio of 1: n: n. The NMOS threshold voltage in this process is about 0.3V. The voltages VL and VR will be higher than the NMOS threshold voltage when the photocurrents IPL and IPR flow through ACM. If IO is low, DN is reverse biased and VN is low. While VL is about NMOS threshold voltage 0.3V, because there is a photocurrent flowing IPL into the ACM. If IO is high, DN is forward biased and VN is about 0.6 V. The V-I curves of the diode DN and photodiode DL has been described in the lower right corner of Figure 43. The curves describe the relationship of voltage between DN and DL in different current conditions. The OP shown in the yellow part of Figure 43 is used to keep VN=VL. Based on Kirchhoff's Current Law at the point A, we can get the equation as follow:

nIO+IPL=IDL+IL. Considering the size ratio of diodes, IDL=nIPN=nIO. Hence, we can get another equation IPL=IL which means that all the photocurrents generated by DL flow into ACM without the effect of forward currents. For IPR, when the real-time adaptive tracking ADC reaches a balanced state, VR almost equals to VL, so IDR=nIDL=nIO, and hence IPR=IR. So the compensation circuit works well and enhances the accuracy of the ratio between two photocurrents.

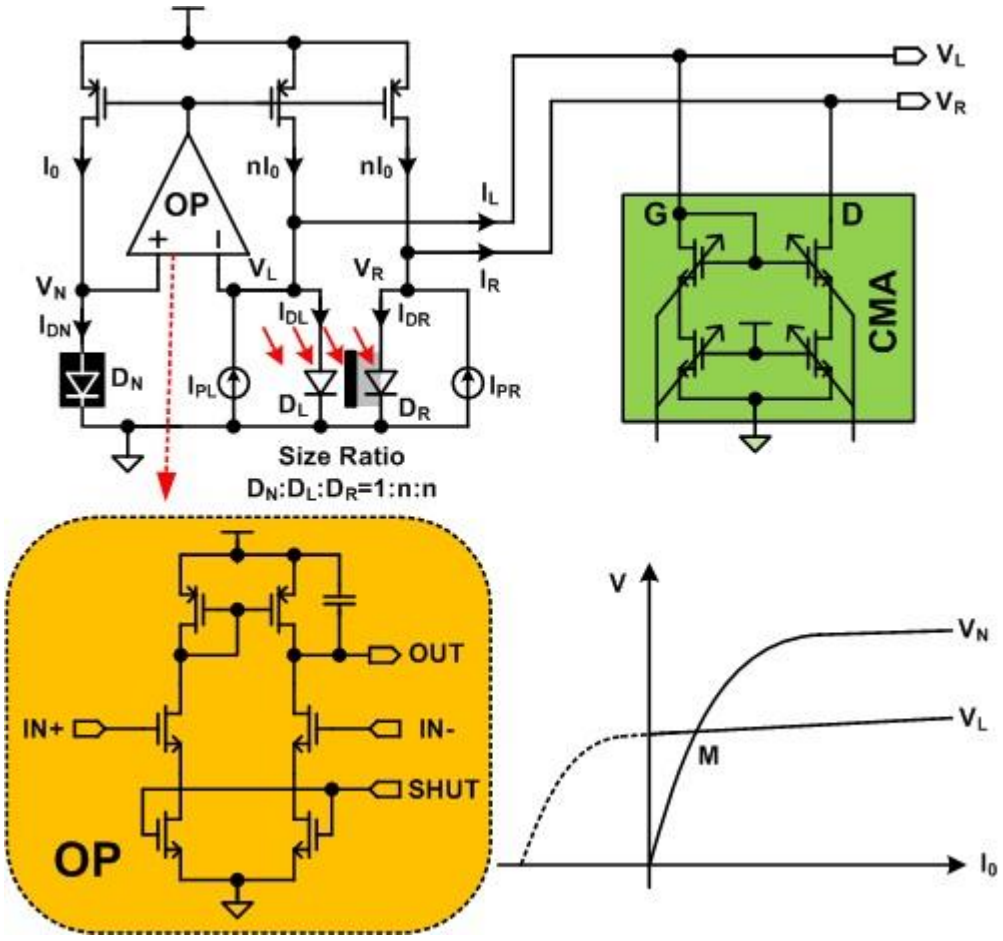

Figure 43. Forward Current Compensation Circuit

5.3.3 Oscillator & Comparator Block

The OSC & CMP block shown in Figure 44 generates incident light angel/direction signal TD/TDX and clock signal for DIGTIAL block further processing. It is mentioned above that the photocurrents have been converted into voltages (VL, VLX, VR and VRX) by adjustable current mirror (ACM) and fixed current mirror (FCM). These voltages are compared by CMP in OSC & CMP block to get TD and TDX. The comparator has an enable signal SET to control it. Its outputs are both high levels when SET is low. When SET is high, it compares the two input signals VL, VLX, VR and VRX. When the comparing is completed, one of the outputs signal will change to low level. This change will be detected and used to generate the clock signal and to indicate the comparing result. The purple part in Figure 44 receives the signal SET and outputs XCK with inverse phase after a delay time. So the function of this block can be seen as an inverter. Then we get the clock signal CLK and it is the inverse phase of XCK. Unlike a usual oscillator, the frequency of our oscillator in this work is variable and adaptive. Because the power supply is offered by the photodiode DP absorbing ambient energy which is very limited and varying with the incident optical intensity. So we present a low power ADC with an adaptive frequency oscillator to fit the power supply. When the incident optical power is intense, the oscillator will generate high frequency to fit the quick digitized output. On the contrary, the weak power results in the low frequency to decrease the power consumption. The delay time in the oscillator loop depends on not only the comparator operating speed, but also the capacitor values and charging/discharging currents. The T-ADJ block in this work is designed to control the discharging current for adjusting the delay time. It can be seen that the discharging current is dependent on G1 and G2 which are controlled by VL, VLX, VR and VRX. The higher incident optical power leads to higher voltages of VL, VLX, VR and VRX which results in higher discharging currents in the T-ADJ block. The oscillator outputs a high frequency signal in this condition.

Whereas, lower incident optical power results in lower voltages, lower discharging currents and lower frequency finally. T-ADJ block also has a control terminal G3 to enhance the discharging current as necessary. The OSC & CMP block provides CLK, TD, TDX signals which represent clock, light angel and light direction to the DIGITAL block for data processing.

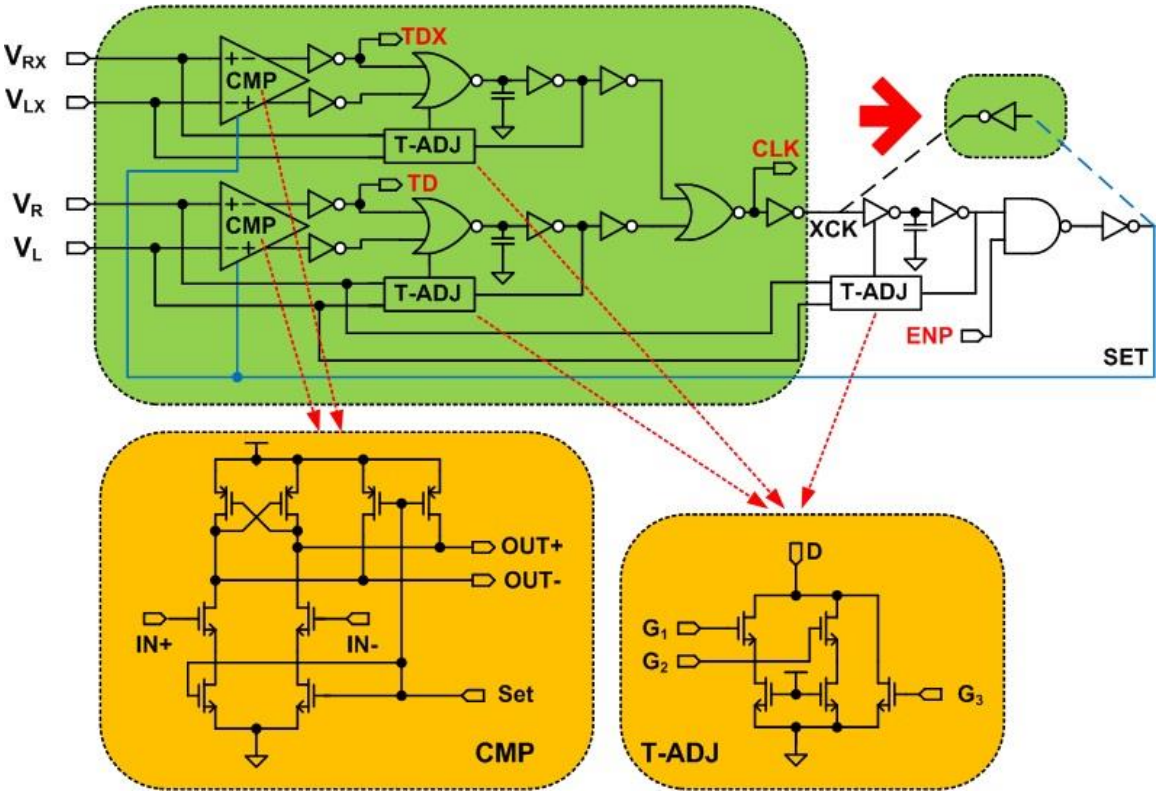

Figure 44. The Schematic of OSC & CMP Block

5.3.4 Digital Block

DIGITAL block works like an analog to digital converter to generate a 9-bits digitized output. And this ADC has an adaptive conversion speed with variable supply power. This block receives three signals TD, TDX and CLK which are generated by

OSC & CMP block and outputs three signals L, R and DOUT. L and R both are 8 bits signals which go back to control the current mirror ratio in ACM. DOUT is a 9 bits signal that carries the incident light angel and direction. The first bit of DOUT means the incident light direction left/right with 0/1, respectively. When DOUT begins with 0, it means the light comes from left side, and the other bits of DOUT mean the current ratio of left side to right side. Similarly, DOUT indicates the incident light from right side and the current ratio of right side to left side when the first bit of DOUT is 1. Figure 45 shows the complete block diagram of DIGITAL in this work. DIGITAL block can be divided into three parts, 8 bits up/down adder and register circuit, ADD/SUB control signal detection and generation circuit, and output level circuit. The core of DIGITAL block is the 8 bits up/down adder and register circuit which consists of an 8 bits full adder as function of real-time adaptive tracking ADC and 8 DFF for latching data. The ADD and SUB signals are generated by all 0 detection circuit and all 1 detection circuit which is shown in the red dotted frame. The two signals are used to control an 8 bits full adder in an add operation or a subtraction operation. When the detected signal D which represents the latter 8 bits of DOUT indicating the current ratio is 00000000, the ADD signal will be 0 and the SUB signal will be 1. So the 8 bits full adder is set to an add operation and D will accumulate. When the signal D is detected as 11111111, the 8 bits full adder will work in subtraction operation and D will decrease. If D is neither 00000000 nor 11111111, the operation mode of full adder will be dependent on TD and TDX rather than ADD and SUB. Not only the full adder but also the Light Angle Output depends on TD. TD and TDX which produced by OSC & CMP block can be permuted and combined into four types 00, 01, 10, and 11. When the combination of TD and TDX is 00 or 11, the full adder will work in a subtraction operation and D decreases. Conversely, when the combination of TD and TDX is 01 or 10, the full

adder will work in an add operation and D accumulates. Through output level circuit, we obtain the output DOUT and L and R are in different conditions according to TD and TDX. The 8 bits signal L and R which represent the incident light angle information come back to control the adjustable current mirror. Then the adjustable current mirror's outputs change and TD maybe change or not. So D will increase or decrease with the incident light angle changing. The flow chart of the signal processing in DIGITAL block is shown in Figure 45.

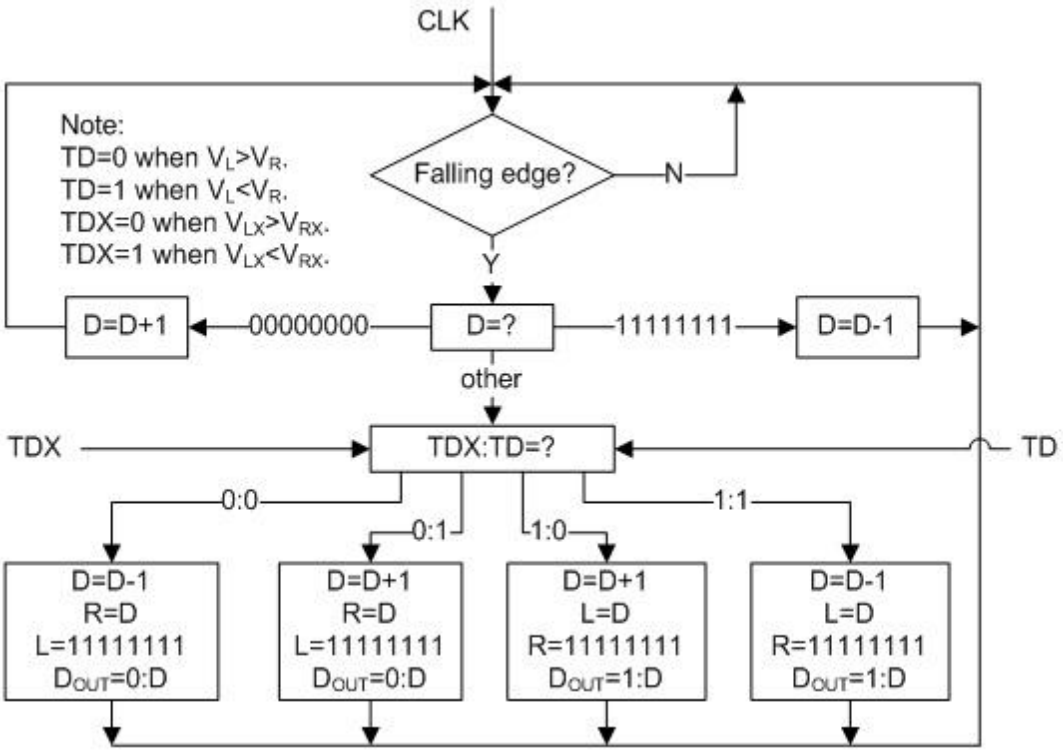

Figure 45. Flow Chart of Data Processing in DIGITAL block

5.4.4 Under Voltage Protection Block

In this work we use photodiodes absorbing ambient light to provide the power supply, however the variable incident optical power leads to unstable power supply. Considering the risk of low supply voltage, an Under Voltage Protection (UVP) circuit

is needed. Under Voltage Protection as shown in Figure 46 is designed like a simple power management to detect the voltage of the power supply. VDD is compared with the threshold of transistor not with some a fixed value. So the UVP circuit is adaptive, because the threshold of transistor varieties due to different processes, process deviation or some other environment effects. If the power supply voltage generated by photodiodes is lower than the threshold voltage, the UVP circuit outputs an ENP signal which controls the oscillator entering sleep state and no longer oscillating. In this case, all the digitized outputs are stored and VDD will not decrease more. When the photodiodes harvest enough energy, VDD becomes higher and chip works again. In Figure 46, there are two resistances which are used to set a threshold range for preventing the ENP signal flipping back and forth. In this work, the wake-up voltage is 383 mV while the standby voltage is 360 mV.

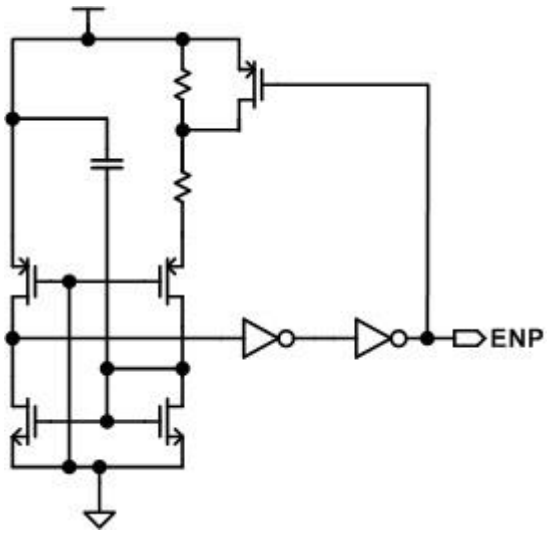

Figure 46. The Schematic of Under Voltage Protection Circuit

5.4 Layout and Test Results

The chip is fabricated in a 0.18 μm CMOS process with 6 metal layers and the whole areas is 4.5 mm². Figure 47 shows the micrograph of the test chip including

an expanded view of the interface circuits and sensor elements. The interface circuits are covered by metal layers to prevent the circuits from the incident light. We have marked the important blocks in the chip micrograph in Figure 47.

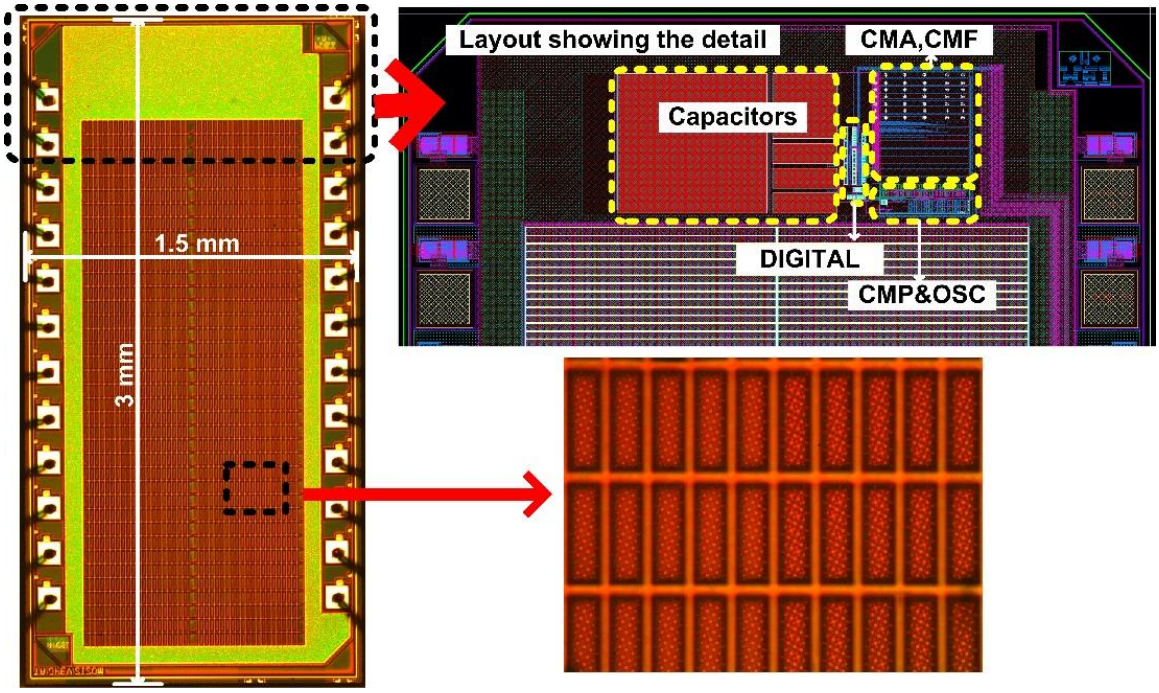

Figure 47. The Layout for the Interfaces Circuits

To verify the performance of our chip, we set up a test platform as shown in Figure 48. The self-power chip is mounted on a breadboard which is placed on an angular actuator to allow us to adjust the angle of the incident light. We measure the data with an oscilloscope both inside the laboratory and outside under the sun. The energy harvesting photodiodes absorb the ambient light to generate a supply power ranging from 380 mV to 480 mV over the optical intensity from 45 mW/cm² to 95 mW/cm². In the range of the optical intensity, the chip generates a variable frequency changing from 1.57 kHz to 32.93 kHz. The UVP circuit works and the oscillator stops when the power supply is lower than the threshold approximately

380 mV. Some relationships of VDD and oscillator frequency is shown in Figure 49. In Figure 49, it is clear that 380 mV is the minimum evoke voltage and the oscillator frequency changes automatically as VDD varieties. The power supply and frequency are proportional to the optical intensity. The relationships of VDD and frequency versus optical intensity are plotted in Figure 49.

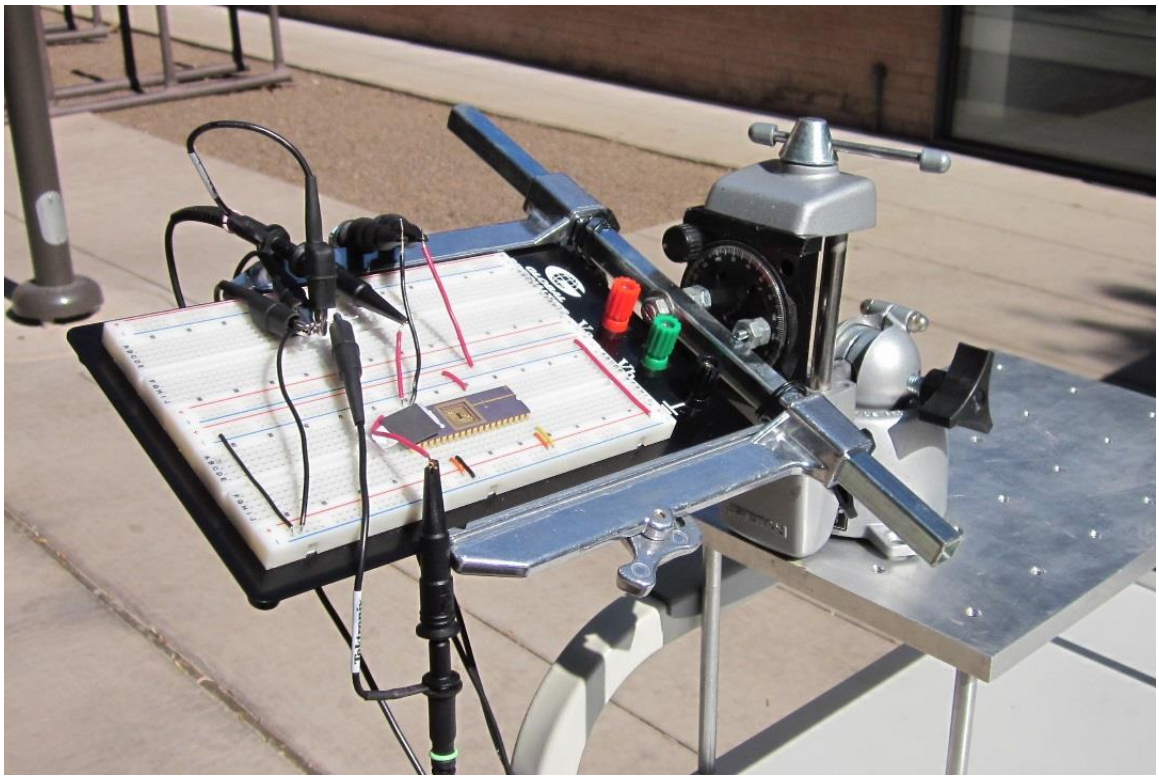

Figure 48. The Test Platform

We adjust the incident light angle to measure the short currents IPR and IPL for an optical intensity of 80 mW/cm^2. It is shown in Figure 49. When the incident light angle is zero, the two photocurrents are equal. When the incident light angle is negative, the left photocurrent is larger than the right one and vice versa. It is significant to calculate a ratio of the small current to the large current for comparison. The calculated ratio will be compared with the digitized output ratio of

real time adaptive tracking ADC and Figure 49 shows the comparison result. The two ratios are very close to each other, and 7 ENOB is achieved as the test results. The power supply is completely driven by on-chip photodiodes without any exterior energy sources. So the power consumption is low ranging from 727 nW to 2.32 μW for the test optical intensity.

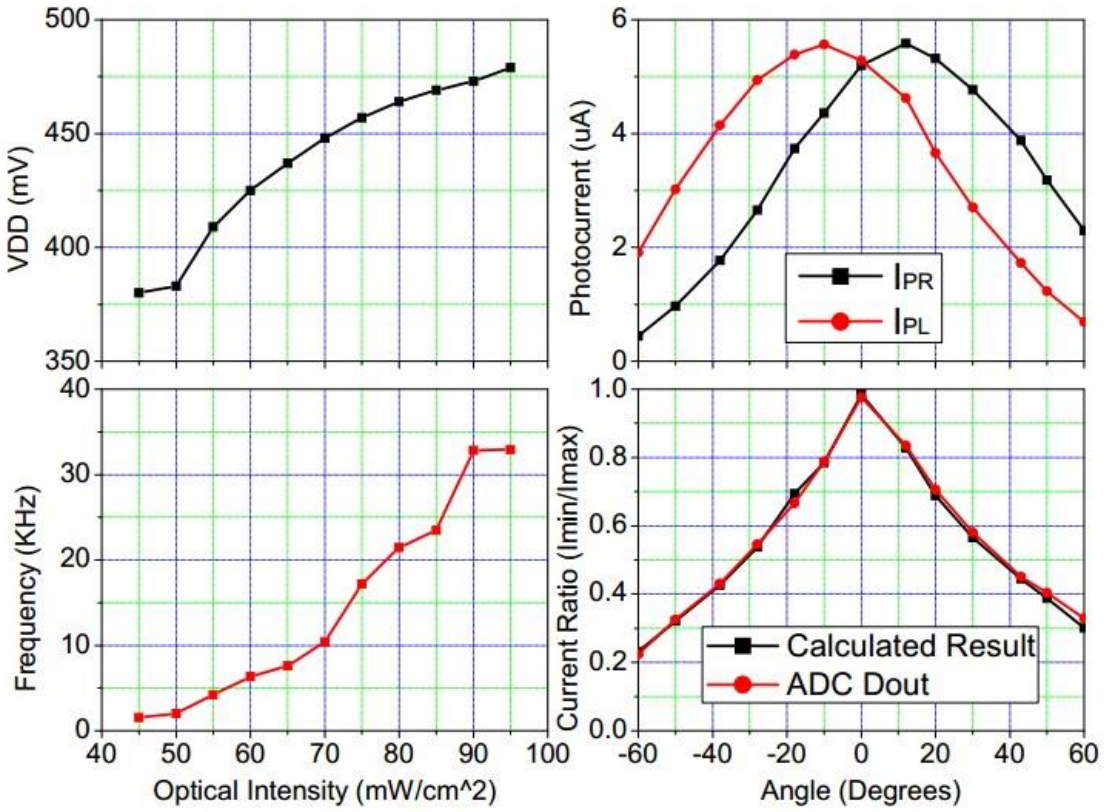

Figure 49. Test Results: VDD and Frequency vs. Optical Intensity, Short Circuit Photocurrents vs. Incident Light Angle, Current Ratio vs. Incident Light Angles

5.5 Self-powered Chip for VLC

We did preliminary test on the self-powered chip for visible light communication as shown in Figure 50. It just shows the feasibility that VLC can

transmit clock signal to self-powered chip which can be widely used in IoT system. Figure 51-53 demonstrate that when the clock signal is modulated in the light emission of laser diode, the self-powered chip can sense the clock signal and regards it as universal clock signal. 100 KHz clock signal can be transmitted by laser diode based VLC. The experiment will be improved in the future research.

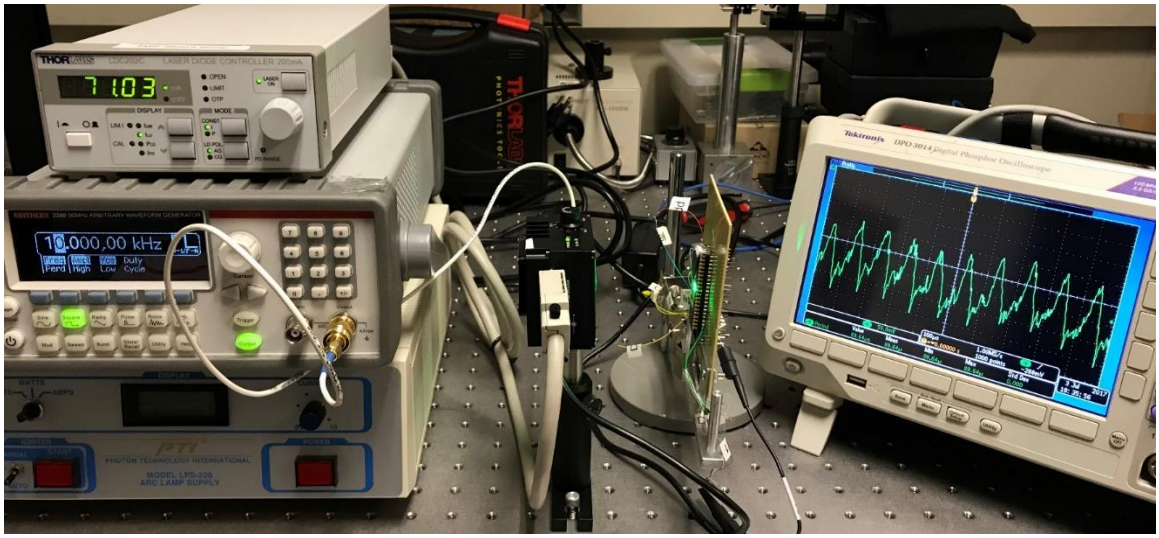

Figure 50. Self-powered Chip for VLC Test Setup

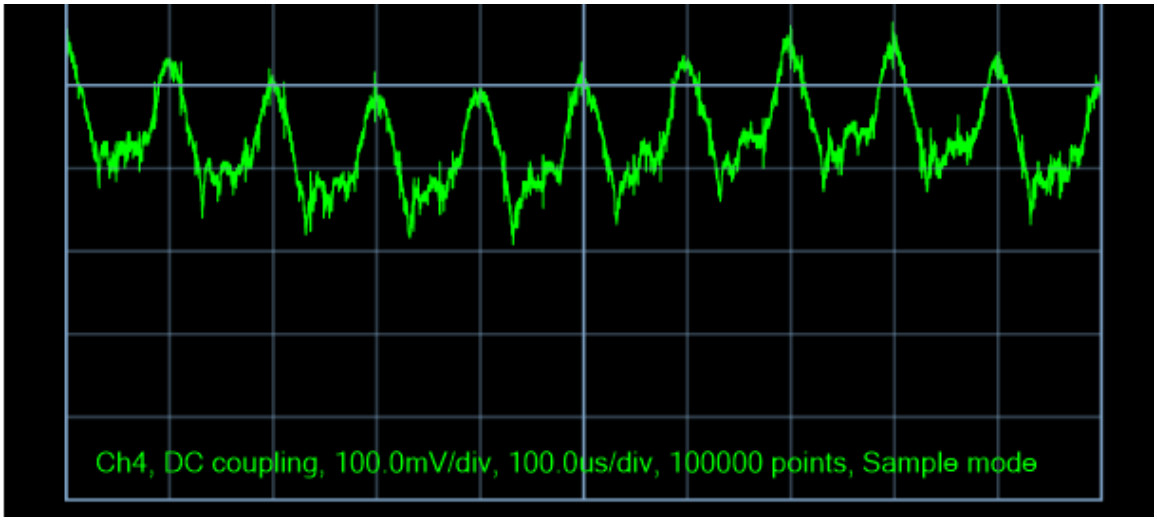

Figure 51. 10 kHz 1Vpp Square Wave AC Input

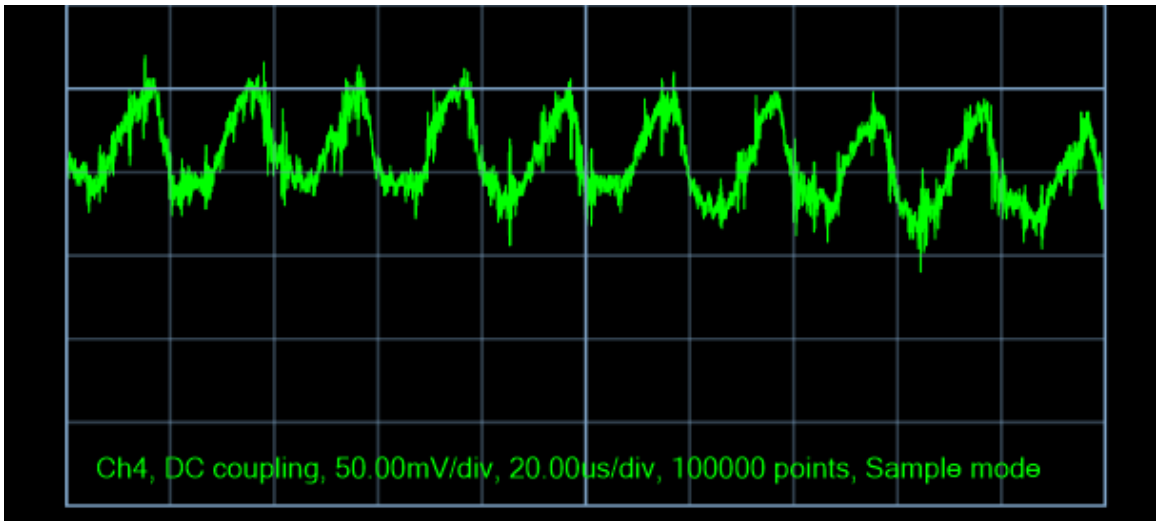

Figure 52. 50 kHz 1Vpp Square Wave AC Input

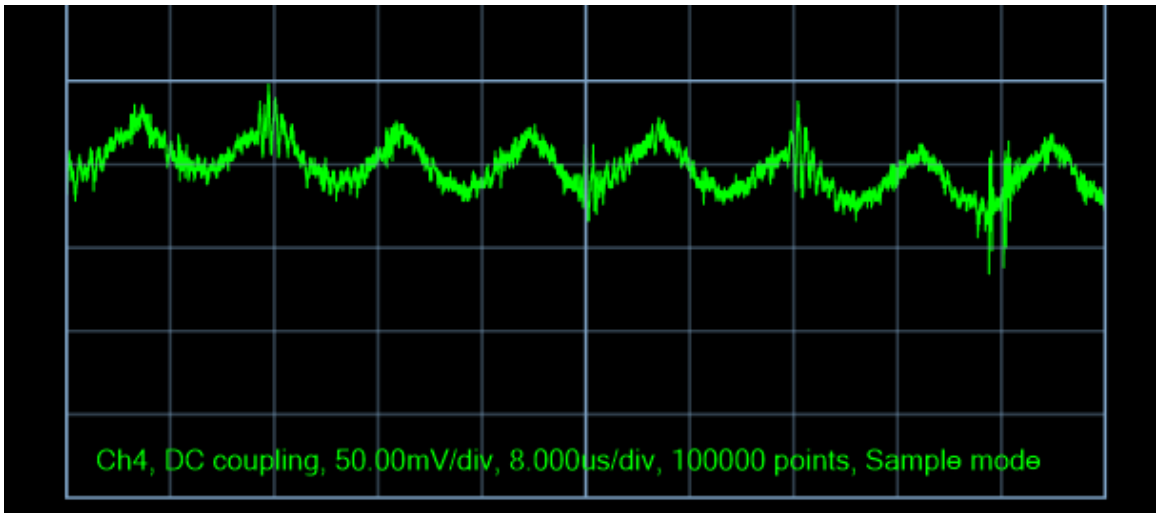

Figure 53. 100 kHz 1Vpp Square Wave AC Input

CHAPTER 6

CONCLUSION

VLC can be employed to realize a high throughout wireless network competing with 5G RF systems. In addition, GaN-based micro-LEDs provide important qualities ideal for the implementation of VLC links. The VLC using GaN-based micro-LED demonstrates the communication link at a data rate of 600 Mbps and a BER of 2.1×10^{-4} for a distance of 80 cm in our dissertation. But this VLC system is so sensitive that manual focus is essential. We put forward a novel active tracking method to increase BER by orders and enlarge the FOV of the PIN receiver to 120° even if it is out of focus. So the micro-LED based VLC becomes both optically and mechanically robust.

The NLOS VLC using a single GaN micro-LED was experimentally demonstrated in this work. Several advanced approaches were utilized for the feasibility of VLC, including the 92.7 MHz modulation bandwidth of the micro-LED, the modification of IEEE 802.11ac standard, and the proposed optics. All these techniques offered a high-speed LOS VLC at a data rate of 433 Mbps and a BER of 5×10^{-5} at a free space transmission distance of up to 3.6 m. Moreover, based on these techniques we also provided a possible VLC link in both directed NLOS and non-directed NLOS. Specially, non-directed NLOS VLC was achieved at a data rate of 195 Mbps and a BER of 10×10^{-5} via one reflection. Beyond theoretical analysis, the first experimental demonstration of practical implementation of NLOS VLC shows significance for indoor VLC system establishment.

REFERENCES

[1] H. Haas. (2011, Aug.). Wireless data from every light bulb. TED Website.

[2] A. Jovicic, J. Li, and T. Richardson. "Visible light communication: opportunities, challenges and the path to market." IEEE Communications Magazine 51, no. 12 (2013): 26-32.

[3] Y. Wang, Y. Wang, N. Chi, J. Yu, and H. Shang. "Demonstration of 575-Mb/s downlink and 225-Mb/s uplink bi-directional SCM-WDM visible light communication using RGB LED and phosphor-based LED." Optics Express 21, no. 1 (2013): 1203-1208.

[4] L. Grobe, A. Paraskevopoulos, J. Hilt, D. Schulz, F. Lassak, F. Hartlieb, C. Kottke, V. Jungnickel, and K. Langer. "High-speed visible light communication systems." IEEE Communications Magazine 51, no. 12 (2013): 60-66.

[5] H, Haas, L. Yin, Y. Wang, and C. Chen. "What is LiFi?." Journal of Lightwave Technology 34, no. 6 (2016): 1533-1544.

[6] E. Sarbazi, M. Uysal, M. Abdallah, and K. Qaraqe, "Ray tracing based channel modeling for visible light communications," in Proc. 22nd Signal Process. Commun. Appl. Conf., Apr. 2014, pp. 702–705.

[7] A. Farid and S. Hranilovic, "Capacity bounds for wireless optical intensity channels with Gaussian noise," IEEE Trans. Inf. Theory, vol. 56, no. 12, pp. 6066–6077, Dec. 2010.

[8] B. Rofoee, K. Katsalis, Y. Yan, Y. Shu, T. Korakis, L. Tassiulas, A. Tzanakaki, G. Zervas, and D. Simeonidou, "First demonstration of service-differentiated converged optical sub-Wavelength and LTE/WiFi Networks over GEAN," in Proc. Opt. Fiber Commun. Conf. Exhib., Mar. 2015, pp. 1–3.

[9] IEEE Std. 802.15.7-2011, IEEE Standard for Local and Metropolitan Area Networks, Part 15.7: Short-Range Wireless Optical Communication Using Visible Light, IEEE Std., 2011.

[10] Z. Lu, P. Tian, H. Chen, I. Baranowski, H. Fu, X. Huang, J. Montes et al. "Active tracking system for visible light communication using a GaN-based micro-LED and NRZ-OOK." Optics Express 25, no. 15 (2017): 17971-17981.

[11] H. Elgala, R. Mesleh, and H. Haas. "Indoor optical wireless communication: potential and state-of-the-art." IEEE Communications Magazine 49, no. 9 (2011).

[12] M. Z. Afgani, H. Haas, H. Elgala, and D. Knipp. "Visible light communication using OFDM." In Testbeds and Research Infrastructures for the Development of Networks and Communities, 2006. TRIDENTCOM 2006. 2nd International Conference on, pp. 6-pp. IEEE, 2006.

[13] H. Elgala, R. Mesleh, H. Haas, and B. Pricope. "OFDM visible light wireless communication based on white LEDs." In Vehicular Technology Conference, 2007. VTC2007-Spring. IEEE 65th, pp. 2185-2189. IEEE, 2007.

[14] H. Elgala, R. Mesleh, and H. Haas. "Indoor broadcasting via white LEDs and OFDM." IEEE Transactions on consumer electronics 55, no. 3 (2009).

[15] H. Elgala, and T. D. Little. "Reverse polarity optical-OFDM (RPO-OFDM): dimming compatible OFDM for gigabit VLC links." Optics express 21, no. 20 (2013): 24288-24299.

[16] S. Rajagopal, R. D. Roberts, and S. Lim. "IEEE 802.15. 7 visible light communication: modulation schemes and dimming support." IEEE Communications Magazine 50, no. 3 (2012).

[17] H. Burchardt, N. Serafimovski, D. Tsonev, S. Videv, and H. Haas, "VLC: Beyond point-to-point communication," IEEE Commun. Mag. 52(7), 98–105 (2014).

[18] N. Zhao, X. Li, G. Li, and J. M. Kahn, "Capacity limits of spatially multiplexed free-space communication," Nat. Photon. 9(12), 822–826 (2015).

[19] P. Tian, J. J. McKendry, Z. Gong, S. Zhang, S. Watson, D. Zhu, I. M. Watson, E. Gu, A. E. Kelly, C. J. Humphreys, and M. D. Dawson, "Characteristics and applications of micro-pixelated GaN-based light emitting diodes on Si substrates," J. Appl. Phys. 115(3), 1–6 (2014).

[20] H. Chen, H. Fu, Z. Lu, X. Huang, and Y. Zhao, "Optical properties of highly polarized InGaN light-emitting diodes modified by plasmonic metallic grating," Opt. Express 24(10), 856–867 (2016).

[21] H. Chen, H. Fu, X. Huang, Z. Lu, X. Zhang, J. Montes, and Y. Zhao, "Optical Cavity Effects in InGaN Micro-Light Emitting Diodes With Metallic Coating," IEEE Photon. J. 9(3), 1–8 (2017).

[22] M. S. Islim, R. X. Ferreira, X. He, E. Xie, S. Videv, S. Viola, S. Watson, N. Bamiedakis, R. V. Penty, I. H. White, and A. E. Kelly, "Towards 10 Gb/s orthogonal frequency division multiplexing-based visible light communication using a GaN violet micro-LED," Photon. Res. 5(2), 35–43 (2017).

[23] T. Peyronel, K. J. Quirk, S. C. Wang, and T. G. Tiecke, "Luminescent detector for free-space optical communication," Optica 3(7), 787–792 (2016).

[24] R. C. Peach, G. L. Burdge, T. Tidwell, and J. G. Vickers, "System and method for free space optical communication beam acquisition," U.S. Patent App. 13/780, 489 (2013).

[25] M. Jeganathan, and K. Kiasaleh, "Transceiver, system, and method for free-space optical communication and tracking," U.S. Patent App. 09/808, 496 (2001).

[26] H. Wang, T. Luo, Z. Lu, H. Song, and J. B. Christen, "CMOS self-powered monolithic light-direction sensor with digitalized output," Opt. Lett. 39(9), 2618–2621 (2014).

[27] H. Song, Z. Lu, T. Luo, J. B. Christen, and H. Wang, "A CMOS self-powered monolithic light direction sensor with SAR ADC," in IEEE International System-on-Chip Conference (IEEE, 2014), pp. 58–62.

[28] H. Wang, T. Luo, Y. Fan, Z. Lu, H. Song, and J. B. Christen, "A self-powered single-axis maximum power direction tracking system with an on-chip sensor," Sol. Energ. 112, 100–107 (2015).

[29] W. Yang, S. Zhang, J. J. D. McKendry, J. Herrnsdorf, P. Tian, Z. Gong, Q. Ji, I. M. Watson, E. Gu, M. D. Dawson, L. Feng, C. Wang, and X. Hu, "Size-dependent capacitance study on InGaN-based micro-light-emitting diodes," J. Appl. Phys. 116(4), 044512 (2014).

[30] P. Tian, X. Liu, S. Yi, Y. Huang, S. Zhang, X. Zhou, L. Hu, L. Zheng, and R. Liu, "High-speed underwater optical wireless communication using a blue GaN-based micro-LED," Opt. Express 25(2), 1193-1201 (2017).

[31] V. Zabelin, D. A. Zakheim, and S. A. Gurevich, "Efficiency improvement of AlGaInN LEDs advanced by raytracing analysis," IEEE J. Quantum Electron. 40(12), 1675–1686 (2004).

[32] P. Tian, A. Althumali, E. Gu, I. M. Watson, M. D. Dawson, and R. Liu. "Aging characteristics of blue InGaN microlight emitting diodes at an extremely high current density of 3.5 kA cm−2," Semicond. Sci. Technol. 31(4), 045005 (2016).

[33] H. Fu, Z. Lu, and Y. Zhao, "Analysis of low efficiency droop of semipolar InGaN quantum well light-emitting diodes by modified rate equation with weak phase-space filling effect," AIP Adv. 6(6), 065013 (2016).

[34] H. Fu, Z. Lu, X. H. Zhao, Y. H. Zhang, S. P. DenBaars, S. Nakamura, and Y. Zhao, "Study of Low-Efficiency Droop in Semipolar ($20\bar{2}1\bar{}$) InGaN Light-Emitting Diodes by Time-Resolved Photoluminescence," J. Display Technol. 12(7), 736–741 (2016).

[35] C. C. Pan, Q. Yan, H. Fu, Y. Zhao, Y. R. Wu, C. Van de Walle, S. Nakamura, and S. P. DenBaars, "High optical power and low-efficiency droop blue light-emitting diodes using compositionally step-graded InGaN barrier," Electron. Lett. 51(15), 1187–1189 (2015).

[36] C. A. Balanis, Advanced Engineering Electromagnetics (John Wiley & Sons, 2012).

[37] J. R. Barry, J. M. Kahn, W. J. Krause, E. A. Lee, and D. G. Messerschmitt, "Simulation of multipath impulse response for indoor wireless optical channels," IEEE J. Sel. Areas Commun. 11(3), 367–379 (1993).

[38] J. M. Kahn, and J. R. Barry, "Wireless infrared communications," in Proceedings of the IEEE (IEEE, 1997), pp. 265–298.

[39] J. B. Carruthers, and P. Kannan, "Iterative site-based modeling for wireless infrared channels," IEEE Trans. Antennas Propag. 50(5), 759–765 (2002).

[40] J. B. Carruthers, S. M. Carroll, and P. Kannan, "Propagation modelling for indoor optical wireless communications using fast multi-receiver channel estimation," in IEEE Proceedings-Optoelectronics (IEEE, 2003), pp. 473–481.

[41] A. M. Khalid, G. Cossu, R. Corsini, P. Choudhury, and E. Ciaramella, "1-Gb/s transmission over a phosphorescent white LED by using rate-adaptive discrete multitone modulation," IEEE Photon. J. 4(5), 1465–1473 (2012).

[42] R. X. Ferreira, E. Xie, J. J. McKendry, S. Rajbhandari, H. Chun, G. Faulkner, S. Watson, A. E. Kelly, E. Gu, R. V.Penty, and I. H. White, "High bandwidth GaN-based micro-LEDs for multi-Gb/s visible light communications," IEEE Photon. Technol. Lett. 28(19), 2023–2026 (2016).

[43] R. Sridhar, R. D. Roberts, and S. Lim. "IEEE 802.15.7 visible light communication: modulation schemes and dimming support," IEEE Commun. Mag. 50(3), 72–82 (2012).

[44] B. Sklar, Digital communications (Vol. 2) (Prentice Hall, 2001).

[45] V. Kelly. "New IEEE 802.11 ac specification driven by evolving market need for higher, multi-user throughput in wireless LANs," IEEE Standards Association (2014).

[46] E. Perahia and M. X. Gong. "Gigabit wireless LANs: an overview of IEEE 802.11 ac and 802.11 ad," ACM SIGMOBILE Mobile Comput. Commun. Rev. 15(3), 23–33 (2011).

[47] D. Tsonev, H. Chun, S. Rajbhandari, J. J. McKendry, S. Videv, E. Gu, M. Haji, S. Watson, A. E. Kelly, G. Faulkner, and M. D. Dawson. "A 3-Gb/s single-LED OFDM-based wireless VLC link using a gallium nitride," IEEE Photon. Technol. Lett. 26(7), 637–640 (2014).

[48] H. Chun, S. Rajbhandari, G. Faulkner, D. Tsonev, E. Xie, J. McKendry, E. Gu, M. Dawson, D. C. O'Brien, and H. Haas. "LED based wavelength division multiplexed 10 Gb/s visible light communications," J. Lightw. Technol.34(13), 3047–3052 (2016).

[49] X. Li, L. Wu, Z. Liu, B. Hussain, W. C. Chong, K. M. Lau, and C. P. Yue. "Design and characterization of active matrix LED micro displays with embedded visible light communication transmitter," J. Lightw. Technol. 34(14),3449–3457 (2016).

[50] M. Saadi, L.Wattisuttikulkij, Y. Zhao, and P. Sangwongngam. "Visible light communication: opportunities, challenges and channel models," Int. J. Electron. Informat. 2(1), 1–11 (2013).

[51] R. Yuan, and J. Ma. "Review of ultraviolet non-line-of-sight communication," China Commun. 13(6), 63–75 (2016).

[52] D. Silage, Digital Communication System Using System VUE (Firewall Media, 2006).

[53] A. K. Majumdar. "Non-line-Of-sight (NLOS) ultraviolet and indoor free-space optical (FSO) communications," in Advanced Free Space Optics (FSO) (Springer, 2015).

[54] G. Cossu, R. Corsini, and E. Ciaramella. "High-speed bi-directional optical wireless system in non-directed line-of-sight configuration," J. Lightw. Technol. 32(10), 2035–2040 (2014).

[55] M. S. Chowdhury, W. Zhang, and M. Kavehrad. "Combined deterministic and modified monte carlo method for calculating impulse responses of indoor optical wireless channels," J. Lightw. Technol. 32(18), 3132–3148 (2014).

[56] Z. Xu, H. Ding, B. M. Sadler, and G. Chen. "Analytical performance study of solar blind non-line-of-sight ultraviolet short-range communication links," Opt. Lett. 33(16), 1860–1862 (2008).

[57] G. Chen, Z. Xu, H. Ding, and B. M. Sadler. "Path loss modeling and performance trade-off study for short-range non-line-of-sight ultraviolet communications," Opt. Express 17(5), 3929–3940 (2009).

[58] H. Ding, G. Chen, A. K. Majumdar, B. M. Sadler, and Z. Xu. "Modeling of non-line-of-sight ultraviolet scattering channels for communication," IEEE J. Sel. Areas Commun. 27(9), 1535–1544 (2009).

[59] G. Chen, Z. Xu, and B. M. Sadler. "Experimental demonstration of ultraviolet pulse broadening in short-range non-line-of-sight communication channels," Opt. Express 18(10), 10500–10509 (2010).

[60] Cisco, Cisco Visual Networking Index. "Global mobile data traffic forecast update, 2013–2018." white paper (2014).

[61] A. M. Khalid, G. Cossu, R. Corsini, M. Presi, and E. Ciaramella. "Demonstrating a hybrid radio-over-fibre and visible light communication system." Electronics letters 47, no. 20 (2011): 1136-1137.

[62] M. Ayyash, H. Elgala, A. Khreishah, V. Jungnickel, T. Little, S. Shao, M. Rahaim, D. Schulz, J. Hilt, and R. Freund. "Coexistence of WiFi and LiFi toward 5G: Concepts, opportunities, and challenges." IEEE Communications Magazine 54, no. 2 (2016): 64-71.

[63] D. A. Basnayaka, and H. Haas. "Design and Analysis of a Hybrid Radio Frequency and Visible Light Communication System." IEEE Transactions on Communications (2017).

[64] M. B. Rahaim, A. M. Vegni, and T. D. Little. "A hybrid radio frequency and broadcast visible light communication system." In GLOBECOM Workshops (GC Wkshps), 2011 IEEE, pp. 792-796. IEEE, 2011.

[65] N. Xie, and A. J. Theuwissen. "Low-power high-accuracy micro-digital sun sensor by means of a CMOS image sensor." Journal of Electronic Imaging 22, no. 3 (2013): 033030-033030.

[66] P. Sarkar, and S. Chakrabartty. "A compressive piezoelectric front-end circuit for self-powered mechanical impact detectors." In Circuits and Systems (ISCAS), 2013 IEEE International Symposium on, pp. 2207-2210. IEEE, 2013.

[67] M. Guan, and W. Liao. "Comparative analysis of piezoelectric power harvesting circuits for rechargeable batteries." In Information Acquisition, 2005 IEEE International Conference on, pp. 4-pp. IEEE, 2005.

[68] D. Yuan, Z. Wen, H. Liao, and Z. Wen, "Power self-regulation circuit of piezoelectric multi-shaker micro-generator," Electronic Measurement and Instruments. 2007 ICEMI 07 8th International Conference on, 2007, pp. 656–660.

[69] J. Quero, A. Guerrero, L. Franquelo, M. Dominguez, I. Ameijeiras, and L. Castaner, "Light source position microsensor," Circuits and Systems, 2001. ISCAS 2001 The 2001 IEEE International Symposium on. vol. 3, 2001, pp. 648–651.

[70] K. Karimov, M. Saqib, P. Akhter, M. Ahmed, J. Chattha, and S. Yousafzai, "A simple photo-voltaic tracking system," Solar Energy Materials and Solar Cells., vol. 87, no. 1, pp. 49–59, 2005.

[71] H. Mousazadeh, A. Keyhani, A. Javadi, H. Mobli, K. Abrinia, and A. Sharifi, "A review of principle and sun-tracking methods for maximizing solar systems output," Renewable and Sustainable Energy Reviews., vol. 13, no. 8, pp. 1800–1818, 2009.

[72] P. Ortega, G. López-Rodríguez, J. Ricart, M. Domínguez, L. M. Castañer, J. M. Quero, C. L. Tarrida et al. "A miniaturized two axis sun sensor for attitude control of nano-satellites." IEEE Sensors Journal 10, no. 10 (2010): 1623-1632.

[73] J. Delgado F, M. Quero J, J. Garcia, et al. "Accurate and Wide-Field of-View MEMS-Based Sun Sensor for Industrial Applications," IEEE Transactions on Industrial Electronics. 2012, 59(12):4871 - 4880.